Design and Optical Analysis of BISOU

By

Saoirse Doyle

Supervisor: Dr. Neil Trappe

A thesis submitted in partial fulfilment for the
degree of Master of Science

Maynooth University
National University of Ireland Maynooth

Faculty of Science and Engineering
Department of Physics

April 2026

Contents

Abstract

This thesis describes the design and initial optical design, layout and testing of a nulling polarising interferometer for observation of CMB spectral distortions called BISOU (**B**alloon **I**nterferometer for **S**pectral **O**bservations of the **U**niverse) which is a pathfinder balloon experiment for future proposed space missions such as FOSSIL, a current ESA M7 mission proposal. Firstly, the background of spectral distortions and a justification of the proposed science are given based on discussion of previous mission proposals.

Various example initial designs are analysed using TICRA GRASP, which is a commercial physical optics simulation software. Then in Chapter 4 an analysis technique known as Gaussian beam mode analysis (GBMA) is introduced. GBMA allows the tracking of beam parameters (the beam radius, radius of curvature, and phase slippage) and allows an alternative technique to analyse truncation or loss of power due to finite sized optical components in BISOU. GBMA has different assumptions/approximations compared to Physical Optics, so GBMA is a useful technique for verifying the output from GRASP.

A truncation analysis of BISOU optical designs using Laguerre-Gaussian and Hermite-Gaussian beam modes is introduced in Chapter 5. Values obtained from this technique are compared with spillover values taken from GRASP.

A modal analysis of example beams from conical horns and pyramidal multimoded horns is then performed to check for aberration/distortion of the beam as it propagates through the system. This multimoded analysis of the BISOU optics will be critical to analyse the throughput and optical performance of BISOU from 90 to 1500 GHz where its full multimoded behaviour will need to be incorporated into future optical models

Acknowledgements

I would like to thank my supervisor Dr. Neil Trappe for his patience, continuous support and valuable insight.

I would like to thank all members of the Physics Department of Maynooth University.

Thanks to members of the BISOU consortium for the valuable experience gained working with a broad project collaboration. In particular, I would like to thank members of the BISOU Optics Working Group with whom I worked closely

1 Chapter 1: CMB Spectral Distortions

1.1 Cosmic Microwave Background

The Cosmic Microwave Background refers to remnant radiation remaining from the Big Bang. To even a very sensitive optical telescope the space in between stars is completely black. However, a sufficiently sensitive far-infrared/radio telescope will detect a faint background glow that is almost uniform across the sky. This background radiation is energy leftover from the Big Bang and the formation of the Universe.

The first prediction of this background radiation was made by George Gamow, Ralph Alpher and Robert Herman in the 1940s. It was theorised that because the early Universe was much hotter and denser than its current state, any photons released in the early Universe would undergo scattering many times. This scattering would cause the radiation and matter in the early Universe to enter thermal equilibrium and therefore the emitted radiation would have a blackbody spectrum. (Alpher & Herman, 1949)

A blackbody is an ideal model which absorbs/emits all incident radiation regardless of frequency or angle of incidence. It then reemits this radiation in a spectrum according to its temperature. This radiation obeys the classic relationship known as Planck's Radiation Law:

$$E_{\lambda} = \frac{8\pi hc}{\lambda^5} \times \frac{1}{\exp\left(hc / kT\lambda\right) - 1} \tag{1.1}$$

Where E_{λ} is the energy radiated by the blackbody at a wavelength λ, c is the speed of light, k is Boltzmann's constant, T is the temperature of the blackbody in Kelvin and h is Planck's constant.

The frequency or wavelength where the peak emission occurs is given by Wiens displacement Law

$$\lambda = \frac{b}{T} \tag{1.2}$$

where λ is the wavelength of the peak of the blackbody spectrum, b is Wiens displacement constant and T is the temperature of the blackbody source.

The CMB spectrum is very close to an ideal blackbody spectrum with a peak at 2.726 Kelvin

As the Universe expands and this radiation is redshifted into the microwave spectrum it would be expected that this radiation would retain a blackbody spectrum. Any deviation from this blackbody spectrum at 2.726 K is known as a spectral distortion.

The remnant radiation from the Big Bang was first measured in 1965 by Penzias and Wilson of Bell Labs. After observing this faint signal over a period of time and failing to detect any modulation, and also observing that the intensity of the signal received was independent of the position observed on the sky, the only remaining possible conclusion was that it was cosmological in origin and existed everywhere. (Bothun, 1998). An interesting aspect of the CMB is how uniform it is thermally. The Cosmic Microwave Background is uniform at the 10^{-5} level (Räsänen, 2009).

As the speed of light is an upper limit on how fast anything in the Universe can travel, this places an upper limit on the region of space around a specific point where there could have been any physical interaction. This region of space is constantly expanding as time passes since the Big Bang as light originating in the early Universe would have had longer time to propagate.

The expansion of the Universe is characterised by a cosmological scale factor a which is proportional to t, the time since the Big Bang. The scale factor is set to 1 at the present time, is less than 1 in the past, and greater than 1 in the future. This means that the region of space across which physical interactions could occur was smaller in the past.

However, this raises the question of how the temperature of the CMB became so uniform. How could regions of space in opposite directions interact physically to have uniform temperature distribution. These regions of space are physically far enough away that not enough time has passed since the Big Bang for these interactions to occur.

The theory of cosmic inflation solves this issue known as the “horizon problem”. Developed by Alan Guth, Andrei Linde, Paul Steinhardt, and Andy Albrecht in 1980, cosmic inflation theory predicts that after the Big Bang the Universe

underwent a period of exponential expansion, faster than the speed of light, before slowing again to its current expansion rate.

This solves the issue of the horizon problem and the uniformity of the CMB as these regions would have been close enough in the early Universe to reach thermal equilibrium before the rapid expansion during the inflation period. However, we are still waiting for direct measurement proof of this inflation theory.

Thomson scattering in a perfectly homogeneous, isotropic distribution of matter and photons will lead to the emission of unpolarised light. However, the early Universe has a small level of inhomogeneity. Quantum fluctuations produce small "clumps" or anisotropies in the matter distribution in the early Universe. Gravitational attraction within the matter causes these small clumps to grow into the large-scale structures we see in the Universe today such as galaxies.

In the case of an isotropic radiation field, there are equal intensities of light hitting the electrons from all directions and the electron oscillates in all directions equally. Thus, the polarisation of the scattered light would be zero with no prominent orientation.

Now considering a quadrupole radiation field with higher intensity along one axis (for example the x-axis), the electrons oscillations will be larger in the y-direction than the x-direction, thus the electric field of the scattered light will be larger in the y-direction, and the scattered light will be slightly polarised. So, light emitted from scattering in a matter cloud that is even slightly inhomogeneous as in the case of the early Universe will lead to some level of polarisation of the scattered light. These density perturbations only produce a specific type of CMB polarisation known as E-Modes. (Rahimi & Reichardt, 2024)

Gravitational waves (tensor perturbations of spacetime) from inflation will also have their own effect on this polarisation of the CMB. The stretching and squeezing of spacetime will also produce these non-homogeneous radiation fields and will thus also lead to the emission of polarised light in the CMB (Rahimi & Reichardt, 2024). Gravitational wave interactions will only produce a specific type of polarisation known as B-Modes.

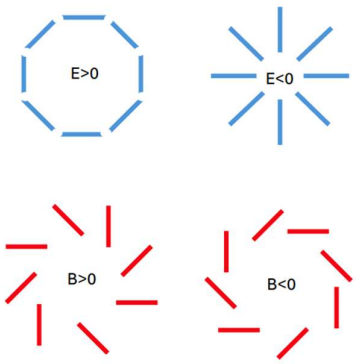

Figure 1.1 Diagram of E mode polarisation and B mode polarisation. For E mode polarisation the orientation is horizontal or vertical. The B modes are polarised at 45 degrees. (Rahimi & Reichardt, 2024)

When discussing polarisation, the Stokes parameters I, Q, U and V are normally used, where I describes the total intensity of the light, Q and U are measures of the light's linear polarization and V is a measure of the circular polarization. For cosmological analyses I, Q and U are generally converted to T, E and B. The terms E and B modes refer to the gradient-like and curl-like nature of the electric (E) and magnetic (B) fields. E modes have a gradient and zero curl, while B modes have zero gradient and nonzero curl (Baumann, et al., 2008).

1.2 Previous Measurements of CMB (COBE/FIRAS)

The first space mission specifically designed to measure the Cosmic Microwave Background was the Cosmic Background Explorer (COBE) launched by NASA in 1989. COBEs main aim was to make an all-sky map of the cosmic microwave background (Boggess, et al., 1992).

COBEs FIRAS (Far Infrared Absolute Spectrophotometer) instrument was a Polarizing Michelson Interferometer with an internal reference blackbody calibrated by an external blackbody used to measure the CMB spectrum. COBE was able to accurately measure the spectrum of the CMB (shown in figure 1.2) relative to a reference blackbody, to within $3.4 \times 10^{-8}\ ergs\ cm^{-2} sr^{-1} cm$ over a frequency range of 2 to 20 cm^{-1}.

FIRAS scanned the sky 1.6 times in a frequency range of 30 GHz to 3 THz (a wavelength range of 0.1 mm to 10 mm), in in two channels separated by 0.5 mm, with a 7-degree field of view flared horn antenna. It had dual inputs and outputs. One input receives radiation from the sky, the other input receives emission from an internal calibration source with an emissivity ≈0.98 within 5% of a blackbody. The external calibrator was shown to be isothermal to better than 1 mK at 2.7 K. (Fixsen, et al., 1996)

As an FTS, FIRAS used a movable mirror to modulate the path length difference between the calibrator beam and the sky beam. It used two different scanning modes a "long" mode with an OPD of 5.8 cm and a "short" mode with an OPD of 1.2 cm, giving a spectral resolution of $0.45cm^{-1}$ or 13 GHz for the long scanning mode. It had a flared horn antenna giving a 7-degree field of view. The data was collected at 43 positions equally spaced along the spectrum. (Mather, et al., 1993)

FIRAS had an RMS sensitivity better than $\frac{10^{-9}W}{cm^2sr}$. The instrument had a Noise Equivalent Power of $4 \times 10^{-1}\ W/\sqrt{Hz}$. FIRAS was not background limited, and its sensitivity was instead determined by phonon noise from its 1.4 K detector (Chluba, et al., 2020).

Using the (FIRAS) instrument COBE measured the temperature of the CMB to be 2.735+-0.017 K over a wavelength range of 0.5 to 5 mm (Mather, et al., 1994). The maximum deviation of the CMB spectrum from a perfect blackbody spectrum was measured to be less than 0.03%. This measurement placed such a narrow limit on these deviations that the error bars on a plot of the CMB spectrum (as in figure 1.2) are smaller than the thickness of the line. The error bars shown represent an error level of 400σ, the actual error present in the measurements is much smaller.

This measurement placed 95% confidence limits on the values of distortion parameters to (Mather, et al., 1994):

$$\mu < 3.3 \times 10^{-4}$$

$$y < 2.5 \times 10^{-5}$$

where μ and y are measures of the deviation of the spectrum from a perfect blackbody due to chemical potential in the case of μ, or related to the scattering

processes in the case of *y*. *y* is a parameter that expresses by how much a photon will change its energy due to repeated scatterings. These parameters and their origins are further explained in section 1.3. These parameters were estimated by fitting the observed spectra to a model of the blackbody emission including these distortion parameters (Mather, et al., 1994). However, the expected values of these parameters are an order of magnitude smaller than the limits placed by the FIRAS measurements. ΛCDM predicts "a y-type spectrum, with a y-parameter reaching ' $few \times 10^{-6}$. Although the uncertainty in the amplitude of this contribution is rather large" (Chluba, 2016)

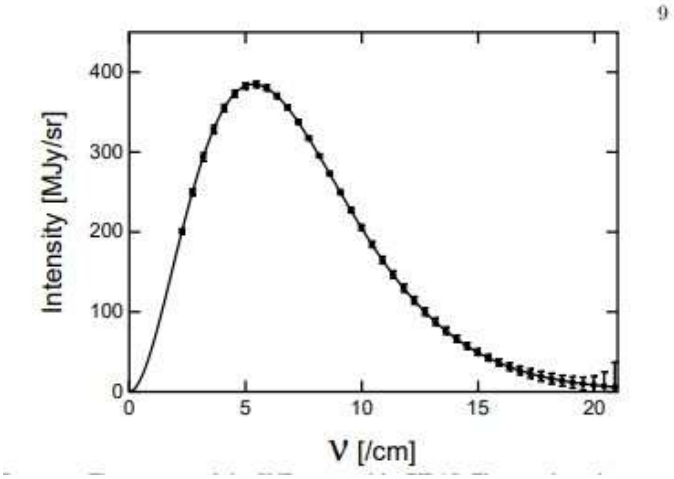

Figure 1.2 Plot of the CMB spectrum from COBE FIRAS. CMB spectrum measured by COBE FIRAS. The errors on this measurement are smaller than the thickness of the line. This measurement placed 95% confidence limits on distortion parameters, however the expected measurement value for these distortion parameters is much smaller. Error bars shown are 400σ. (Smoot, 1997)

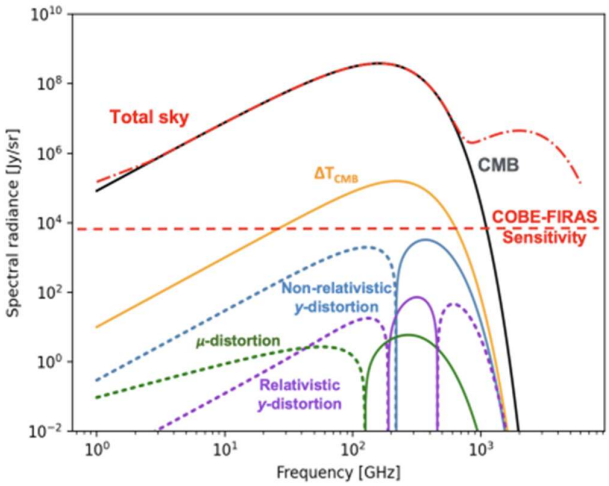

Figure 1.3 The sensitivity of COBE FIRAS compared to the various spectral distortion signals. As can be seen in this figure. The sensitivity of FIRAS was not enough to accurately measure the spectral distortions of the CMB and instead was only able to place upper limits on the values of the distortion parameters (Maffei, et al., 2024).

In the later chapters the initial optical design and analysis of the BISOU instrument is described. Two versions of BISOU are described, a lab-based test bed instrument referred to as the breadboard design and a balloon flight design of the instrument is also described in detail.

1.3 What Spectral Distortions are

With adiabatic expansion, assuming no energy influx into or out of the Universe, we would assume that a blackbody at the start would remain a blackbody, however we have observed that this is not the case. As we predict these spectral distortions exist, we believe something must have either added energy to, or removed energy from, the CMB. Investigation of these distortions gives us insight into the properties and processes of the early Universe.

There are a large number of possible sources of these spectral distortions through processes occurring in the early Universe. In standard ΛCDM cosmology these deviations can be caused by Silk damping of small-scale perturbations. Silk damping, named after British-American astrophysicist Joseph Silk, also known as photon diffusion, is the damping or reduction in anisotropies in the early Universe caused by photons diffusing from hotter denser regions of the Universe to the cooler, less dense regions. This photon diffusion causes the temperatures and

densities in the early Universe to become more uniform. This damping process adds entropy to the thermal plasma in the early Universe and can distort the spectrum of the CMB if it occurs after $z \approx 10^6$ (Sarkar, et al., 2017) and the cooling of photons by electrons and baryons. Other more exotic mechanisms beyond the standard model can include the decay and annihilation of relic particles, primordial magnetic fields, gravitational waves etc (Tashiro, 2014).

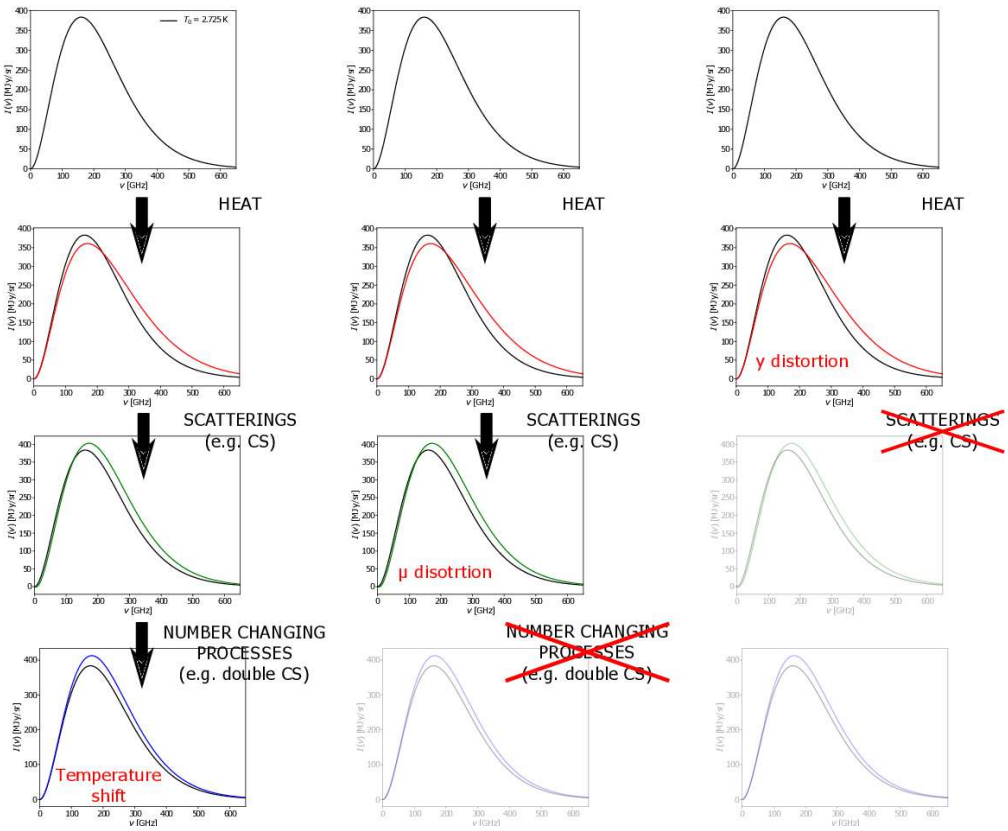

Figure 1.4 Illustration of the different types of spectral distortions (Lucca, 2023). The leftmost column illustrates a full progression of the CMB spectrum through the various processes. Starting off with addition of energy to the CMB (in the form of heat in this case), this increased energy leads to inverse Compton scattering. This causes a shifting of the spectrum towards higher frequency, the red line in the above plot (y-type distortion). Over time through scattering processes this excess energy is distributed among the photons resulting in an overall shift of the spectrum leading to a mu type distortion (green line in above plot). This surplus of photons at higher energies effectively corresponds to a chemical potential. Further scattering processes can eventually drive the chemical potential back to zero and restore a blackbody spectrum shape, this time with an increased temperature from the original spectrum. (blue plot).

Figure 1.4 plots intensity versus frequency for the CMB. The black curves represent a perfect blackbody curve.

Observations show that the CMB spectrum closely matches that of a blackbody. A system with a blackbody spectrum undergoing adiabatic expansion will retain the

blackbody spectrum afterwards. However, it has been observed that this is not the case in the CMB, and a slight deviation exists. For the spectrum to deviate from a blackbody this means that some energy must have been either removed from or added to the system, potentially giving us insight into processes in the early Universe.

Following the evolution in the left column of figure 1.4, we begin with the perfect blackbody spectrum. If for example, some energy is added to the system, we end up with some higher energy photons in the system. This shifts some of the photons from the low energy side of the curve to the high energy tail (red line). Since most of the photons reside at the peak of the distribution, the largest suppression will happen there.

Over time through scattering processes this excess energy is distributed among the photons resulting in an overall shift of the spectrum. (green line in figure 1.4). This distortion is referred to as μ-type or chemical potential distortion. The μ-type distortion is characterised by a deficit of photons at low frequencies and an increment at high frequencies. This surplus of photons at higher energies effectively corresponds to a chemical potential. Given enough time this chemical potential is reduced back to zero and the overall shape of the spectrum returns to a blackbody spectrum although with a higher temperature than the original spectrum (blue line in figure 1.4).

Through double Compton scattering this added energy is distributed through the system equally among the photons, returning it to an ideal blackbody curve, only this time with higher temperature. This shows that the different spectral distortions give insight into different time periods of the evolution of the Universe as the two main types of spectral distortion originate at different time periods (pre-recombination and during recombination).

If we take the case of an expanding Universe, Compton scattering becomes inefficient and the spectrum cannot be returned to a blackbody curve, leaving the μ distortion. (green line in centre column of figure 1.4). μ distortion signals can be created by decaying particles, evaporating primordial black holes, primordial magnetic fields and other non-standard physics examples. The expected value for

μ is roughly $(2.00 \pm 0.14) \times 10^{-8}$ using the predictions from standard ΛCDM cosmology (Chluba, 2016).

As the system continues expanding, Compton scattering becomes less efficient meaning the added energy cannot be redistributed effectively, and the system cannot be changed from the red line in figure 1.4 leaving a shift in photons from the lower energy side of the spectrum to the higher energy side of the spectrum and losing the blackbody distribution. This is known as the *y* type distortion. Since the majority of the photons reside at the peak of the distribution, the largest deviation from the blackbody will happen there. *y* is a parameter that expresses by how much a photon will change its energy due to repeated scatterings. (Lucca, 2023)

Compton scattering becomes inefficient at redshifts $\approx z \leq 5 \times 10^4$ which results in a *y* type distortion remaining. This provides information about the thermal history during recombination and reionization periods in the early Universe. On the other hand, the μ type distortion forms at redshifts of $z \geq 5 \times 10^4$ where Compton scattering is very efficient at redistributing the energy of the CMB photons. A μ distortion cannot form in more recent times, so directly gives us information about the Universe pre-recombination (Chluba, et al., 2019).

1.4 What can we learn from this?

As shown above, these spectral distortions occur due to processes in the early Universe that change the energy distribution of the theoretical blackbody spectrum.

These processes can include Compton scattering from hot gases in the early Universe which is related to the y-type distortion, gravitational waves from cosmic inflation and other energy inducing processes related to the μ-type distortion.

The y-type distortion gives good insight into the scattering processes experienced by photons in the early Universe whereas the μ-type distortion can provide information about other processes such as gravitational waves and is an important piece of evidence for inflation theory.

As described in (Lucca, 2020) spectral distortions can be a useful test of Big Bang cosmology theories such as ΛCDM and any potential modifications of these theories.

The Hubble tension is one of the biggest issues with current theories of the evolution of the Universe. ΛCDM, the currently widely accepted model of the evolution of the Universe, predicts one value of the expansion rate (Hubble parameter) of the Universe based on measurements of the cosmic microwave background from ESA's Planck satellite. This model predicts a value of the Hubble parameter of $H0 = 67.4 \pm 0.5\, km/s/Mpc$ (Cervantes-Cota, et al., 2023).

SH0ES (Supernova H_0 for the Equation of State) was a project to use the "cosmic distance ladder" measurements of Cepheid variables and Type 1a supernova "standard candles" to measure the expansion of the Universe. These two types of stars both have known absolute magnitudes, so by comparing the known absolute magnitudes with the apparent magnitudes the distances to these objects can be calculated. The speed at which they are receding from us can be found from the Doppler shift of their spectra. The Hubble parameter is a measure of the speed of expansion of the Universe versus distance to objects. So, from these standard candle measurements of speed and distance, a value for the Hubble parameter can be found.

The SH0ES project gave a value of H0 of $73.04 \pm 1.04 km/s/Mpc$. This value and the value found from ESA Planck data are not in agreement. (Cervantes-Cota, et al., 2023)

Modifications to ΛCDM theory have been proposed to solve this problem. One such idea is EDE or "Early Dark Energy", which adds a new dark energy variable in the early Universe. This model has been shown to reduce the discrepancy in the Hubble parameter measurements when analyzed with CMB measurements from Planck, Baryon Acoustic Oscillation, Pantheon supernova data and data from SH0ES (Herold & Ferreira, 2022).

Lucca uses spectral distortions as a test of the accuracy of these modifications to ΛCDM cosmology. By comparing the EDE posterior distributions in figure 1.5 below with and without the inclusion of spectral distortions it becomes clear that the limits now placed on the value of H_0 mean that it is no longer compatible with the SH0ES value anymore. This shows that EDE, while initially promising, will not solve the Hubble tension as the inclusion of the spectral distortions in the data show

that the results are no longer consistent with previous data from SH0ES . (Lucca, 2020).

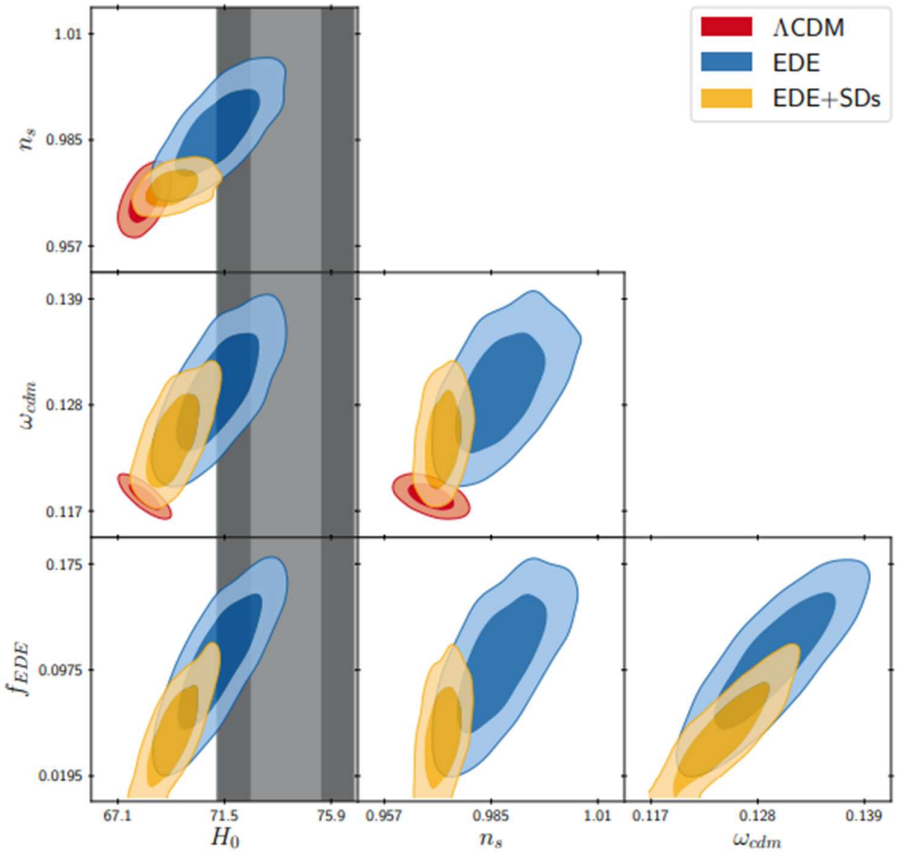

Figure 1.5 posterior distributions of cosmological parameters. ΛCDM (red) and EDE (blue and orange) predictions of the different parameters. The grey band represents 68% and 95% confidence limits for the Hubble parameter H_0. The Hubble tension/disagreement can be seen from the fact that the values given by the ΛCDM model do not agree with data from SH0ES. In the bottom left plot, different confidence values for fEDE (the fractional contribution of EDE to the total energy) are plotted versus confidence values for H_0. The addition of the EDE model initially appears to be a solution to this problem, as the blue section (predictions for H0 with the addition of EDE) of the plot now intersects with the grey band (68% and 95% confidence levels for the H0 values from SH0ES). However once spectral distortions are taken into consideration (the yellow section of the plot) EDE is no longer compatible with the SH0ES value anymore. Plot is from (Lucca 2020).

1.5 BISOU Science Goals

The huge potential for science with CMB spectral distortions was recently mentioned in the NASA 30-year roadmap study, where improved characterisation of the CMB spectrum was declared as one of the future targets (Kouveliotou, et al., 2014).

BISOU plans to use increased sensitivity and spectral coverage compared to previous missions to measure the spectral distortion levels to three orders of magnitude fainter than the limits imposed by the original COBE/FIRAS measurements. The BISOU optical layout as well as PIXIE are described in more detail in chapter 2.

The below table gives predicted detections (from (Coulon, et al., 2024)) for the BISOU balloon borne interferometer mission, along with FOSSIL a proposed space mission for the ESA M7 call in 2022/2025, for the y and μ spectral distortion parameters, and also for A_{CIB}, the absolute intensity of the CIB monopole.

These SNR are calculated by photometric modelling of the specific instrument concept being discussed, along with modelling of foreground emissions. Further described in (Coulon, et al., 2024), the photometric model incorporates different instrument system choices and associated parameters derived from the 2011 PIXIE mission proposal. The foreground emission model uses data from the Planck mission to estimate the different sources of foreground emission. The sky average spectral radiance relative to the assumed CMB blackbody can be described by:

$$\Delta I_\nu = \Delta B_\nu + \Delta I_\nu^y + \Delta I_\nu^{rel-tSZ} + \Delta I_\nu^\mu + \Delta I_\nu^{fg} \tag{1.3}$$

Where ΔI_ν represents the deviation of the true CMB spectrum from that of a blackbody with temperature $T_0 = 2.726\ K$; ΔI_ν^y is the contribution from the y-type distortion; ΔI_ν^μ is the contribution from the μ-type distortion, and Δ_ν^{fg} is the sum of all foreground emissions. Using the photometric model combined with the sky emission model the total NEP on the detectors can be calculated, then with the assumption of the instrument being photon noise limited, an estimate of the sensitivity can be obtained. The full estimation process is further described in Coulon et al, 2024.

MISSION	Y	μ	A_{CIB}
BISOU (with dichroic at 500 GHz)	5.6	0	2.8
BISOU (no dichroic)	1.2	0	0.7
FOSSIL	186	1	76

Table 1.1 Predicted detections for BISOU and FOSSIL (Coulon, et al., 2024). BISOU is expected to be able to detect the y distortions with a 5.6σ significance. BISOU will be unable to measure the μ-type distortion.

Results for a sample configuration for BISOU (explained in chapter 2) are shown in Table 1.1. This gives signal to Noise ratios of 5.6σ for the y-distortion and an SNR of 2.8σ for A_{CIB} – the amplitude of the Cosmic Infrared Background. This represents an improvement of more than a factor of 20 compared to results obtained from COBE-FIRAS. (Maffei, et al., 2021).

"The COBE-FIRAS limit, $|y| < 1.5 \times 10^{-5}$ (95% C.L.), is roughly one order of magnitude larger than the expected signal, $y \approx 2 \times 10^{-6}$" (Maffei, et al., 2024). This demonstrates the need for higher sensitivity, and also good calibration processes with regard to background emissions.

Signals from μ-type distortions will be even fainter ($\mu \approx 2 \times 10^{-8}$) and so it is not predicted that BISOU will be able to measure them.

At the lower end of the measurement range (below 70 GHz), the largest contributions to the foreground emissions are from synchrotron emission, free-free and anomalous microwave emissions. Cosmic-ray electrons in the interstellar magnetic field emit the synchrotron radiation that accounts for most of the continuum emission from our Galaxy at frequencies below about 30 GHz. Free-free emission refers to Bremsstrahlung from interstellar plasma (NASA Goddard Space Flight Centre Astrophysics Science Division, 2021). The higher end foregrounds (above 100 GHz) include sources such as the Galactic thermal dust, cumulative redshifted emission from distant galaxies (the Cosmic Infrared Background (CIB)) and thermal dust emissions.

It is crucial to have reliable models of all the emissions that will be much stronger than these signals in order to properly subtract them (Maffei, et al., 2021).

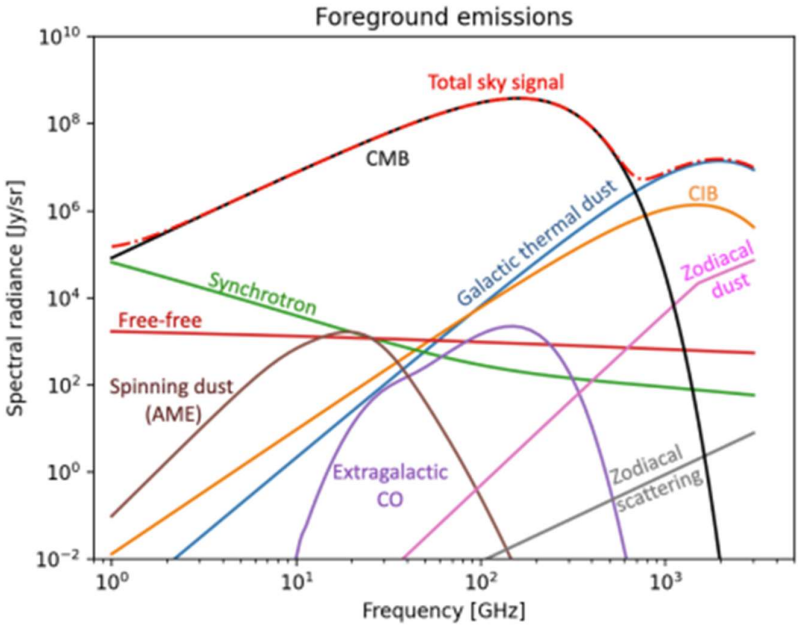

Figure 1.6 Figure from Maffei et al, 2021, showing the intensity of the different foreground emissions compared to the CMB intensity. As the BISOU measurements will be targeting the CMB spectrum, these other foreground emissions need to be taken into account and removed

2 Chapter 2: BISOU Instrument Concept

2.1 Nulling Polarising Interferometer

BISOU is a balloon instrument concept currently in development proposing a Fourier transform spectrometer to measure spectral distortions in the CMB radiation.

As an interferometer, BISOU will not be directly looking at the absolute measurement of the spectrum of the CMB but will instead be focused on "differential interferometry". It will be measuring the difference between the CMB signal from the sky and a reference blackbody source held on board with precise temperature control. This differential measurement will indicate any spectral distortions present in the measured CMB signal from the sky probing any special distortion arising in the early interactions in the Universe. BISOU optics closely follow the NASA PIXIE designs and concepts. PIXIE (Kogut, et al., 2020) had various iterations of designs but was not funded and so BISOU hopes to use the concept and detectors originally proposed for PIXIE.

A nulling polarization interferometer has two beams with a path length offset by $\frac{n\lambda}{2}$. This offset means that the equivalent peak locations from one beam line up with the equivalent troughs from the other beam resulting in destructive interference. If this is done with two identical beams, then total destructive interference will occur and the beam power at the output will measure as 0. However, if the two beams are not identical, then only the identical beam components will interfere and at the output will be the difference between the two input beams.

Light is directed into the FTS column either from the sky via the telescope or from the calibrator. This radiation is then incident on the first polarizing grid A, which sets the instrument's polarisation basis, transmitting the y component of the E-field polarization and reflecting the horizontal component (x). After further reflections Polariser grid B is oriented at 45° relative to polariser A and mixes together the two beams. The middle mirror is a moving mirror which injects an optical phase delay. Next the grid C has the same orientation as grid B and separates the polarizations. Lastly grid D has the same orientation as grid A and again splits the two polarizations before it enters the horns and detectors. Radiation is then reflected

into pyramidal horns. At the back of each horn, two bolometers are mounted orthogonally with their polarization axes giving simultaneous measurement of both polarization states for the sky beam and the calibrator beam. Symmetry in the optical paths is important to keep the paths as identical as possible.

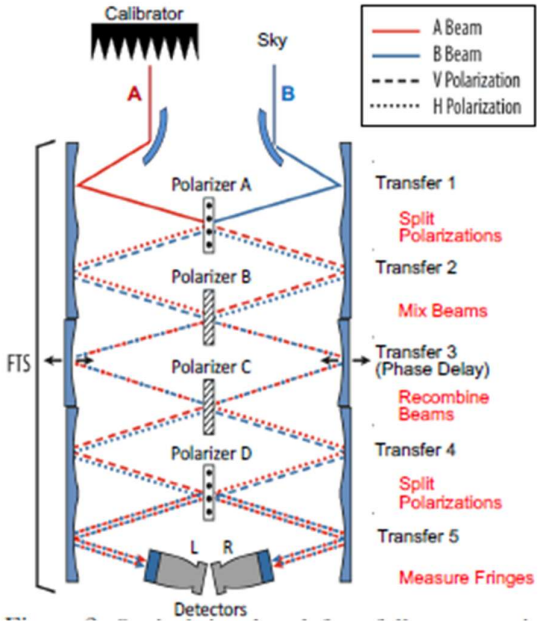

Figure 2.1 Diagram of sample BISOU layout. This is based on the original PIXIE designs and proposes the same techniques to measure spectral distortion (Kogut, et al., 2020)

The movement of the middle mirror back and forth causes the beam interference to create a fringe pattern which has an amplitude dependent on the optical phase delay between the two interfering beams.

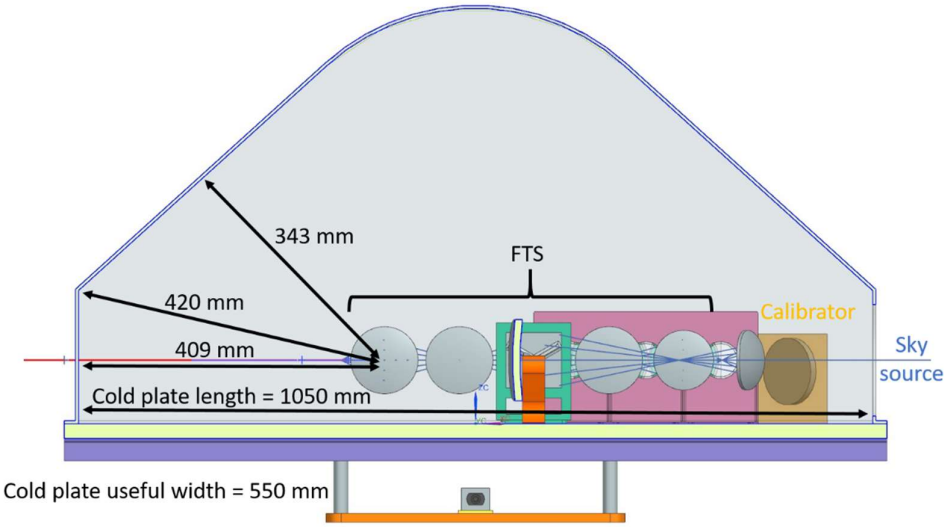

Figure 2.2 Sample BISOU system in gondola (CAD drawing from members of the BISOU consortium).

The size of the optics is limited by the size constraints of the cooling system and balloon gondola. Figure 2.2 shows a sample system enclosed in the gondola. The maximum total width for the system is 550 mm. The maximum distance of the horns below the FTS is ≈400 mm. The maximum allowed size for the primary mirror is limited to 150 mm radius, and the maximum allowed FTS mirror size (and thus mirror spacing for the FTS column) is 50 mm, although a nominal value of 45 mm is used for the individual mirror diameters in the FTS column.

In this thesis two different versions of BISOU are outlined, the breadboard version and the ultimate flight version. The breadboard version is a simpler design than the flight model and is designed to be the lab testbed for the full system. The telescope is kept in the same optical plane of the FTS mirrors as sown below. The flight model needs to have a different telescope configuration due to the flight gondola configuration. The BISOU consortium received funding from Ile de France région (DIM-ORIGINES) and CNES (Centre National d'Études Spatiales) to construct the lab testing breadboard instrument concept for BISOU. This Breadboard version would be constructed initially and used as a testbed for the final BISOU flight instrument design. The Breadboard version was prioritised for the simulation and design described in this thesis. The breadboard and instrument designs follow the same general design concepts with the most significant difference being the orientation of the telescope for the BISOU instrument.

For the breadboard the telescope is kept in the same optical plane as the FTS column of mirrors. This was due to space constraints in the cryogenic enclosure and cooling system. The FTS column has mirrors of alternating sizes 30 mm and 45 mm. This was found to have no effect on the truncation of the beam as the beam will be converging and diverging on alternate mirrors in the path. Truncation values for both potential FTS layouts were identical. This also reduces the propagation distance from the centre of one mirror to the centre of the next to 215.5 from 223 mm and leads to a more compact design. Figure 2.3 shows a sample breadboard design.

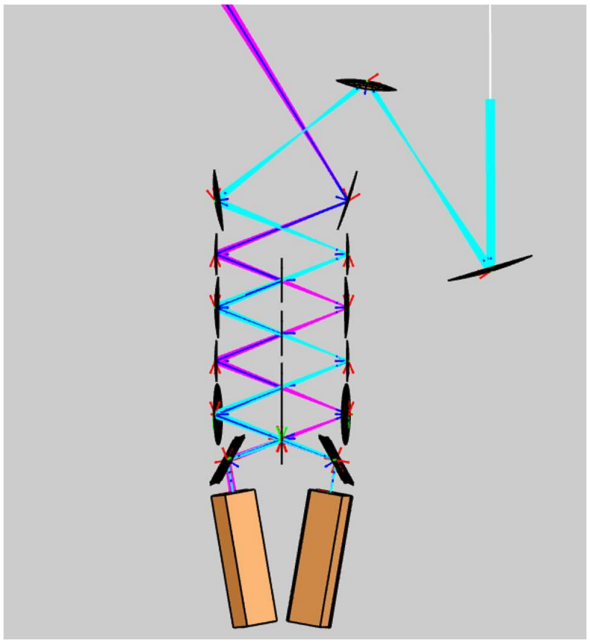

Figure 2.3 Sample BISOU breadboard design. The general concept is the same as for the instrument version with the main difference being the orientation of the telescope. The horns are shown on the bottom of the figure with the optical path to the calibrator shown with pink rays and the path to the sky shown in cyan coloured rays.

The main BISOU instrument has a similar optical layout to the breadboard design with the main change being the reorientation of the telescope to be 90 degrees out of the plane of the FTS.

The instrument design as a result has a modified secondary mirror and primary mirror to reflect the beam out of the plane. The instrument FTS column has all mirrors set to 45 mm.

Figure 2.4 shows the BISOU instrument design

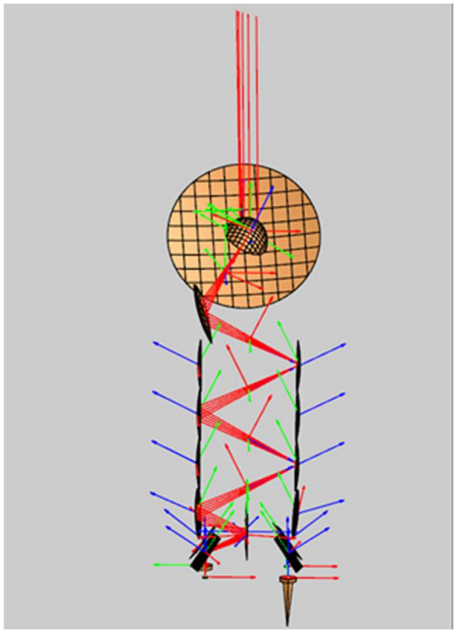

Figure 2.4 BISOU instrument design, the main difference from the breadboard design above is the reorientation of the telescope to be out of the plane of the FTS, this is due to volume constraints in the gondola.

BISOU has been adapted from the PIXIE (Primordial Inflation Explorer) mission proposal which was a mission concept designed “to measure the energy spectrum and linear polarization of the cosmic microwave background (CMB)”. (Kogut, et al., 2025).

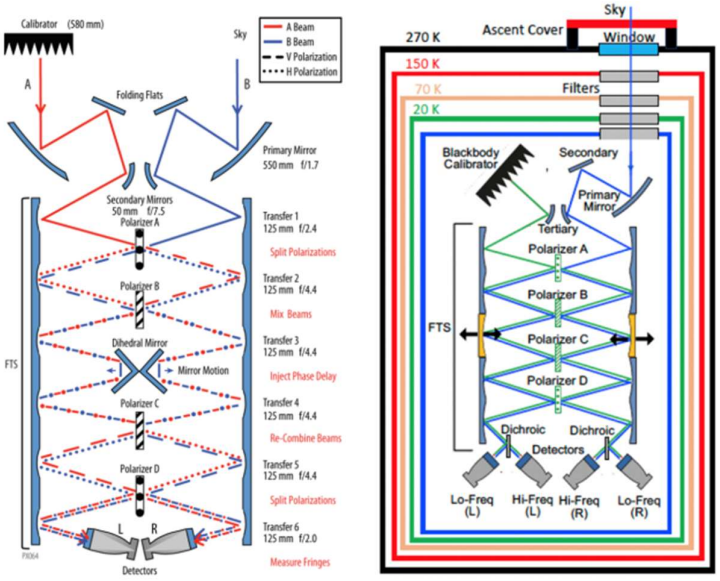

Figure 2.5 The original PIXIE mission concept on the left and the BISOU mission concept on the right. Differences include the addition of the dewar window and spectral filters, only one input telescope, and the addition of dichroics leading to 2 sub-bands and 4 focal planes. Diagram from (Maffei et al 2024).

Figure 2.5 shows the initial PIXIE design and also a sample BISOU optical design. The main differences are the fact that BISOU only has one input telescope, the addition of dichroics to split the beam into two frequency bands, a dewar window and spectral filters. The initial frequency split was set to 500 GHz, but more recent calculations show that a frequency split around 300 to 350 GHz would be best. (Maffei, et al., 2024) The original PIXIE design had two telescopes, and a calibration source, giving 3 modes of operation. In the first two modes, one optical path sees the sky, and the other sees the calibration source so the difference between the sky and the reference blackbody can be recorded.

The third mode is used for calibration and has both optical paths to the sky. The ability to use both telescopes in PIXIE removed some of the systematic effects on the output. PIXIEs design is highly symmetric which enables its operation as a nulling polarizing interferometer, this helps control instrumental effects and improves sensitivity. PIXIE is sensitive to the polarization of the sky emission. The use of PIXIE as an interferometer nulls all the unpolarised emissions incident on the instrument, so that the resulting fringe patterns only respond to the sky polarization. The resulting nulling interferometry greatly reduces detection of systematic errors from unpolarised sources. (Kogut, et al., 2011)

Either input can view the sky or a temperature-controlled absolute reference blackbody calibrator. PIXIE has two off-axis primary mirrors of 550 mm in diameter, a folding flat mirror and a 50 mm secondary mirror to direct the beams through the FTS. The FTS column contains six mirror pairs. PIXIE contains 4 polarising grids. The first polariser, polariser A transmits the vertical polarisations of the beams and reflects horizontal polarisations. Polariser B is oriented at 45 degrees to polariser A and mixes the polarisation states. The movable mirror moves back and forth to inject a phase delay. These beams then recombine and interfere at polariser C. Polariser D splits the beams again and they are directed to the feed horns.

PIXIE's ability to use multiple modes of operation for calibration purposes allows more easy removal of instrumental effects from the final measurements, and account for any asymmetry in the optical paths. BISOU does not have the same ability and so more care will be needed in calibration of the optics. (Kogut, et al., 2025)

The fringe pattern at the detectors can be expressed as a constant term plus a modulated term which is proportional to the Fourier transform of the difference spectrum between the x-polarisation from one beam and the y-polarisation from the other beam. Each of the four detectors measures a fringe pattern between the orthogonal polarisations of the two input beams. Therefore, the variable part of the measured output at the detectors will be the difference between the signal from the sky and the signal from the calibrator, thus giving a differential measurement between the sky signal and an ideal blackbody. (Maffei, et al., 2024)

2.2 BISOU Instrument Design

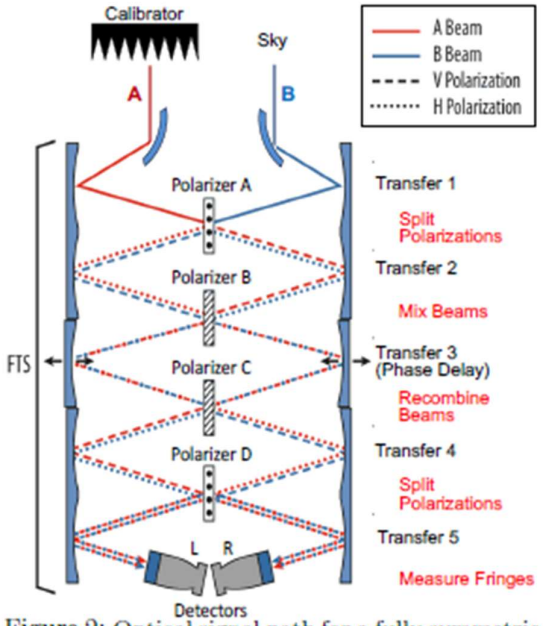

Figure 2: Optical signal path for a fully symmetric Fourier Transform Spectrometer (FTS).

Figure 2.6 Example instrument layout for BISOU (Kogut, et al., 2020).

Above is a design layout of the BISOU instrument. Two beams enter the FTS column, one from the blackbody calibration source (calibrator in diagram) and one through a telescope from the sky.

The polarisations of the beams are split at polariser A into the orthogonal polarisations. This polariser reflects the horizontally polarised components of Beam A, and Beam B, while transmitting the other components.

These beams are combined at polariser B, where each side of the optical path now contains both polarisations of both the A and B beams.

The movable mirrors at the third reflection point inject a phase delay into the beams. These beams create an interference pattern which is dependent on the optical phase delay between the two beams. These beams then combine/interfere at polarizer C. Polariser D splits the polarizations again, and the interference pattern is measured at the horns/detectors. As was the case for the PIXIE design described previously, BISOU will use nulling polarising interferometry. This means that the interference pattern present at the detectors is sensitive only to the polarisation of

the incoming signal from the sky. This helps eliminate systematic effects and improves the overall sensitivity of the instrument.

BISOU uses wire grid polarisers. Wire grid polarisers consist of a grid of very fine electrically conductive wires of a certain thickness, spaced evenly apart. The field components parallel to the wires induce a current on the wires. This current then reflects the incident field in that orientation. The field components perpendicular to the wires does not induce a current and so is able to pass through unimpeded. This means that the beam after propagation through a wire grid polariser will be polarised perpendicular to the orientation of the wires in the polarisers, and the reflected component of the beam will be polarised parallel to the orientation of the wires.

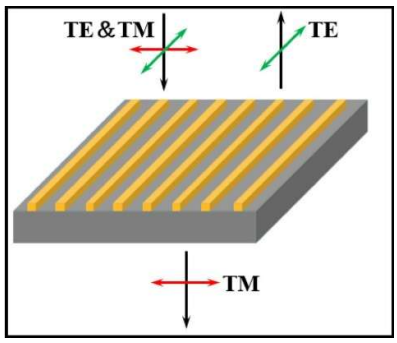

Figure 2.7 Diagram of a wire grid polariser. Initially the light is unpolarised with both vertical components, and components at an angle on the left side of the image. After transmission through the wire grid only the beam components perpendicular to the wires remains (Chen, et al., 2025).

The power at the detectors as a function of frequency ω and mirror position z may be written as:

$$P_{Lx} = 1/2\int\left\{\left(E_{Ax}^2 + E_{By}^2\right) + \left(E_{Ax}^2 - E_{By}^2\right)\cos\left(4z\omega/c\right)\right\}d\omega \qquad (2.1)$$

$$P_{Ly} = 1/2\int\left\{\left(E_{Ay}^2 + E_{Bx}^2\right) + \left(E_{Ay}^2 - E_{Bx}^2\right)\cos\left(4z\omega/c\right)\right\}d\omega$$

$$P_{Rx} = 1/2\int\left\{\left(E_{Ay} + E_{Bx}^2\right) + \left(E_{Bx}^2 - E_{Ay}^2\right)\cos\left(4z\omega/c\right)\right\}d\omega$$

$$P_{Ly} = 1/2\int\left\{\left(E_{Ay}^2 + E_{Bx}^2\right) + \left(E_{Ay}^2 - E_{Bx}^2\right)\cos\left(4z\omega/c\right)\right\}d\omega$$

$$P_{Ry} = 1/2\int\left\{\left(E_{Ax}^2 + E_{By}^2\right) + \left(E_{By}^2 - E_{Ax}^2\right)\cos\left(4z\omega/c\right)\right\}d\omega$$

(Kogut, et al., 2020)

Where P is the total fringe pattern (with L and R indicating which side of the optical path the beam is being measured at), E_{Ax} and E_{Ay} are the electric fields of the A beam in the x and y directions, E_{Bx} and E_{By} are the electric fields of the B beam in the x and y directions. ω is the frequency and z is the mirror position. The fringe pattern $P(z)$ can be measured at each detector as a set of N mirror positions to recover the overall frequency spectrum of the incident radiation.

Where S_ν represents the frequency dependent sky signal and S_k represents the amplitude of the sampled interference fringe pattern, the two are related by a Fourier transform

$$S_k = \int S_\nu \exp\left(\frac{2\pi i z_k \nu}{c}\right) \partial \nu \qquad S_\nu = \sum_{k=0}^{N_z - 1} W_k S_k \exp\left(\frac{2\pi i k Z}{c N_s}\right) \tag{2.2}$$

(Kogut, et al., 2020)

This interference pattern then tells us about the difference between the sky signal and the reference beam – thus we can measure potential spectral distortion of the sky beam relative to the reference beam. The ability of such an instrument to measure the spectral distortions effectively is dependent on the frequency range covered. BISOU is planned to operate in a frequency range from 90 GHz to 1.5 THz.

This frequency range is chosen to cover the dominant frequency range of the CMB as well as higher frequency signals of foreground objects. These constraints set the high frequency limit to 1.5-2THz. The photon noise contributions were found to be increasing with increased ν_{max} however the measurement of the science goals is dependent on the ability to go to high frequencies. Therefore, a trade-off needs to be reached in order to optimise the signal to noise ratio for each parameter. (Maffei, et al., 2021)

A dichroic is used to split the frequency range into two channels. Photometric modelling indicated that due to a high contribution to the photon noise from the high frequency end of the spectrum, the sensitivity of the instrument can be improved by the use of a dichroic, splitting the detection range into 2 sub-ranges. The low frequency range would be best suited for measurements of the spectral distortions whereas the high frequency band would be utilised for measurement and

removal of foreground emissions. Recent calculations show that a frequency cutoff of roughly 350 GHz between the two bands would be best (Coulon, et al., 2024).

Another consideration of the instrument's ability to measure spectral distortions is the spectral resolution. The spectral resolution of an interferometer is determined by the maximum path length difference between the two optical paths i.e. the amplitude of the movement of the moving mirror. The spectral resolution in cm^{-1} is, from Li et al,

$\frac{0.5}{OPD_{\max}}$ where OPD_{max} is the maximum path length difference between the two beams in centimetres. The current chosen value for OPD_{max} is 10 mm or 1 cm, giving a spectral resolution for the system of $0.5\ cm^{-1}$ or 15 GHz.

An estimate of the required cooling level for the instrument was developed using a photometric model which only included the dewar window and a minimum of two spectral filters. The emission of all the components in the system was modelled as a blackbody emission at the specified temperature. The load on the detector is estimated by adding the power contributions of the optical components as well as the contributions from the sky. The load on the detector can be described by the equation 2.3 below:

$$P(\nu,T) = \int_{\nu_{\min}}^{\nu_{\max}} eff\,(\nu)\, A\Omega(\nu)\, \varepsilon(\nu,T) B(\nu,T) d\nu \tag{2.3}$$

Where AΩ is the throughput of the multimoded optics, eff is the transmission efficiency of the optical system and B is the blackbody function. The emissivity is taken as a constant.

The NEP or Noise Equivalent Power value gives insight into the cooling requirements of the instrument, as it gives a lower bound on a signal that can be picked up by the detectors. This signal could refer to the actual sky signal we are interested in, or any unwanted signals such as thermal emission from the system itself. The NEP is given as a function of frequency in $\frac{W}{\sqrt{Hz}}$.

Essentially the NEP expresses the minimum detectable power per square root of bandwidth of a given detector. It's a measure of the weakest optical signal that can

be detected. The Noise equivalent power can be seen as the weakest input signal power that can produce a signal to noise ratio of 1. This can vary with incoming frequency and so the NEP is given as a function of $\sqrt{Hz}$ (Leclercq, 2007).

For calculation of the NEP for BISOU, the power received by the detector is integrated over the full range of frequencies. For a worst-case scenario estimation when the optical path difference is null, the power is integrated over the full observation frequency range. The NEP can then be calculated by combining in quadrature the photon NEP from the signal, and the NEP of the detector itself which is assumed to be four times lower. It is assumed that the majority contribution to the overall NEP is the photon contribution. Depending on assumptions made about the temperature and emissivity of the optical components the total NEP can be calculated to be on the order of a few x $10^{-16} W\ Hz^{-\frac{1}{2}}$ for a space mission or $10^{-14} W\ Hz^{-\frac{1}{2}}$ for the BISOU balloon borne instrument. The calculated NEP for a sample balloon instrument is high enough to use detectors cooled to a temperature around 300mK. (Maffei, et al., 2021). This cooling requirement will allow the use of a 3He sorption cooler.

The choice of detector technology is dependent on the allowable detector NEP. For BISOU depending on the assumptions and instrument parameters, photometric models show that “a detector NEP on the order of a $few \times 10^{-16}$ is enough for the instrument to be photon noise limited", (Maffei, et al., 2024) allowing the use of various detector technologies.

Resistive detectors developed by NASA-GSFC for the PIXIE mission proposal can be adapted and optimised for BISOU and so are the baseline choice.

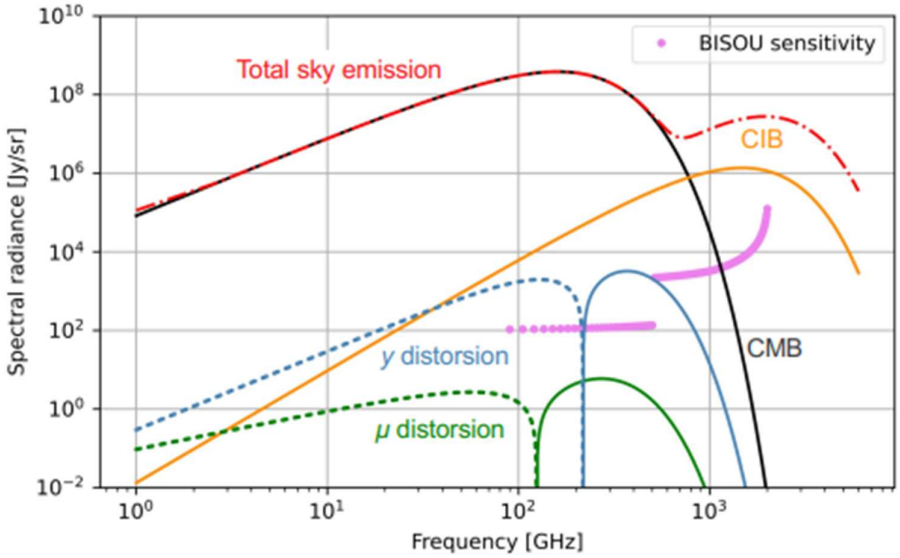

Figure 2.8 Sensitivity of the proposed BISOU instrument compared to the various spectral distortion signals shown previously in figure 1.6. Calculations indicate that BISOU should be able to detect the CMB y distortion. BISOU will not have the necessary sensitivity to detect the μ distortion (Maffei, et al., 2024). *The pink lines on the plot indicate the predicted sensitivity from section 1.4. It can be seen that it should be possible to detect the y-type distortion with BISOU. Detection of the μ-type distortion will not be possible.*

3 Chapter 3: GRASP and Physical Optics

3.1 Physical Optics

Generally, the first approximation used for calculating reflection and refraction of optical wavelength light passing through optical components is geometrical optics. Geometrical optics does not account for the diffraction of light and assumes that light radiating from a source travels along straight-line paths or "rays", effectively with a wavelength of zero. The paths of these rays can be modelled using simple mathematical relations for reflection/refraction.

Ray tracing is routinely used for optical wavelengths but becomes less accurate for longer wavelength radiation as is the case for BISOU operating at a frequency range of 90 to 2000 GHz. Physical optics is a method of optical simulation where, instead of using light rays to simulate reflection and refraction as in geometrical optics in straight line ray paths, the light is modelled as an electromagnetic wave which can experience physical effects such as diffraction, divergence, polarisation and interference where the ray approximation is no longer useful.

Radiation integrals give electric and magnetic field intensities at an observation point P for a known distribution of J (electric) and M (magnetic) currents. Physical optics starts with a given current distribution that radiates, or the measured radiation pattern from an antenna. When an object is placed in this field the PO method calculates the induced currents on the object. The surface is then broken up into constant current surface patches. As the patch size decreases the physical optics simulations converge towards the correct solution.

Scattering from an object can therefore be calculated using the following steps:

1. Start with a source field comprising of electric and magnetic field components **E** and **H**.
2. Calculate the equivalent currents **J**, **M** induced on the scatterer by

source. (Milligan, 1985)

$$J_s = \hat{n} \times H_1 \tag{3.1}$$

$$M_s = -\hat{n} \times E_1 \tag{3.2}$$

3. Use the radiation integrals to find A (the magnetic vector potential) and F (the electric vector potential):

$$A(r) = \mu \iint J_s(r) G(r, r') ds' \tag{3.3}$$

$$F(r) = \varepsilon \iint_s M_s(r) G(r, r') ds' \tag{3.4}$$

where $G(r, r') = \dfrac{\exp(-jkR)}{4\pi R}$ and $R = |r - r'|$ (Milligan, 1985)

and then calculate the **E**, **H** fields at an observation point P resulting from **J** and **M**.

The magnetic vector potential A can be used to determine the near fields, these are: (Milligan, 1985)

$$H(r) = \frac{1}{\mu} \nabla \times A(r) \tag{3.5}$$

$$E(r) = -j\omega A(r) + \frac{\nabla(\nabla . \mathrm{A})}{j\omega\mu\varepsilon} \tag{3.6}$$

The electric vector potential F can also be used to derive the near field: (Milligan, 1985)

$$H = -j\omega F + \frac{\nabla(\nabla . F)}{j\omega\mu\varepsilon} \tag{3.7}$$

$$E = -\frac{1}{\varepsilon} \nabla \times F \tag{3.8}$$

The steps so far have made no approximations about the system. The approximations become important in step 2 above. If the boundary of the surface is perfectly electrically conductive (PEC) then the PO approximation says that H_1^{inc} and H_1^{ref} at the boundary are in phase and have the same amplitude (the surface is a perfect reflector) so:

$$J_s^{PO} = 2\hat{n} \times H(r') \tag{3.9}$$

And that the tangential component of E on the surface is 0: $M_s^{PO} = 0$. PO assumes that the currents go to zero on parts of the surface that are not directly illuminated. The scatterer surface (of any shape) is subdivided into many tangential planar surfaces, and the PO calculations are applied to each. This approach is valid as long as the dimensions and radius of curvature of the scatterer are sufficiently large.

Physical theory of diffraction is also included in the calculations performed by GRASP unless the surface has special electrical properties. PTD models the diffraction of the beam at the edge of the scatterers. PTD is an extension of physical optics theory used to model the diffraction of the beam at the edges of the scatterer.

The main physical optics process uses geometrical optics to estimate the surface current. This current is then used in radiation integrals to calculate the scattered field from the reflector. Physical Optics simulations often work very well for electrically large and smooth bodies (i.e. where the size of the components is large compared to the wavelengths of the radiation being studied). However, despite the huge successes of Physical Optics, the use of an approximate current can lead to inherent inaccuracies. The physical theory of diffraction is an important high frequency technique that addresses this problem. (Paknys, 2016)

Physical optics is inherently a high frequency simulation method, Kobayashi,2020 states, "in conventional PO, the radiation integral for the scattered field is calculated by employing a Geometric Optics approximation for the currents induced on the surface, which is assumed to be an electrically large plane; hence, the PO method is also a high-frequency method".

This is an important difference from GBMA which is a theory that can be used at lower frequencies. As a high frequency approximation PO theory assumes that the electromagnetic current is zero in the shadowed area of the scattering object. The electromagnetic current distribution in the transition region is also different from the actual one, so this limits the application range of PO (Kobayashi, 2020). Since the PO method is calculated regardless of the shape and material of the object in the shadow area the same result is obtained for different shapes.

In PTD (Physical Theory of Diffraction), a transition current is introduced at the boundary region. PTD was proposed by Ufimtsev and Keller. When PTD was first introduced it was only applied to surfaces with edges, however, recently the method has also been applied to smooth impedance objects. The induced currents on a perfectly conducting infinite plane surface illuminated by an arbitrary incoming field are given by the formula:

$$J^e = 2\hat{n} \times H^{inc} \tag{3.10}$$

Where J^e is the induced electric current, $\hat{n}$ is the surface normal (pointing out of the illuminated side of the surface) and H^{inc} is the incident magnetic field. This equation is a reasonable approximation for induced currents on a curved scatterer as long as the radius of curvature and dimensions of the scatterer are sufficiently large relative to the wavelength of the incident radiation. For simple scatterer designs the approximations used in GRASP can be used down to sizes of roughly 5 wavelengths in diameter (GRASP user manual). This cutoff is sufficient for the systems illustrated in this thesis but show the potential limitations of the physical optics simulations for lower frequency beams.

The grid over which the physical optics integrations are carried out is defined by two variables, po1 and po2. These define the number of points in the integration grid. If these values are too low the result of the integration will be inaccurate as the integral will not converge towards a correct result. However, if the number of points is too high the computation time for the simulation will greatly increase without a corresponding increase in accuracy. GRASP performs some checks to automatically determine the number of PO points required for each scatterer, so these values do not need to be defined by the user.

For a focused reflector with a circular rim, GRASP can estimate the number of necessary PO points from the following:

$$po1 = n\,\mathrm{int}(z / 2.4),\ po2 = n\,\mathrm{int}(z) \tag{3.11}$$

where:

$$z = 1.09\pi \frac{D}{\lambda} \sin\theta_0 + 10\,, \tag{3.12}$$

D is the reflector diameter, λ is the wavelength, θ_0 is the output angle from the beam centre where the integral will converge, and $n\,\mathrm{int}$ gives the nearest integer value to the given argument. As the PO analysis divides the surface into a number of smaller patches the computational cost of the analysis rises rapidly depending on the size and geometry of the scatterer.

In GRASP the surfaces can be defined in a number of ways: The two methods used in this project were Second Order Polynomial and Conic Mirror Surface.

The Second Order polynomial definition is the most generalised case. The surface is defined by a second order polynomial of the form:

$$A_{xx}x^2 + A_{yy}Y^2 + A_{xy}xy + A_x x + A_y y + A_c = A_{zz}z^2 + A_{xz}xz + A_{yz}yz + A_z z \tag{3.13}$$

This is the most generalised case, and this definition can be used to describe a large range of scatterer geometries such as paraboloids, hyperboloids and ellipsoids.
GRASP also contains other surface definitions. Also used in this research was the conic surface definition. The conic mirror surface definition uses 4 parameters to describe the surface.

*r*1: The distance from the reflection point to the first focal point
*r*2: The distance from the reflection point to the second focal point
theta_i: The angle from the surface normal to the axial ray
theta_n: The direction of the surface normal at the reflection point given as the angle from the z-axis to the normal

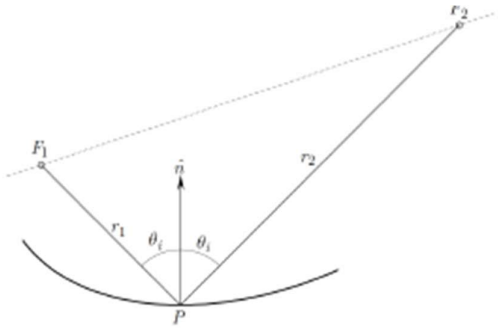

Figure 3.1 Diagram illustrating the parameters necessary for GRASPs conic mirror surface definition. Diagram is from the GRASP user manual.

The rims of the reflectors are defined in a plane perpendicular to the z-axis of the reflector coordinate system. This is important as it leads to some small differences

when implementing the different mirror surface geometries. The z-axis for the SOP mirror definition is oriented parallel to the incoming beam/input angle of the mirror, whereas for the conic mirror surface the z-axis is oriented as a surface normal, perpendicular to the mirror surface. This means that for two mirrors defined with the two different methods, the z-axes are at an angle relative to each other and will lead to a slightly different rim definition due to a projection effect. This becomes more apparent for more complicated mirror definitions with larger angles of throw but is still a factor for the smaller mirror definitions. Elliptical rims are defined in the reflector coordinate system by the ellipse:

$$\left(\frac{x-x_c}{a}\right)^2+\left(\frac{y-y_c}{b}\right)^2=1 \tag{3.14}$$

where (x_c, y_c) is the centre of the rim and a and b are the half axes.

Spillover calculations

When the induced currents are being calculated on a reflector, the power contained in the incident field can also be calculated by integrating the Poynting vector over the surface:

$$P=\frac{1}{2}\mathrm{Re}\left(\mathbf{E}\times\mathbf{H}^*\right) \tag{3.15}$$

The total power on the surface can be found by:

$$W=-\iint_B \mathbf{P}\left(r'\right).\hat{\mathbf{n}}\left(r'\right)ds' \tag{3.16}$$

The spillover value is then found as:

$$spillover=10\log_{10}\frac{4\pi}{W} \tag{3.17}$$

Where the factor 4π comes from the fact that GRASP normalises the power to 4π Watts. Because both the electric fields and magnetic fields are used to calculate the spillover the computation time is significantly worse than for calculating the induced currents. However, it is much more efficient to calculate the total power hitting the reflector than to calculate the power in all other directions. A consequence of this spillover definition is that it is cumulative. The spillover on a chosen reflector in a multi scatterer system will include the spillover at all previous

reflectors (GRASP user manual). As a simple check to ensure consistency between the conic mirror surface and second order polynomials, a single mirror was defined in GRASP both using the second order polynomial definition and the conic mirror surface definition. The same rim (radius 30 mm) is used for both. Both have the same angle of throw (38.1 degrees) and the same input (190 mm) and output distances (290.6 mm).

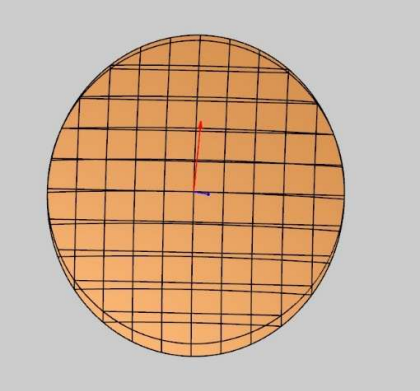

Figure 3.2 Two mirrors of the same focal length and angle of throw defined using the second order polynomial and conic mirror surface definitions in GRASP. It can be seen that the rims for the two mirrors are not identical with one rim experiencing a projection effect relative to the other. This is due to the different z-axis definitions for the two mirror types. The stretched mirror in figure 3.2 is the second order polynomial definition. It can be seen that the rim experiences a projection effect, and the rim is stretched vertically.

Spillover values were recorded for each mirror from the same initial 10 mm radius Gaussian beam at 90 GHz:

Second order polynomial	0.976201
Conic mirror surface	0.970988
GBMA truncation analysis	0.970579

Table 3.1 spillover values for this single mirror example in GRASP, for both the second order polynomial and conic mirror surface definitions of the reflector and also a value from the python truncation analysis code.

There is a difference of roughly 0.6% between the spillover values from the two mirror definitions in GRASP, which is due to the projection effect described previously. The z-axis for the second order polynomial definition is at an angle, the z-axis for the conic surface is normal to the reflector. As the rims are defined relative to the respective z-axes the second order polynomial mirror will experience a projection effect. Both have reasonable agreement with the Python truncation analysis code described in section 5.1, with the conic mirror surface giving slightly more accurate values.

Both these mirror surface definitions were used for the simulations in this thesis, depending on the requirements for the specific mirror. The mathematical description of the surfaces in GRASP means that for specific focal length and angle of throw requirements for the scatterer being designed, the surface may be undefined for the given radius. This means that depending on the scatterer being implemented either second order polynomial or conical surface may need to be used.

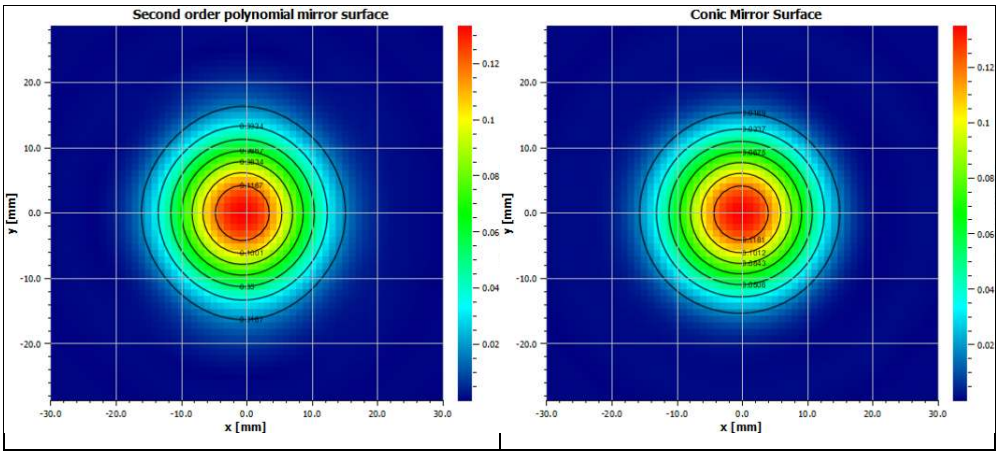

Figure 3.3 Beam plots from a 10 mm initial Gaussian beam reflected from both the second order polynomial mirror and the conic mirror surface. Both beam plots are very similar. Along with the fact that the spillover values from each mirror are similar, this indicates that both mirror definitions are valid for the simulations performed in this thesis, as long as the projection effect of the rim is taken into account when the truncation is being compared. GRASP plots linear plots using "TICRA tools units" which are equivalent to W^0.5.

3.2 GBMA (Gaussian Beam Mode Analysis)

Quasi-optics refers to electromagnetic propagation through optical components whose size is comparable to the wavelength of the light, where the effects of diffraction remain significant because the size of the components when measured in wavelengths is relatively small (Goldsmith, 1998)

GBMA (Gaussian Beam Mode Analysis) uses a quasi-optical expansion of ABCD ray matrices to calculate properties of EM beam along the path. With the assumption that the fundamental mode of the beam being studied is a Gaussian Beam and that the propagation of the beam can be accurately modelled by focusing on this fundamental Gaussian beam mode. It can be shown that Gaussian beams are a valid solution to the Helmholtz wave equation and so are a valid mathematical model of these electromagnetic beams. These Gaussian beams are discussed further in chapter 4

The Helmholtz equation can also be shown to be a solution to Maxwells equations; therefore, this approximation is valid for simulating the propagation of an electromagnetic wave through the optical system. GBMA works by using a modification of ABCD matrix theory to calculate properties of the Gaussian Beam as it propagates through the optical system.

These beam parameters are:

- W – the Gaussian Beam waist, the radial distance from the centre of the beam where the intensity drops to $\frac{1}{e^2}$ or 13.5% of the max value
- R – the radius of curvature of the wave front.
- Φ - the phase slippage.

Using a modification of ABCD matrix theory these beam parameters can be calculated throughout the propagation of the beam.

Laguerre-Gaussian or Hermite-Gaussian beam modes can be used to model truncation of the beam where it is scattered off a reflector that may be too small for a beam of that size and beam loss may occur. This can be a useful estimate of the required mirror sizes for an optical system before a full physical optics analysis is carried out.

Gaussian Beam Mode Analysis is useful in quasi-optical systems where the wavelength of the beam being studied is comparable to the size of the optical components. This is in contrast to Geometric Optics (and thus Physical Optics) which is more suited to situations where the wavelength of the beam is small relative to the scale of the optical system/optical components. A full description of this theory is described in the next chapter.

4 Chapter 4: Gaussian Beam Theory

The quasi-optical beam is modelled as a simple Gaussian with a varying beam radius w, phase radius of curvature R and phase slippage ϕ as a first approximation to modelling a propagating horn antenna field.

The waist radius w of a Gaussian beam is the radial distance from the centre at which the amplitude has dropped to $\frac{1}{e}$ times the max value and the intensity has dropped to $\frac{1}{e^2}$ the max value (Goldsmith, 1998). The waist is the minimum beam radius that occurs at a single location where the beam is smallest in extent.

The phase radius of curvature of a Gaussian beam is the radius of a circle which has a curvature that best approximates the curvature of the wavefront at that point. If the wavefront is flat (i.e. a plane wave), then R is infinite, if the wavefront has a sharp curve, R is small.

The majority of power in the beam is concentrated towards the centre of the beam. The fundamental Gaussian beam is a good approximation of the fundamental mode of the electric field from horn antennas and can be used for initial analysis of diffraction in optical systems like BISOU.

In reality, a long wavelength horn beam has a more complex electric field profile, and the power will not necessarily be Gaussian in profile. This means any simulations performed need to account for electric field profiles where the field does not taper exponentially away from the beam centre, as you need to ensure any optical path allows for the potentially wider beam profiles, but for initial simulations, a Gaussian beam is quite indicative of quasioptical behaviour.

The Gaussian beam can be shown to be a solution to the paraxial approximation of the Helmholtz equation (Goldsmith, 1998):

$$\nabla^2\psi + 2ik\frac{\partial\psi}{\partial z} = 0 \tag{4.1}$$

where: $\nabla^2 = \frac{\partial^2}{\partial x^2} + \frac{\partial^2}{\partial y^2}$

Using a trial solution of the form:

$$u(x,y,z) = A_x(z)\,A_y(z)\exp\left(-\frac{jkx^2}{2q_x}\right)\exp\left(-\frac{jky^2}{2q_y}\right) \quad (4.2)$$

where A_x and A_y are the amplitudes, and q is the complex beam parameter, defined as:

$$q_x = \frac{j\pi w_{0x}^2}{\lambda} + z, \quad q_y = \frac{j\pi w_{0y}^2}{\lambda} + z \quad (4.3)$$

Separating the solution, and with the requirement that it be valid for all x and y gives the conditions:

$$\frac{\partial q_x}{\partial z} = 1, \frac{\partial q_y}{\partial z} = 1$$

As well as:

$$\frac{\partial A_x}{\partial z} = -\frac{1}{2}\frac{A_x}{q_x}, \frac{\partial A_y}{\partial z} = -\frac{1}{2}\frac{A_y}{q_y}$$

The overall field distribution is the combination of the x and y parts giving the normalised form:

$$E(x,y,z) = \left(\frac{2}{\pi w_x w_y}\right)^{0.5} \exp\left(-\frac{x^2}{w_x^{\,2}} - \frac{y^2}{w_y^{\,2}} - \frac{j\pi x^2}{\lambda R_x} - \frac{j\pi y^2}{\lambda R_y} + \frac{j\phi_{0x}}{2} + \frac{j\phi_{0y}}{2}\right) \quad (4.4)$$

In the special case that the beam waists W_{0x} and W_{0y} are equal and they are located at the same value of z we gain the symmetric fundamental mode Gaussian Beam and equation 4.4 becomes:

$$E(r,z) = \left(\frac{2}{\pi w^2}\right)^{0.5} \exp\left(\frac{-\left(x^2+y^2\right)}{w^2} - jkz - \frac{j\pi r^2}{\lambda R}\,j\phi_0\right) \quad (4.5)$$

The first part of the exponential is real and has a Gaussian variation as a function of distance in x and y from the axis of propagation. Where the real part of Equation 4.5 can be seen as a Gaussian in 2 dimensions:

$$\exp\left(\frac{-(x^2+y^2)}{w^2}\right)$$

multiplied by a constant normalisation term:

$$\left(\frac{2}{\pi w^2}\right)^{0.5}$$

For simulations presented below, the Gaussian beam is modelled by the mathematical equation,

$$I(z) = e^{\frac{-(x^2+y^2)}{w^2}} \tag{4.6}$$

where x and y are positions on a 2D grid, W is the Gaussian Beam waist and *I(z)* is the intensity of the beam at the given x and y coordinates at a certain propagation distance z.

The Rayleigh range is the axial distance from the beam waist at which the radius has increased by a factor of $\sqrt{2}$ or equivalently the distance from the beam waist at which the cross-sectional area of the beam has doubled. This parameter is a function of z, the propagation distance the beam has travelled. As the beam propagates it diffracts and spreads out without the addition of collimating optics to the system. (Ji & Dou, 2012)

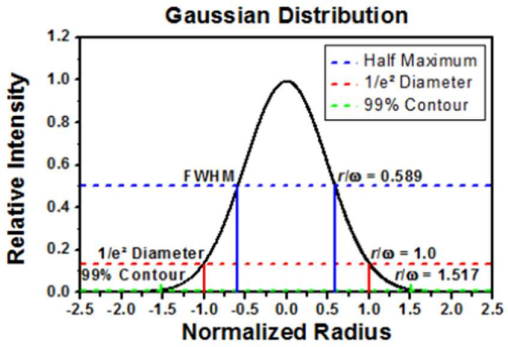

Figure 4.1 Diagram of sample Gaussian beam showing a cross section with intensity as a function of radial position. ω is the radial position at which the intensity drops to 1/e^2 the maximum value. So in the diagram above, the red line where r/ω=1 illustrates the location of the Gaussian Beam Waist radius. Diagram is from Thorlabs.com

As long as the aperture is kept sufficiently large to avoid truncation (at least 3 times the Gaussian Beam radius) then the beam will retain its Gaussian shape on transmission, however if the beam is cut off with a very small aperture then the

distribution will be no longer Gaussian and the far-field intensity distribution will develop sidelobes and other non-Gaussian features. (Burke, 2021)

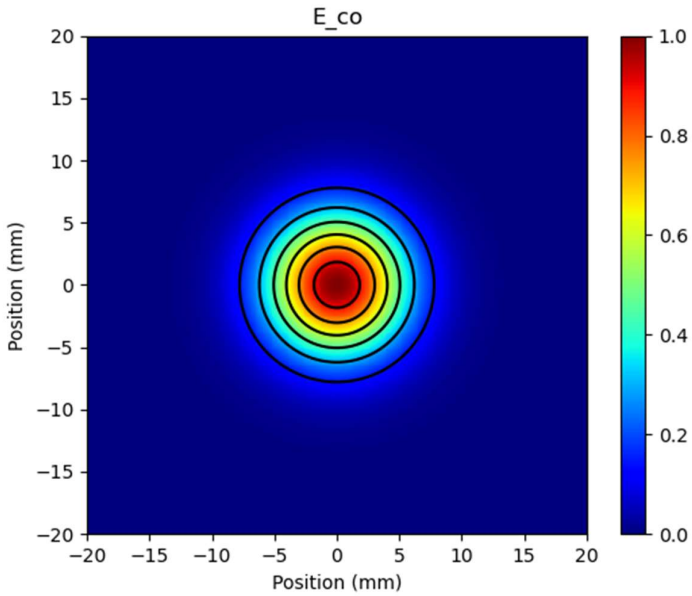

Figure 4.2 Gaussian Beam plotted in python, created from a grid file using the equation described above (Equation 4.6).

As the beam intensity can be modelled as a Gaussian beam over the XY plane with one input parameter (W, the beam radius), this means that given starting parameters of the beam, and information about the focal lengths of any mirrors and propagation distances, the shape/size of the beam can be tracked as it propagates through any optical system. The phase curvature and phase slippage relative to a plane wave must also be accounted for in a complete evolution of the beam parameters with propagation distance *z*.

The procedure used in this process is ABCD Matrix analysis. In ABCD Matrix analysis, the optical system can be modelled as a series of 2×2 matrices. In standard ABCD (or ray transfer) matrix analysis, each optical element is described by a 2×2 matrix. This matrix when operated on an incoming ray vector can be used to calculate the outgoing ray vector.

The ABCD matrix theory described in this thesis is an extension of the traditional optical ABCD ray trace matrix technique which will be used to deal with quasi-optical beams. This process can be used to track the beam

parameters for a Gaussian beam i.e. the beam radius, phase radius and phase slippage. These 3 parameters can be kept track of using ABCD matrices.

ABCD Matrices are a mathematical tool used to model relatively simple optical systems using the paraxial approximation i.e. that the angle the light rays make with a chosen reference axis are small (usually less than 1 radian). When using Gaussian beam propagation, this means that the beam waist used must be sufficiently large so that the wave front is tilted no more than~30 degrees, the required minimum beam waist for this condition to hold is approximately $\frac{2\lambda}{\pi}$. Essentially, the paraxial approximation remains valid as long as divergence angles remain well below 1 radian. This also implies that the beam radius at a beam waist must be much larger than the wavelength. (Siegman, 1990)

4.1 ABCD Matrices

Take for example, a beam with a Gaussian waist of 8 mm, wavelength of 3 mm and phase radius of 10000 mm propagating over a distance of 100 mm.

The propagation matrix is:

$$path = \begin{vmatrix} 1 & d \\ 0 & 1 \end{vmatrix}$$

where in this example *d* will be 100 mm.

So, the matrix for the path is:

$$\begin{vmatrix} 1 & 100 \\ 0 & 1 \end{vmatrix}$$

4 parameters can be found from the matrix, A, B, C and D.

$$A = path(0,0)$$

$$B = path(0,1)$$

$$C = path(1,0)$$

$$D = path(1,1)$$

where A is 1, B is 100, C is 0 and D is 1.

We then combine these values to find the beam parameter q_{out} after propagation:

$$q_{out} = \frac{A_{qin} + B}{c_{qin} + D} \tag{4.7}$$

q is related to the phase radius R and the beam width w by:

$$\frac{1}{q_{in}} = \frac{1}{R_{in}} - \frac{j\lambda}{\pi w_{in}^2} \tag{4.8}$$

From these, we can find equations for the phase radius and beam waist:

$$\frac{1}{R_{out}} = \mathrm{Re}\left(\frac{C + \frac{D}{R_{in}} - j\frac{D\lambda}{\pi w_{in}^2}}{A + \frac{B}{R_{in}} - \frac{jB\lambda}{\pi w_{in}^2}} \right) \tag{4.9}$$

$$w_{out} = \sqrt{\frac{-\lambda}{\pi\,\mathrm{Im}\left(\frac{C + \frac{D}{R_{in}} - \frac{jD\lambda}{\pi w_{in}^2}}{A + \frac{B}{R_{in}} - \frac{jB\lambda}{\pi w_{in}^2}} \right)}} \tag{4.10}$$

Where Re and Im are the real and imaginary parts of the equations. (Kehoe, 2008)

An equation for the phase slippage ϕ can also be derived:

$$\phi = -Arg\left(A + B\left(\frac{1}{R}\right) - i\left(\frac{\lambda}{\pi w^2}\right) \right) \tag{4.11}$$

Now using the values above for our sample system:

$$\frac{1}{R_{out}} = \mathrm{Re}\left(\frac{0 + \frac{1}{10000} - \frac{j(1)(3.33)}{\pi(8)^2}}{1 + \frac{1}{10000} - \frac{j(100)(3.33)}{\pi(8)^2}} \right)$$

$$\frac{1}{R_{out}} = 6.89 \times 10^{-3}$$

$$R_{out} = 145.162 \text{ mm}$$

The beam radius at the output can also be found:

$$w_{out} = \sqrt{\frac{-\lambda}{\pi \operatorname{Im}\left(\frac{C + \frac{D}{R_{in}} - \frac{jD\lambda}{\pi w_{in}^2}}{A + \frac{B}{R_{in}} - \frac{jB\lambda}{\pi w_{in}^2}} \right)}}$$

$$w_{out} = \sqrt{\frac{-3.33}{\pi \operatorname{Im}\left(\frac{0 + \frac{1}{10000} - \frac{j(1)(3.33)}{\pi 8^2}}{1 + \frac{100}{10000} - \frac{j(100)(3.33)}{\pi (8)^2}} \right)}}$$

$$w_{out} = 14.41 \text{ mm}$$

The phase slippage of the beam can be found from:

$$\phi = -Arg\left(1 + 100\left(\frac{1}{10000}\right) - \frac{3.33i}{\pi (8)^2}\right) = 0.975$$

The same mathematical process can be used to calculate beam parameters for any optical system containing mirrors or lenses for example.

The ABCD matrix representation for a lens or a mirror is the same, as when taking into account only the beam waist, phase radius and phase slippage, it does not matter whether the beam has been reflected (as is the case in a mirror) or refracted/transmitted through a lens.

The ray transfer matrix for a thin lens (or mirror) of focal length f is:

$$\begin{vmatrix} 1 & 0 \\ -\frac{1}{f} & 1 \end{vmatrix}$$

So, using the starting parameters of the beam i.e. beam waist and phase radius of curvature, and knowing the focal lengths of any mirrors, and the propagation distances between them, the above listed beam parameters can be tracked.

Take for example a beam propagating 200 mm, then refracting through a lens (ABCD matrix theory assumes on axis refraction as equivalent to a reflection off a mirror) of focal length 100 mm, then propagating another 200 mm, with a starting beam waist of 8 mm and phase radius of 10000 mm the resulting beam radius, phase radius and phase slippage can be found.

The ABCD Matrix for a 200 mm focal length mirror is:

$$\begin{vmatrix} 1 & 0 \\ -\frac{1}{200} & 1 \end{vmatrix}$$

The Matrix for propagation of 200 mm is:

$$\begin{vmatrix} 1 & 200 \\ 0 & 1 \end{vmatrix}$$

So, the resultant matrix for the path, the beam takes is the product of 3 matrices, 2 propagation and 1 reflection

$$Resultant = \begin{vmatrix} 1 & 200 \\ 0 & 1 \end{vmatrix} . \begin{vmatrix} 1 & 0 \\ \frac{-1}{200} & 1 \end{vmatrix} . \begin{vmatrix} 1 & 200 \\ 0 & 1 \end{vmatrix} = \begin{vmatrix} 0 & 200 \\ -0.005 & 0 \end{vmatrix}$$

Then the beam waist, phase radius and phase slippage can be found from equations 4.9, 4.10 and 4.11, with A now being 0, $B = 200, C = -0.005$ and $D = 0$. This gives an output beam waist of 21.2 mm, an output phase radius of -89055.8 mm and a phase slippage of 1.564.

The beam radius value found from the ABCD Matrices can be used to construct an ideal Gaussian plot using Equation 4.6 with only the x-dimension. This can then be plotted vs field cut data taken from a simulation of the same system in a commercial physical optics analysis tool, GRASP, described in chapter 5. If the predictions of the ABCD matrices matches the simulated beam in GRASP, we should expect both plots to match when plotted together.

As can be seen from figure 4.3, the plots overlap perfectly, indicating that the beam radius predicted by the ABCD Matrices matches that of the beam simulated by GRASP. This also demonstrates that the beam retains its Gaussian shape as no truncation is included, assuming that the mirror is sufficiently large to avoid truncation effects.

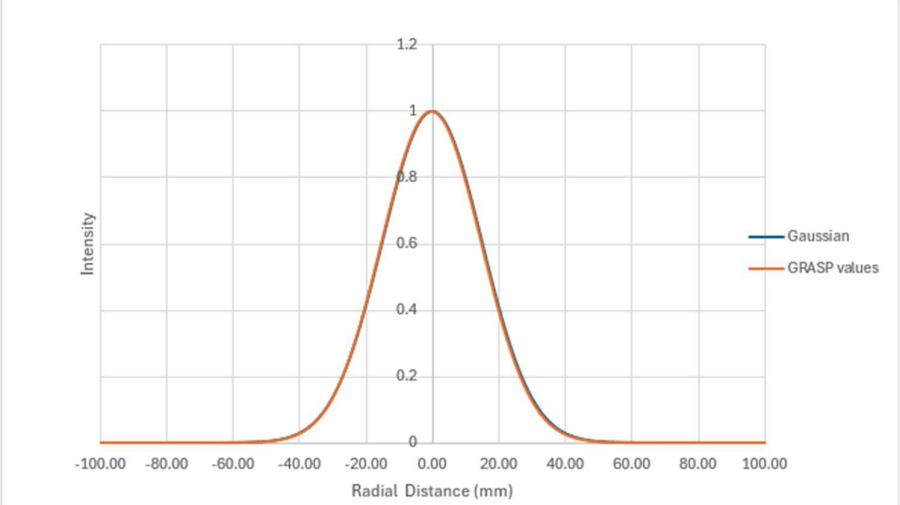

Figure 4.3 Plot of field values taken from GRASP, along with a predicted Gaussian from the ABCD Matrices.

4.2 Laguerre-Gaussian Modes

In radially symmetric optical systems, the Gaussian Beam is the lowest-order mode of a family of Laguerre-Gaussian Modes. Summation of higher complexity beam modes are needed to analyse more complex electric field shapes as will occur as a beam propagates through the optical system. The Laguerre-Gaussian modes are defined by equations of the form:

$$A = \left(\sqrt{\frac{2}{\pi w^2}}\right)^2 L_n\left(\frac{2r^2}{w^2}\right) e^{\frac{-2r^2}{w^2}} (2\pi r) \tag{4.12}$$

These can be seen as a combination of the fundamental Gaussian beam which is the $e^{-\frac{2r^2}{w^2}}$ part of the equation, and the nth Laguerre polynomial. L_n are solutions to Laguerre's differential equation (Weisstein, 1999):

$$xy''+(1-x)y'+ny=0, y=y(x) \tag{4.13}$$

The Laguerre-Gaussian modes can also be shown to be solutions to the paraxial wave equation with normalised electric field distribution (Goldsmith, 1998):

$$E_{pm}(r,\phi,z)=\frac{\left[\frac{2p}{\pi(p+m)!}\right]^{0.5}}{w(z)\left[\frac{\sqrt{2}r}{w(z)}\right]L_{pm}\left(\frac{2r^2}{w^2(z)}\right)}\exp\left[\frac{-r^2}{w^2(z)}-jkz-\frac{j\pi r^2}{\lambda R(z)}-j(2p+m+l)\phi_0(z)\right]\exp(jm\phi)$$

(4.14)

When describing systems that are axially symmetric such as corrugated feed horns these modes can be written as:

$$E_{p0}(r,z)=\left[\frac{2}{\pi w^2}\right]^{0.5}L_{p0}\left(\frac{2r^2}{w^2}\right)\exp\left(\frac{-r^2}{w^2}-jkz-\frac{j\pi r^2}{\lambda R}+j\left(2p+1\right)\phi_0\right)\quad(4.15)$$

which has the same form as Equation 4.12 used in simulations below.

Associated Laguerre Modes

For non-circularly symmetric cases where the profile of the beam has a φ dependence a family of associated Laguerre modes can be used to describe the beam profile.

The associated Laguerre modes are described using the associated Laguerre polynomials (also known as the generalised Laguerre polynomials). The associated Laguerre polynomials are solutions to Laguerre's differential equation:

$$xy''+\left(m+1-x\right)y'+ny=0,\ y=y\left(x\right)\qquad(4.16)$$

The circularly symmetric case above can be seen as a solution with m=0.

A solution can be found to the paraxial wave equation in cylindrical coordinates with a degree n, and order m which has a normalised electric field given by:

$$E_{mn}\left(r,\phi,z\right)=\left[\frac{2n!}{\pi\left(p+m\right)!}\right]^{0.5}\frac{1}{w\left(z\right)}\left[\frac{\sqrt{2}r}{w(z)}\right]^{m}L_{mn}\left(\frac{2r^2}{w^2(z)}\right)\exp\left[\frac{-r^2}{w^2(z)}-jkz-\frac{j\pi r^2}{\lambda R(z)}-j(2n+m+1)\phi_0(z)\right]$$

(4.17)

(Goldsmith, 1998)

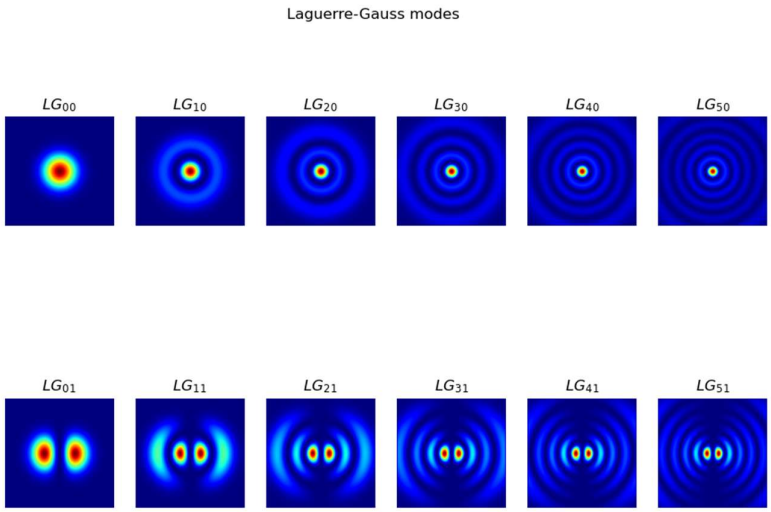

Figure 4.4 The above image shows Laguerre-Gaussian Modes generated using the LightPipes python package. The top row shows the circularly symmetric modes with m=0. The second row shows the associated Laguerre-Gaussian modes which have angular variation. The axial lengths just scale in terms of the beam radius W.

4.3 Hermite-Gaussian Modes

In optical systems where circular symmetry does not exist such as pyramidal feed horns and square mirrors/reflectors it is useful to describe the profile of the beam using Cartesian Hermite-Gaussian Modes.

The Hermite-Gaussian modes are defined by equations of the form:

$$A = H_n\left(\frac{\sqrt{2}x}{w(z)}\right)\exp\left[-\frac{jkx^2}{2q(z)}\right] \tag{4.18}$$

where we take the beam radius w and the complex beam parameter q to be the same as above.

H_n refers to the nth Hermite polynomial. The function H is a solution to Hermite's differential equation:

$$\frac{d^2H(u)}{du^2} - 2u\frac{dH(u)}{du} + 2mH(u) = 0 \tag{4.19}$$

When describing systems with rectangular symmetry it is useful to describe the beam in 2 dimensional rectangular coordinates. The 2-dimensional Gauss-Hermite beam mode is described by the equation:

$$E_{mn}(x,y) = \left(\frac{1}{\pi w_x w_y 2^{m+n-1} m!n!}\right)^{0.5} H_m\left(\frac{\sqrt{2}x}{w_x}\right) H_n\left(\frac{\sqrt{2}y}{w_y}\right) \exp\left(-\frac{x^2}{w_x^2} - \frac{y^2}{w_y^2}\right)$$

(4.20)

Where H_m and H_n are the m^{th} and n^{th} Hermite polynomials, w_x and w_y refer to the Gaussian beam waist in the x and y directions. In the examples used in this thesis the Gaussian beam waists in the x and y directions are the same so Equation 4.20 becomes:

$$E_{mn}(x,y) = \left(\frac{1}{\pi w 2^{m+n-1} m!n!}\right)^{0.5} H_m\left(\frac{\sqrt{2}x}{w}\right) H_n\left(\frac{\sqrt{2}y}{w}\right) \exp\left(-\frac{x^2}{w^2} - \frac{y^2}{w^2}\right) \tag{4.21}$$

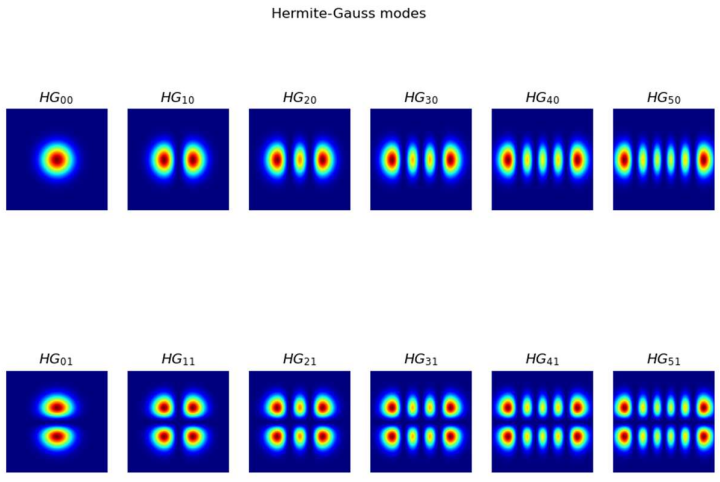

Figure 4.5 Hermite-Gaussian Modes generated by the LightPipes python package to illustrate the modal profile complexity with increasing mode order/number.

5 Chapter 5: Truncation Analysis Theory

Electromagnetic fields from horn antennae are Gaussian-like so the Gaussian beam shape can be used as a good approximation for diffraction of the beam as it propagates through an optical system.

In this idealised case, assuming sufficiently sized mirrors relative to the Gaussian beam waist, a Gaussian beam propagating through the system will retain its Gaussian profile through the system, only changing in width, Phase slippage, and radius of curvature. However, in a finite diameter system, some beam loss may occur due to truncation of the beam relative to the finite size of the optical components, this will lead to loss and the profile of the beam changing from a simple Gaussian shape and with less power.

In this truncation analysis study, we propagate an electric field from a horn aperture which is represented as Gaussian modeled using free space Laguerre-Gaussian modes to construct the electric field shape, which can more accurately reflect the development of the beam profile as it propagates through the BISOU optical system. The mode coefficients, indicating the power contained in each mode, are calculated from the integral in equation 5.1.

$$A_n = \int_0^r \sqrt{\frac{2}{\pi w^2}}^2 L_n\left(\frac{2r^2}{w^2}\right) e^{-\frac{2r^2}{w^2}} \tag{5.1}$$

The wavefunction describing the beam at the mirror is defined by the equation:

$$\psi_{mn} = \sqrt{\frac{2}{\pi w^2}} L_i\left(\frac{2r^2}{w^2}\right) \exp\left(\frac{-r^2}{w^2}\right) \exp\left(\frac{-ikr^2}{2R}\right) \tag{5.2}$$

where w refers to the beam radius at the mirror, r is the radial distance from the centre of the beam, k is the wavenumber, and R is the radius of curvature of the beam at that point. The zero-order mode has the 0^{th} Laguerre Polynomial, which is just:

$$L_0 = 1$$

This only leaves the Gaussian part of the equation multiplied by a constant, giving the fundamental Gaussian beam where the zeroth mode coefficient will

evaluate to 1 indicating that all the power is contained in the fundamental Gaussian beam mode. The mode coefficient calculated from the integral in equation 5.3 will evaluate to 1.

$$A_0 = \int \left(\sqrt{\frac{2}{\pi w^2}} \right)^2 e^{-\frac{2r^2}{w^2}} \tag{5.3}$$

As the beam travels through the system and is reflected from the mirrors and some power might be lost from the mirror's finite sized surfaces, the power contained in each of the modes changes, so more power is scattered to the higher order modes. When summed a more complex electric field shape than the initial Gaussian Beam will be realised. The power contained in each of the modes after truncation is found from the scattering matrix which is calculated from the integral of:

$$S_{mn} = \int_0^r \frac{2}{\pi w^2} L_m\left(\frac{2r^2}{w^2}\right) L_n\left(\frac{2r^2}{w^2}\right) e^{\left(-\frac{2r^2}{w^2}\right)} 2\pi r \tag{5.4}$$

The scattering matrix is an $m \times n$ matrix, where each element gives a fraction of the power contained in a modal order required to reconstruct the truncated electric field. It is assumed that the radius of the mirror is a distinct boundary beyond which no power will be reflected i.e.

$$at\ radii \leq mirror\ radius : 100\%\ of\ power\ reflected$$
$$at\ radii > mirror\ radius : 100\%\ of\ power\ lost.$$

This means that if the beam at any point of propagation through the system has a radius larger than a rim representing the circular edge of the mirror or lens., some power will be lost from the incident beam. The scattering matrix is then multiplied with the input mode coefficient matrix A_n to give B_n the output mode coefficients.

$$B_n = S_{mn}.A_n \tag{5.5}$$

Initially, 100% of the power will be contained in the 0-order mode, i.e. the fundamental Gaussian mode. However, as the beam propagates through the optics, the power is scattered between the different modes, causing the beam profile to become more complex.

For example, if we have a 10 mm waist Laguerre-Gaussian 0^{th} order beam at 90GHz propagating 20 mm and hitting a 70 mm radius mirror, the first 5 input mode coefficients A_n are:

$$\begin{pmatrix} 1 \\ 0 \\ 0 \\ 0 \\ 0 \\ \dots \end{pmatrix}$$

The scattering matrix with no truncation is an identity matrix: When the modes are propagated to the first optical component before truncation and including phase slippage, the modes still contain unity power but the coefficients are now complex due to the phase slippage from the waist position

$$\begin{pmatrix} (0.9833 + 0.182j) \\ (-3.99e-17 - 1.885e-17j) \\ (6.368e-18 - 9.292e-18j) \\ (3.627e-17 + 4.694e-17j) \\ (-1.604e-17 + 4.267e-17j) \\ \dots \end{pmatrix}$$

As no truncation has occurred yet, the power contained in the first mode is found from $abs\left(0.9833+0.182j\right)^2=1$. This indicates that 100% of the power is still contained within the first beam mode, the fundamental Gaussian mode and all other modes are effectively zero. For demonstration, if the same system with a smaller 10 mm mirror radius is used and is truncating the beam more severely, the first 6 elements from the scattering matrix becomes:

0.853	0.282	0.0122	-0.086	-0.094	-0.063	-0.022	…
0.282	0.312	0.259	0.176	0.093	0.026	-0.0207	…
0.0121	0.259	0.311	0.266	0.184	0.099	0.028	…
-0.086	0.176	0.266	0.2615	0.212	0.148	0.086	…
-0.094	0.093	0.184	0.212	0.202	0.172	0.134	…
…	…	…	…	…	…	…	…

This imposed a new power distribution into the output mode coefficients from this operation and the first 5 output mode coefficients are now:

$$\begin{pmatrix} (0.83828 + 0.155j) \\ (0.27759 + 0.051j) \\ (0.01195 + 0.0022j) \\ (-0.08422 - 0.0156j) \\ (-0.09201 - 0.017j) \\ \dots \end{pmatrix}$$

This shows that the zero-order fundamental mode now contains $abs(0.8383 + 0.155j)^2 = 0.702 = 70.2\%$ of the power, with almost 8% in the second order mode, and 0.014% in the 3rd mode. The plot of the beam shape shows the change from the fundamental Gaussian beam to a more complex shape with 70 Laguerre-Gaussian modes used:

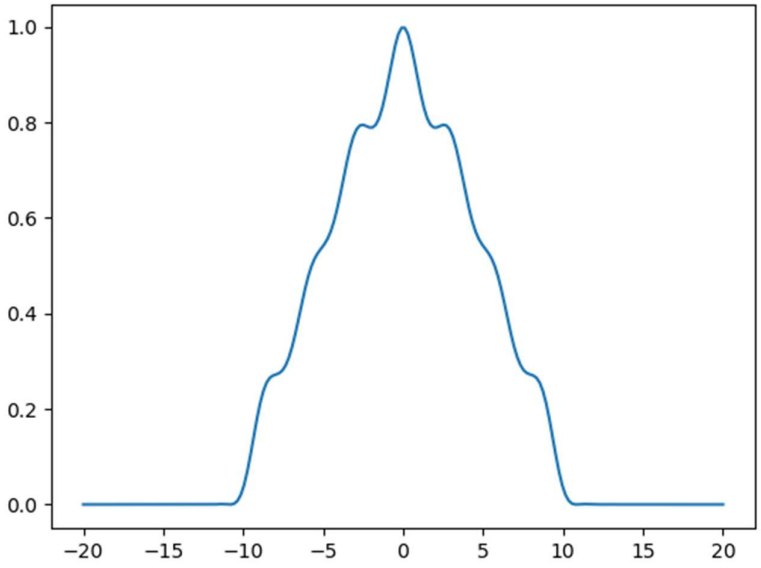

Figure 5.1 Truncated Beam from a 10 mm mirror.

These more complex beam shapes have distributions that may diffract more and have more off-axis power where the electric field does not taper off exponentially.

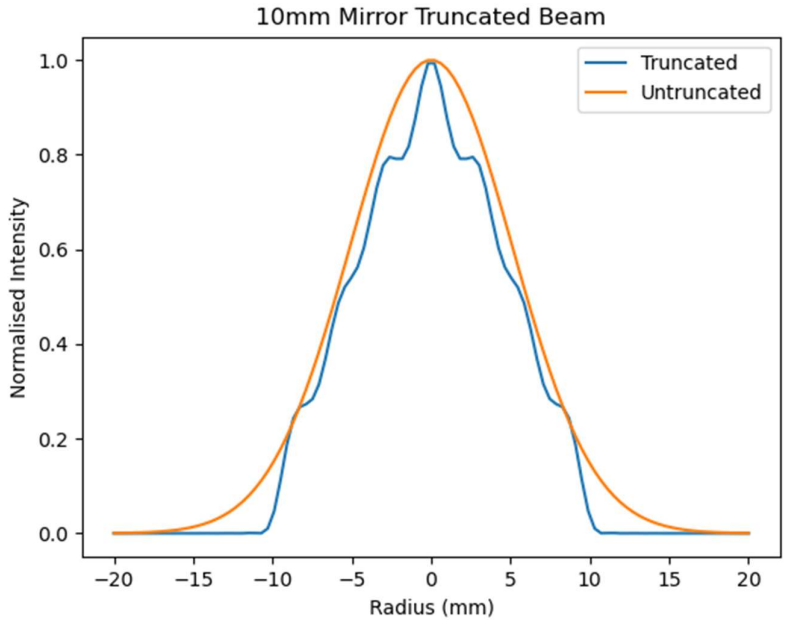

Figure 5.2 plot of the same truncated beam from figure 5.1 overlapped with an untruncated beam. The untruncated beam retains the initial Gaussian profile, the truncated beam becomes distorted, and has an intensity profile which no longer drops off exponentially.

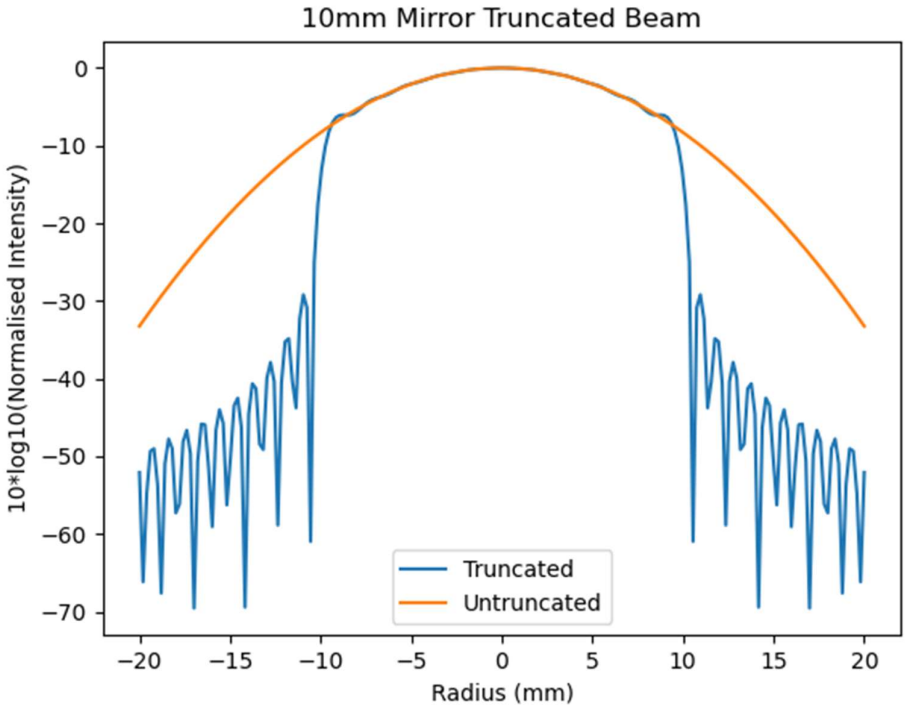

Figure 5.3 log plots of both the truncated beam (blue) and the untruncted gaussian beam (orange). The sharp truncation of the beam profile of the blue beam is clear.

As can be seen, the power distribution in the higher order beam is wider and so if the next mirror were to be 5 mm radius, the power loss would be higher for the higher order components of the beam than the fundamental mode Gaussian. This shows that truncation will more severely affect the higher order beam modes than the fundamental beam mode. These simulations will need to be carried out for the entire system to ensure the majority of the beam modes are still transmitted through the system. The output mode coefficients for the beam are dependent on the input truncated beam from the previous element and the scattering matrix for the mirror. This means that for an optical system with multiple mirrors the evolution of the beam will be much more complex than the simple single mirror system described above.

5.1 Laguerre-Gaussian Mode Truncation Results

Truncation analysis was carried out initially using a summation of Gaussian Beam Modes summed correctly to reconstruct the evolution of an electric field pattern as a function of propagation distance z. The electric field to be traced was set to be a Gaussian Beam with radii of 10, 12 and 15 mm at a frequency of 90 GHz, propagated through the BISOU system described in section 6.1 using both the GBM truncation developed and the commercial package GRASP using physical optics, described further in chapter 5. Spillover power values are recorded at each mirror truncation. The nominal initial value for the FTS mirrors is 45 mm however it is important to check performance of the beam at a smaller mirror size and a larger mirror size in case any modification of the system is required.

These 3 values for beam waist were simulated for varying FTS mirror radii, from 35 to 50 mm where the nominal radius is 45 mm. The range of values of beam size and mirror size were used to determine the range of acceptable values for the final system. These values were compared with values calculated with GBMA code developed in Python using the method described previously, where the spillover values were taken as the sum of the absolute value squared of the mode coefficients for each section of the beam path.

The beam was simulated using 150 modes and 200 data points to plot the resultant beams, this was chosen as a compromise between increased accuracy

and computation time. Up to a certain point a higher number of modes leads to a more accurate representation of the beam profile but beyond a certain mode number value it significantly increases computation time without a reciprocating corresponding increase in accuracy This was established in developing the code and ensuring reproducible results with various mode numbers.

Simulations were performed for a range of initial Gaussian beam radii and a range of mirror sizes for the BISOU FTS column for the BISOU breadboard system described in section 2.1. This range of values was tested to find the best compromise between initial beam size, and mirror size throughout the optical path. A smaller initial beam size will diverge at a faster rate than a larger initial beam size up to the first mirror as it propagates through the system

Results were obtained for a range of initial beam sizes (10, 12 and 15 mm) at 90GHz and a range of mirror sizes (35,40,45, and 50 mm). For the default BISOU FTS mirror size of 45mm the RPHS (Relative Power Hitting Scatterer) values, which are a measure of transmitted power which hits each mirror with the initial value normalised to 1. Values are shown in the table below obtained from PO simulations performed in GRASP, where M5 to M1 are the mirror pairs in the FTS column starting from the bottom. The initial size of the secondary mirror was 45 mm radius and the initial value for the primary mirror was 100 mm radius. In initial designs for the BISOU breadboard it was desirable to have a smaller telescope overall.

Initial beam size (mm)	M5	M4	M3	M2	M1	Secondary	Primary
10	1.000	0.9999	0.9997	0.9997	0.9996	0.9355	0.8725
12	1.000	0.9993	0.9974	0.9968	0.9965	0.8780	0.7865
15	1.000	0.9907	0.9818	0.9773	0.9757	0.7680	0.6479

Table 5.1 Table of truncation values for a sample BISOU system with M5 to M1 set to 45 mm radius, for an initial Gaussian beam waist of 10,12 and 15 mm simulated using GRASP

Up until the secondary mirror the truncation level for each of the three beam sizes is comparable, however truncation for the two larger beam sizes is significantly worse at the secondary and primary mirrors. Table 5.2 below

shows RPHS values obtained from the python truncation code described previously:

Initial beam size (mm)	M5	M4	M3	M2	M1	Secondary	Primary
10	1.0000	0.9999	0.9999	0.9999	0.9999	0.9323	0.8662
12	1.0000	0.9993	0.9991	0.9982	0.9978	0.8587	0.7725
15	1.0000	0.9907	0.9885	0.9735	0.9713	0.7061	0.6103

Table 5.2 Truncation values for the sample BISOU system with 45mm FTS mirrors and varying beam sizes 10,12 and 15 mm.

This was done with the aim of finding the best fundamental mode beam size to match the optical design with 45 mm radius FTS mirrors. Results from GRASP in Table 5.1 were compared with results from the Python truncation code in Table 5.2.

Table 5.3 below shows truncation values from Python and GRASP for an FTS mirror radius of 35 mm and an initial beam waist of 15 mm at 90GHz. Although both methods exhibited good agreement up to this point, a greater discrepancy between the python simulation and GRASP is observed in figure 5.3 below.

	M5	M4	M3	M2	M1	Secondary	Primary
GRASP	0.9996	0.9347	0.9174	0.8999	0.8915	0.6668	0.5912
Python	0.9995	0.9404	0.9238	0.8579	0.8458	0.5850	0.4903

Table 5.3 Truncation values for a 3 5mm FTS mirror radius, with a 15mm Gaussian beam.

Sources of discrepancy between the Python calculations and the truncation analysis code could be because the truncation analysis code does not take into account the angle of incidence of the beam on the mirror, it is assumed that the beam is hitting the mirror directly, and in the centre. The mirror definitions in GRASP described in section 3.1 define a rim relative to the z axis of the reflector which is at an angle relative to the incident beam, whereas described previously the Gaussian Beam mode analysis assumes normal illumination of the mirror.

Physical optics assumes that induced surface currents go to zero in any non-directly illuminated "shadow" regions with a rim defining the surface at some angle, the truncation analysis code described above assumes normal illumination of the mirror. It was discovered that the original design, starting with an input beam of a 10 mm waist Gaussian at 90 GHz, led to a beam waist of 29 mm occurring at the secondary mirror of the breadboard system, and a beam waist of 92 mm at the primary mirror. This led to quite a large amount of beam loss at these two mirrors:

Mirror	M5	M4	M3	M2	M1	Secondary	Primary
Python	1.0000	0.9999	0.9999	0.9999	0.9999	0.9323	0.8662
GRASP	1.0000	0.9998	0.9997	0.9997	0.9996	0.9355	0.8725

Table 5.4 Truncation Values for a 10 mm initial 90GHz *Gaussian Beam with 45 mm FTS mirrors*

As can be seen from Table 5.4 For the 10 mm Gaussian, 45 mm FTS there was a power loss of roughly 6% of the beam at the secondary mirror and a further 6% loss at the primary mirror, meaning a total loss of over 10% of the beam at these two mirrors alone.

Further simulations showed that a secondary mirror of 65 mm was an acceptable compromise of beam loss vs mirror diameter.

M1 RPHS Python	M1 RPHS GRASP	Secondary RPHS Python	Secondary RPHS GRASP	Primary RPHS Python	Primary RPHS GRASP
0.99993	0.9996	0.9998	0.9971	0.9007	0.8760

Table 5.5 Truncation results with 65 mm secondary, 10 mm 90GHz starting Gaussian.

As can be seen from the above table when simulating a 10 mm waist 90GHz starting Gaussian Beam a 65 mm secondary now results in only 1% beam loss at the secondary, however there is still roughly 10% beam loss at the primary. The beam waist at the primary is 92 mm with this configuration, for a mirror of radius 100 mm, this beam is too large.

The primary mirror in the initial versions of this design had a set radius of 100 mm due to the overall constraints of the system. The above truncation results indicate that this mirror size is much too small for the current beam, this means that the mirrors earlier in the optical path would need to be modified to reduce

the resulting beam size at the end as the primary mirror cannot be made any larger.

To solve this issue, the focal length of the secondary mirror was increased by 40 mm, this caused the beam to focus at a point closer to the primary intercept, meaning less divergence of the beam would occur between this point, and the intercept with the primary mirror.

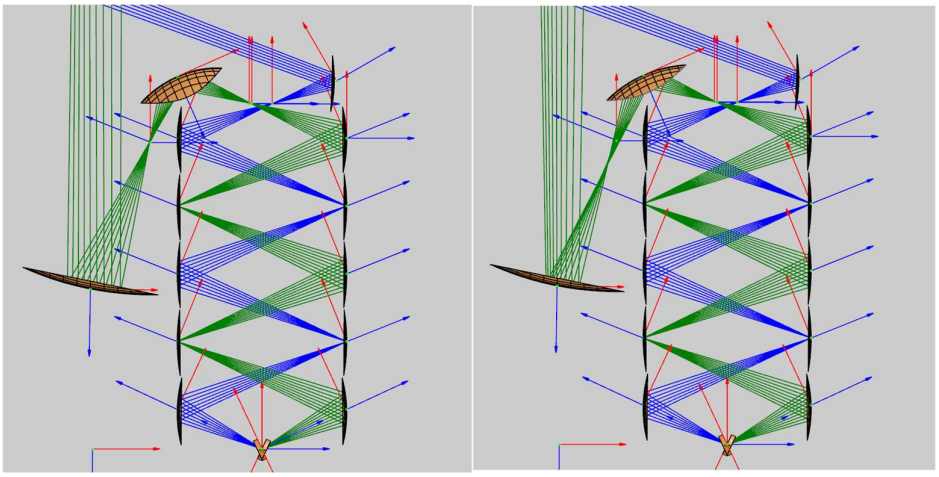

Figure 5.4 The original Breadboard layout (left) and the updated design with longer focal length Secondary mirror (right)

This change resulted in the beam waist at the primary becoming 67 mm, leading to a beam loss of less than 2% for the total system, compared to ≈13% for the original design

M1RPHS Python	RPHS GRASP	Secondary RPHS Python	RPHS GRASP	Primary RPHS Python	RPHS GRASP
0.9999	0.9996	0.9998	0.9975	0.9885	0.9810

Table 5.6 Truncation values from GRASP and Python for the last 3 mirrors in the system. Longer focal length secondary

These modifications of the initial design clearly demonstrate the benefits of carrying out truncation analysis of an optical design before moving onto more detailed physical optics simulations of resulting beams, as it can quickly indicate any problems with the design with regard to mirror sizes and focal lengths.

Truncation Analysis was also performed with a top-hat beam. The tophat beam is effectively a circular radius within which the field is 1, and outside this radius the field is zero, giving the field a flat peak in the middle with steep edges, this beam takes the form:

$$f(x) = \begin{cases} 1 & -r \leq x \leq r \\ 0 & \text{otherwise} \end{cases}$$

The truncation analysis is carried out using the same process as for a Gaussian beam except the initial mode coefficients are this time calculated using the integral:

$$\int_0^a \sqrt{\frac{2}{\pi w^2}} \sqrt{\frac{1}{\pi a^2}} L_n\left(\frac{2r^2}{w^2}\right) \exp\left(\frac{-r^2}{w^2}\right) 2\pi r \tag{5.6}$$

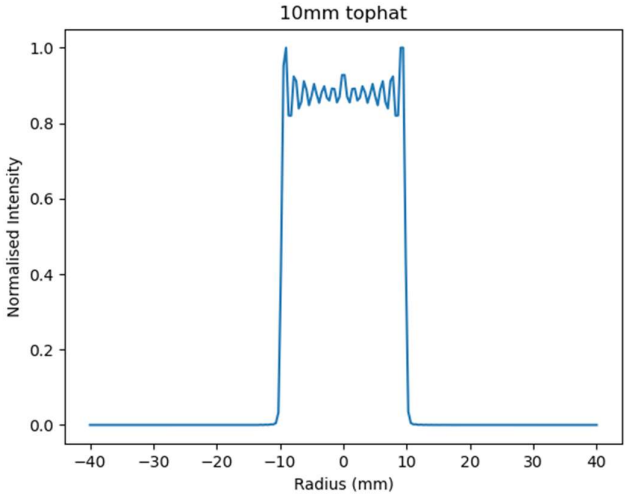

Figure 5.5 Tophat beam plot from Python, this is the result of the overlap integral of mode coefficients above in equation 5.5 multiplied by the wavefunction

A tophat function is input into GRASP as a grid of values, GRASP then reads this grid as an electric field.

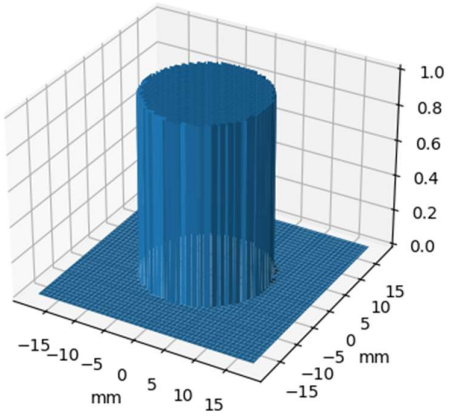

Figure 5.6 Tophat beam generated from grid of values where the intensity of the beam is 1 within the specified radius and zero everywhere else.

The above grid is run through grasp and a physical optics simulation performed; these results are compared to Truncation Analysis using the Python code described above. In theory these results should be very similar, and the Python calculations simply serve as a way of verifying the results from the physical optics simulations performed by GRASP.

In practice there was a larger discrepancy between the GRASP results and the Python results for the tophat beam. It is believed this is due to the significantly higher off-axis power in the tophat beam compared to the Gaussian beam which has power that drops off exponentially. The difference in treatment of the edges/rims of the reflectors between GRASP and GBMA may lead to some discrepancies between the results. Whereas GBMA assumes normal illumination, GRASP actually models reflections with a defined rim. This discrepancy in truncation levels is likely to be more prominent for a beam with a higher off-axis intensity profile such as a tophat field.

Below is a sample of some of the results obtained from GRASP and Python of the tophat field through the system. A 10 mm tophat at 90 GHz was propagated through GRASP as an example and the nominal value of 45 mm was used for the FTS mirrors:

	M5	M4	M3	M2	M1	Secondary	Primary
GRASP	0.915599	0.912344	0.908005	0.906104	0.904187	0.897121	0.888922
Python	0.910839	0.910839	0.880148	0.88013	0.86755	0.86382	0.850704

Table 5.7 Truncation results for a 10mm 90GHz tophat field with a nominal value of 45mm for the FTS column

This discrepancy between GRASP and Python results was mostly expected as the tophat field was used as an extreme example in contrast to the Gaussian Beam. The tophat field has significantly higher off axis power whereas the power in the Gaussian beam profile drops off exponentially from $r = 0$, the centre of the mirror. In reality, the spillover of the multimoded horn antenna will be somewhere in between these two simulated examples. As a result of this truncation analysis study an idea of the expected range of beam loss can be obtained, both a basic from the Gaussian Beam, and a higher truncation case of the tophat field. As demonstrated above, these studies can help inform the design process of the BISOU optics and highlight any issues with the initial design.

A further check on the validity of plotting beams from imported grid files can be found by plotting a Gaussian beam generated within GRASP, and a Gaussian beam generated with GBMA. The beam file from GBMA is generated in a similar way to the tophat beam described above. The input file for a Gaussian of radius w, is a grid of x and y values where the intensity at a point (x,y) is given by:

$$I = \exp\left(\frac{-\left(x^2 + y^2\right)}{w^2}\right) \tag{5.7}$$

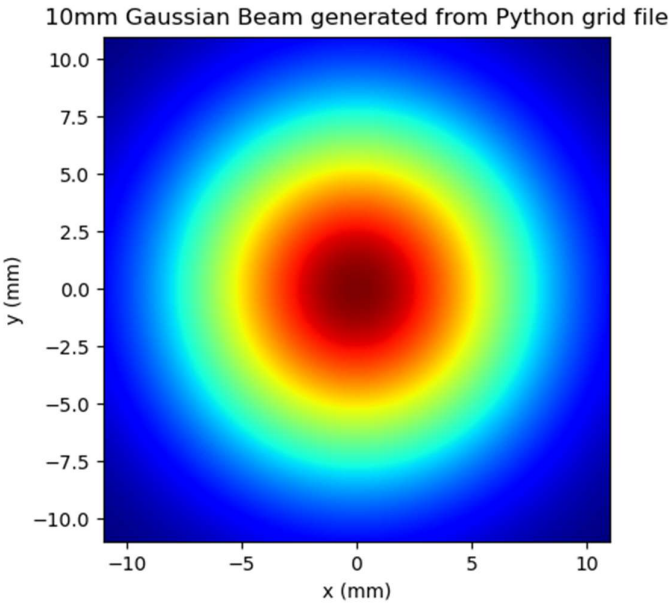

Figure 5.7 Gaussian beam generated from a grid file in python using equation 5.7

As with the tophat beam, these grid files can be imported into GRASP and used as a source field. Figure 5.8 below shows the above Gaussian beam, and a Gaussian beam generated in GRASP after propagating 100 mm.

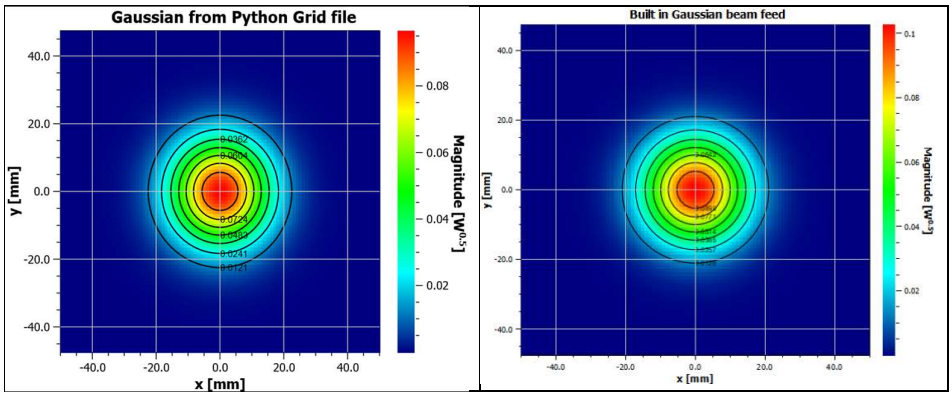

Figure 5.8 Plot of a Gaussian imported from the grid file in figure 5.7, and a Gaussian beam from the built in GRASP description. Both are plotted after propagating 100 mm, so the beam waist in these plots is now 14.575 mm

As can be seen in figure 5.8, both beam plots are extremely similar. This indicates that a beam imported from an externally generated grid file and a beam generated using the built in GRASP Gaussian beam definition should be equivalent.

To ensure consistency a further test was performed comparing the truncation of this externally generated grid file with the beam from GRASP. If both perform equivalently, then the truncation values should be extremely similar/identical. A 10 mm beam defined in both ways was propagated 190 mm and reflected off a 45 mm radius mirror.

	RPHS (GRASP)	RPHS (Python)
GRASP defined Gaussian	0.970516	0.99180
Gaussian from grid file	0.969591	0.99180

Table 5.8 Truncation values from both GRASP and Python, for a 10mm Gaussian beam generated from GRASP using the defined Gaussian beam function, and a Gaussian beam generated from Python code.

This shows extremely good agreement between the Gaussian imported from a grid file and also GRASPs built in Gaussian definition when both are propagated in GRASP. GRASPs spillover values agree to within 0.02%. Both spillover values also agree well with the truncation analysis python code to within 2%

5.2 Hermite-Gaussian truncation analysis

While the Laguerre-Gaussian truncation analysis method most efficient in cases where circular symmetry of the beam exists (as in the case of conical horns), A different description of the beam modes is optimum for cases with Cartesian symmetry (in the case of pyramidal horns). The Laguerre Polynomials described previously have natural circular symmetry, Hermite polynomials are necessary in the rectangularly symmetric case.

The process for performing the truncation analysis is the same as described in section 5.1 with circular symmetry, the only modification is a change in the overlap integrals used for the initial description of the beam and for the scattering matrix. When the Laguerre-Gaussian case was assumed to have perfect circular symmetry, an integral in $2\pi r\, dr$, with angular symmetry was sufficient to carry out the scattering integral. For Cartesian geometries representation Hermite modes are the natural mode set to utilise. The Hermite modes are written in a way to avoid double indexing and can be written as

$$\Psi_n(x,y) = h_n(\frac{2(x^2+y^2)}{W^2})\ \exp[-jk\left(z+\frac{x^2+y^2}{2R}\right)]\exp[j(\frac{Int(n)}{\sqrt{n}}+\frac{Mod(n)}{\sqrt{n}}+1)\varphi_n]$$

(5.8)

where h_n is a Hermite polynomial of order number n, *Int(n)* returns numerically the integer part of n relative to the square root of the total number of modes and *Mod(n)* is the modulus of i relative to the square root of the total number of modes. Modulus is a function that can be given in certain algebraic functions to specify that integers should be treated modulo n. This formulation as fully described in Tim Finns thesis in 2007 (Finn, 2007) is adopted to avoid double indexed Hermite modes. In order to understand why this can lead to an unwanted level of complexity we return to the original description of Hermite modes in chapter 4 given by (Martin & Bowen, 1993)

$$\Psi_{mn}(x,y) = h_m(\frac{2(x^2)}{W^2})h_n(\frac{2(y^2)}{W^2})\exp[-jk\left(z+\frac{x^2+y^2}{2R}\right)]\exp[j(m+n+1)\phi_{mn}] \quad (5.9)$$

The table illustrates the equivalence of $Int(n)$ and $Mod\ (n)$ to the normal indexing parameter i the double indexed and single indexed modes for 100 Hermite modes (including only the first 20 modes). It is necessary to use a number of modes that has a whole number square root (25, 49, 100, 400 etc) or the indexing goes out of sequence.

I	Int(n)	Mod(n)	i	Int(n)	Mod(n)
0	0	0	10	1	0
1	0	1	11	1	1
2	0	2	12	1	2
3	0	3	13	1	3
4	0	4	14	1	4
5	0	5	15	1	5
6	0	6	16	1	6
7	0	7	17	1	7
8	0	8	18	1	8
9	0	9	19	1	9

The real advantage of single indexed Hermites stems from its ease of use in simple matrices. The standard double indexed Hermite require an overlap integral of the general form

$$\int \left(\Psi_{mn} \Psi_{op}^{*}\right) dxdy \,, \tag{5.10}$$

where Ψ_{mn} and Ψ_{op} represent the overlapping fields (e.g for a truncation Ψ_{mn} would represent fields at one side of the aperture Ψ_{op} would represent the field at the output side of the aperture). The general form of the single indexed Hermite overlap integral is

$$\int \left(\Psi_{m} \Psi_{n}^{*}\right) dxdy \,, \tag{5.11}$$

where Ψ_m and Ψ_n again represent the overlapping fields. Now we have only two indices and we end up with a standard 2D matrix $m \times n$ regardless of the number of modes we choose to use.

Once the indexing of the Hermite modes is kept consistent as above, the truncation analysis process is the same as for the Laguerre-Gaussian beams. A sample of the scattering matrix for a beam truncated at 1.5 times its beam waist is shown below for 25 modes. It can be seen that the values start repeating after the 5th ($\sqrt{n}$) mode:

0.9946	0	0	0	0	0	0	0	0
0	0.9681	0	0	0	0	0	0	0
0	0	0.8620	0	0	0	0	0	0
0	0	0	0.6499	0	0	0	0	0
0	0	0	0	0.4509	0	0	0	0
0	0	0	0	0	0.9680	0	0	0
0	0	0	0	0	0	0.9423	0	0
0	0	0	0	0	0	0	0.8390	0
0	0	0	0	0	0	0	0	0.6325

Using the relationship from equation 5.5:

$$B_n = S_{mn} \cdot A_n$$

The output mode coefficients for this beam can be found. The first 4 mode coefficients are given below:

$$\begin{pmatrix} (0.6305 + 0.7692j) \\ 0 \\ (-2.2390e-05 - 2.7318e-05j) \\ 0 \\ (-3.6857e-05 - 4.497e-05j) \\ 0 \\ (3.1200e-16 - 9.7564e-17j) \\ \dots \end{pmatrix}$$

As before the proportion of the power contained in each mode is found from the absolute value of the mode coefficient squared. So, in this example there is still 98.9% of the power remaining in the first order mode.

Both truncation methods were applied to an example BISOU system. In this case the BISOU breadboard design was tested. This breadboard system will be constructed first and used as a testbed for the final BISOU instrument. Further analysis and simulation of this breadboard system is in section 6.7 of this thesis.

The layout in GRASP is shown in figure 5.10 below:

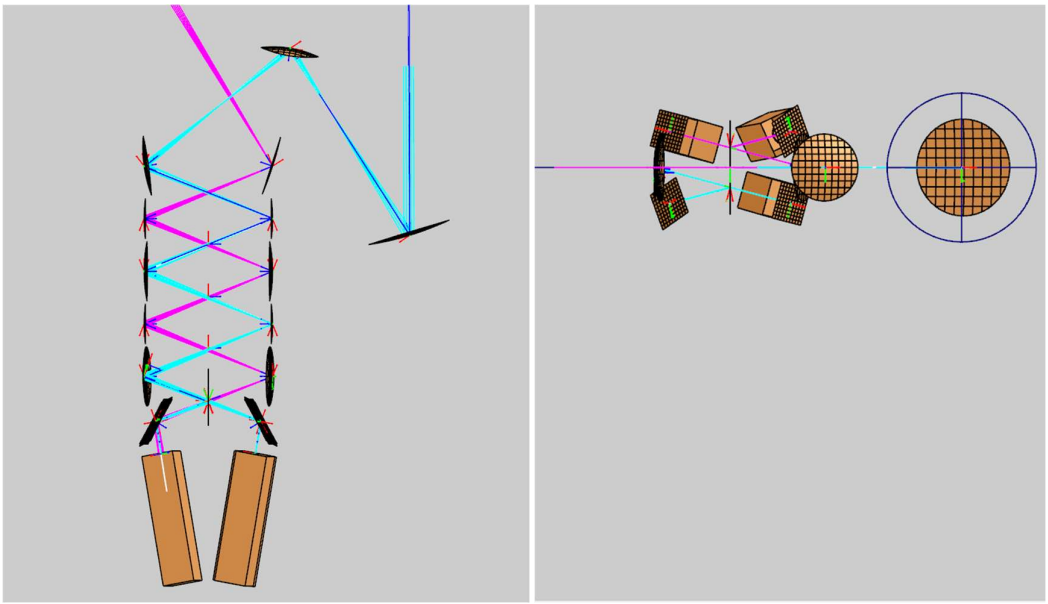

Figure 5.9 Front view and side view of the tested BISOU breadboard design. The location of the horns is represented by the rectangular boxes at the bottom. Two horns are in front of (or above) the FTS column, and two behind. This was due to space constraints horizontally within the design. Design created by Morgane Locquet le Gall.

This design was tested with the original Laguerre-Gaussian mode set, the Hermite-Gaussian mode set and a Gaussian beam propagated using GRASP using Physical Optics.

As the Laguerre-Gaussian simulation has circular symmetry, circular mirrors were assumed for the whole system. The Hermite-Gaussian simulation has rectangular symmetry, so square mirrors were assumed. Similar values would be expected for all three simulations as beam sizes were kept constant throughout and mirror diameters are consistent (only changing in geometry from circular to square in the case of the Hermite-Gaussian analysis).

Previous values for the primary mirror of 100 mm radius indicated the initial size of the mirror was too small as 20% beam loss was outside the accepted range. If this mirror radius is increased to 150 mm from the initial value the truncation levels improve greatly with over 95% of the beam power now propagating through. The radius of the primary mirror has been increased to 150 mm from the initial 100 mm value described in section 5.1

	M5	M4	M3	M2	M1	Secondary	Primary
GRASP (circular mirrors)	0.9939	0.9919	0.9888	0.9872	0.9824	0.9775	0.9694
GRASP (Square Mirrors)	0.9956	0.9943	0.9927	0.9918	0.9901	0.9863	0.9820
Laguerre modes	0.9932	0.9932	0.9815	0.9815	0.9631	0.9594	0. 0.9563
Hermite modes	0.9941	0.9941	0.9881	0.9881	0.9823	0.98209	0.9819

Table 5.9 Truncation values for an example BISOU breadboard system obtained from GRASP, Laguerre Gaussian, and Hermite Gaussian truncation analysis

The results in Table 5.8 indicate good agreement between the three methods of truncation analysis. The Laguerre-Gaussian truncation analysis agrees with the circular mirror simulation in GRASP to within 1%. The Hermite-Gaussian truncation analysis also has very good agreement with the simulation of square mirrors performed in GRASP. It is noted that the square mirrors have a slightly larger surface area so have a slightly lower truncation level compared to the circular case.

The same process was carried out for the most recent V1 version of the flight version of the BISOU instrument. There is good agreement between the Laguerre-Gaussian truncation analysis and the circular mirror simulation in GRASP. There was also good agreement between the Hermite-Gaussian truncation analysis and the square mirror simulation in GRASP.

	M5	M4	M3	M2	M1	Secondary	Primary
GRASP (circular mirrors)	0.9926	0.9915	0.9893	0.9886	0.9877	0.97916	0.9162
Laguerre	0.9932	0.9925	0.9812	0.9800	0.9660	0.9613	0.9549
Hermite	0.9941	0.9941	0.9882	0.9882	0.9823	0.9821	0.9782
GRASP (square mirrors)	0.9960	0.9955	0.9939	0.9935	0.9785	0.9461	0.9345

Table 5.10 Truncation values for the BISOU V1 instrument. Values are included for GRASP Gaussian beam simulations using circular and square mirrors, as well as Python truncation analysis using Laguerre-Gaussian and Hermite-Gaussian beams.

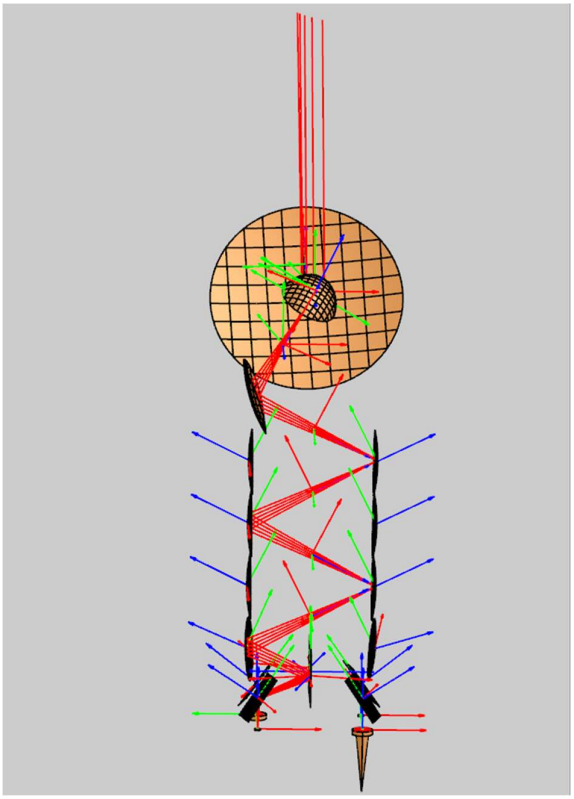

Figure 5.10 BISOU Instrument V1 Layout in GRASP. The focal plane/layout of the horns is the same as the breadboard system described above. The FTS has been increased in size as the breadboard layout above had alternating mirror sizes of 30 mm and 45 mm. This V1 layout has all the FTS mirrors set to 45mm. This increased the propagation distance between the FTS mirrors to 223mm from 215.5. The telescope is out of the plane of the FTS unlike the breadboard design where everything has been kept in plane. This design is further analysed in section 6.8

5.3 Multimoded Beam Analysis

As described above the Gaussian beam gives a good first order representation of typical truncation in an optical system based on a horn antenna used as a feed to the detectors over BISOU's bandwidth. A tophat beam (uniform intensity beam) has more off-axis power than a Gaussian. A beam from a conical or pyramidal horn will have a coherent mode set whose overall field can be represented as an incoherent sum of waveguide modes, some of which may experience higher levels of truncation.

This means that the truncation analysis described above will give a good estimate of the beam loss in the system.

However, to more accurately measure the potential distortion and aberration of the beam as it passes through the system a more representative approach is

required to simulate the horn antennae fields (conical or pyramidal in geometry).

Two of the standard horn antennas used in communications and astronomical receivers are smooth walled conical horns and smooth walled pyramidal horns. In most applications these horns are operated in a single mode state where only the fundamental waveguide mode is allowed to propagate to the detector behind the horn by limiting the size of waveguide exiting the horn towards the detector. In the circular case the fundamental mode is the TE_{11} mode (fundamental circular waveguide mode) or the TE_{10} mode for a rectangular single moded pyramidal horn. Single mode pyramidal horns are not square but rectangular to compensate for horn beam size in the vertical and horizontal planes. BISOU will have multimoded horn antennae to couple the radiation to the BISOU detectors. These detectors are resistive detectors previously developed by NASA GSFC for the PIXIE mission proposal. It is planned that it will be pyramidal multimoded rather than conical as in the pyramidal horn the polarization purity of the modes is preserved going through the horn. The field at the aperture of a smooth walled conical horn supporting a TE_{11} mode only is given by the expression (Murphy, et al., 1988)

$$E(x,y) \propto \left(\left(J_0\left(p_{1,l}' \frac{r}{a} \right) + J_2\left(p_{1,l}' \frac{r}{a} \right) \cos 2\phi \right) \hat{\mathbf{i}} + \left(J_2\left(p_{1,l}' \frac{r}{a} \right) \sin 2\phi \right) \hat{\mathbf{j}} \right) \exp\left[\frac{-jkr^2}{2L} \right], \quad (5.12)$$

in Cartesian co-ordinates, where p'_{1l} represents the *lth* zero of the Bessel function $dJ_l(z)/dz$, a is the aperture radius of the horn and L is the slant length of the horn as seen in figure 5.20 below. The complex exponential term describes the spherical wavefront, which the field acquires as it propagates in the horn from the phase centre of the horn, which is always located behind the aperture.

The field described by equation 5.12 is not cylindrically symmetric because of the azimuthal angle ϕ. The boundary conditions of the waveguide (assumed to be perfectly conducting) mean that the tangential component of E is zero, so that the field lines are perpendicular to the walls (Goldsmith, 1998). The

transverse electric field must fall to zero in the *H-plane* ($\phi = 90°$ degrees plane) and so is highly tapered in that plane. In the *E-plane* ($\phi = 0°$ degrees plane), the field is less tapered and does not fall to zero at the horn walls.

5.4 Mode Matching and Modelling Waveguides.

This method of analysis is based on a scattering matrix description of the propagation within a waveguide structure made of pure conductor. Mode matching includes full modal scattering at discontinuities in the waveguide structure and allows an extremely accurate analysis of horn antennae. This theory was proposed by (Wexler, 1967), it was followed by the foundation work of this technique by (Masterman & Clarricoats, 1971). The terahertz research group at Maynooth have developed this mode matching technique and have expanded its capabilities into numerous geometries and applications. In the modal matching analysis the changing profile of the horn antenna is replaced by a series of cascaded uniform sections, either cylindrical or square waveguide sections, each differing from the last section by being slightly larger in diameter. In the case of a smooth-walled horn many sections approximate the flared section of the horn (about 10 sections per wavelength was deemed accurate). This scheme is illustrated in figure 5.20, showing a section through a smooth-walled conical horn represented as a series of increasing radius sections representing the expanding flare angle of the horn.

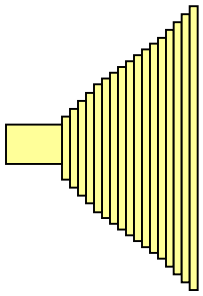

Figure 5.11 The mode matching method to represent a conical smooth walled, where the horn is replaced with a series of cylindrical sections of increasing radius.

A complete overview of smooth walled horns has been carried out at N.U.I Maynooth using this mode matching technique in the PhD thesis by Colgan in 2001 (Colgan, 2001), and a software package *SCATTER* for the exact analysis of

horns was developed over the years. Only an outline of the theory is given here to understand the framework. To analyse a horn using this tool the transmission and reflection coefficients at the section junctions or discontinuities between the sections must be determined. Propagation within the waveguide section must also be taken into account using the $e^{j\beta z}$ phase delay term. It is assumed that the field is travelling from left to right in figure 5.20 above, and so the output from one cylindrical section becomes the input for the next to the right etc. The electric and magnetic fields are required to be continuous across the interface at a particular junction between sections to comply with the underlying Maxwell's equations. The input and output mode coefficients between sections can be expressed in terms of scattering matrices. To describe propagation a diagonal matrix is used, where matrix elements describe the phase evolution of all the propagating waveguide modes.

These scattering matrices are then cascaded together so that an overall scatter matrix for the horn structure is produced. The electric or magnetic field at the aperture of the horn is then represented by a scattering matrix, which operates on the vectors of mode coefficients at the waveguide input to the horn. At Maynooth *SCATTER* was developed for both single and multimoded horns using smooth walled and corrugated structures. This program also can predict the farfield patterns of the horns, by using the appropriate Fourier transform of the horn aperture fields combined with the appropriate obliquity or projection terms. For power to be conserved properly and the fields to match at every junction Olver gives the relationship (Olver, et al., 1994):

$$\begin{aligned} [P][[A]+[B]] &= [Q][[D]+[C]] \\ [R][[A]-[B]] &= [P]^T[[D]-[C]] \end{aligned}, \tag{5.13}$$

where A and B are the transmitted and reflected coefficients on the input side and C and D are the transmitted and reflected coefficients for the output side. The matrices $[P]$,$[Q]$ and $[R]$ represent coupling between all modes at junctions. The $[P]$ matrix represents mutual coupling between modes on the left and right side of the junction, and the $[Q]$ and $[R]$ represent self-coupling between modes on the right-hand side and left-hand side of the junction respectively. Each of these matrices represent scattering between all mode possibilities, (*TE* to *TE*, *TE* to

TM, *TM* to *TE* and *TM* to *TM)*. The overall form of the matrix describing scattering between modes has the form

$$P = \begin{bmatrix} P_{TE-TE} & P_{TE-TM} \\ P_{TM-TE} & P_{TM-TM} \end{bmatrix}. \tag{5.14}$$

where the vectors of the mode coefficients [*A*][*B*][*C*] and [*D*] have the form $\begin{bmatrix} a_{TE} \\ a_{TM} \end{bmatrix}\begin{bmatrix} b_{TE} \\ b_{TM} \end{bmatrix}$ etc., where a_{TE} is a subvector of the mode coefficients for the *TE* modes. In rearranging equation 5.14 the overall scattering matrix for a single interface is given as

$$[S_{11}] = [[R^*]+[P]^{\square}[Q]^{-1}[P]]^{-1}[[R^*]-[P]^{\square}[Q]^{-1}[P]], \tag{5.15}$$

$$[S_{12}] = 2[[R^*]+[P]^{\square}[Q]^{-1}[P]]^{-1}[P]^{\square},$$

$$[S_{21}] = 2[[Q]+[P][R^*]^{-1}[P]^{\square}]^{-1}[P],$$

$$[S_{22}] = -[[Q]+[P][R^*]^{-1}[P]^{\square}]^{-1}[[Q]-[P][R^*]^{-1}[P]^{\square}]],$$

where $[]^{\smile}$ represents the transpose of the matrix and $[]^{-1}$ is the inverse of the matrix. Then cascading each junction together the overall aperture field is calculated. This is the principle of operation used in the SCATTER program to produce the field for the conical and pyramidal smooth walled horns included in BISOU analysis. A grid (x and y electric field values) that is compatible with GRASP input file formatting is used to give the aperture electric field grid points for each mode individually at the horn aperture that can be propagated with physical optics through the BISOU optical design.

The operation of cascading the scattering matrices together is central to modematching. If [S^a] and [S^b] represent two sections of a horn antenna, these can be cascaded to get the overall scattering within the sections,

$$[S^a] = \begin{bmatrix} [S^a_{11}] & [S^a_{12}] \\ [S^a_{21}] & [S^a_{22}] \end{bmatrix} \qquad [S^b] = \begin{bmatrix} [S^b_{11}] & [S^b_{12}] \\ [S^b_{21}] & [S^b_{22}] \end{bmatrix}, \tag{5.16}$$

then, the cascaded matrix elements described by [S^c] are of the form

$$[S^c] = \begin{bmatrix} S_{11}^c & S_{12}^c \\ S_{21}^c & S_{22}^c \end{bmatrix} \tag{5.17}$$

and each of the submatrices are given by (Olver *et al*. 1994),

$$[S_{11}^c] = [S_{12}^a][[I] - [S_{11}^b][S_{22}^a]]^{-1}[S_{11}^b][S_{21}^a] + [S_{11}^a], \tag{5.18a}$$

$$[S_{12}^c] = [S_{12}^a][[I] - [S_{11}^b][S_{22}^a]]^{-1}[S_{12}^b], \tag{5.18b}$$

$$[S_{21}^c] = [S_{21}^b][[I] - [S_{22}^a][S_{11}^b]]^{-1}[S_{21}^a], \tag{5.18c}$$

$$[S_{22}^c] = [S_{21}^b][[I] - [S_{22}^a][S_{11}^b]]^{-1}[S_{22}^a][S_{12}^b] + [S_{22}^b], \tag{5.18d}$$

where $[S^c]$ represents the total cascaded matrix, $[I]$, the identity matrix and $[\ ]^{-1}$ the matrix inverse. By cascading the scattering matrices for successive sections with the complete scattering matrix for all the previous sections in an iterative process, the complete scattering matrix for the overall optical system can be evaluated.

This scattering matrix method of analysis can be applied to both quasi-optical propagation of free space wave Gaussian modes and to the electromagnetic propagation of waveguide modes in a horn feed. A transformation matrix is needed to interface the waveguide modes with free-space modes but a seamless cascading is possible from a back exit waveguide section of a horn to telescope coupling radiation from the sky to give a single matrix representing the entire system.

5.5 Results from Mode Matching Code

Two different versions of SCATTER are used to generate the aperture electric fields for the pyramidal horn and the conical horn. The conical horn modematching code was developed extensively for the Planck mission and the pyramidal version of the code was developed for the SAFARI instrument, a spectrometer design developed for a concept SPICA mission (Doherty, 2012) (Gleeson, 2004).

To show that the modematching code is working we use the example of a single mode horn operating at 90 GHz and the well known farfield expressions to

compare the beam patterns produced by the modematching code. The farfield patterns are predicted in the conical version of SCATTER and the Fourier Transform of the aperture expression illustrated above in equation 5.12.

The conical horn farfield is plotted in the horizontal (E plane) and the vertical (H plane) for a conical horn with an aperture radius of 10 mm and a slant length of 110 mm at 90 GHz. (detector side waveguide dimension is limited to 1.5 mm to allow the E_{11} to only propagate). The farfield pattern prediction from SCATTER agrees well with the established expression for the farfield indicating SCATTER is accurate for a well-established example.

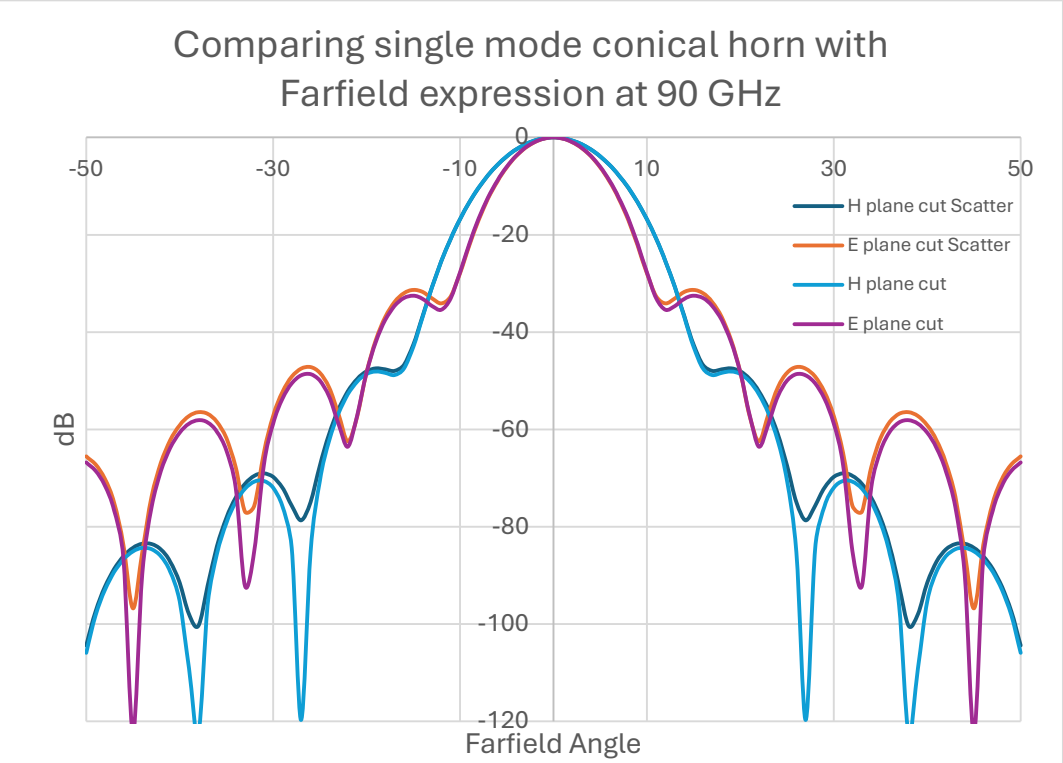

Figure 5.12 The farfield prediction of the SCATTTER modematching code compared to the traditional farfield expression for a single moded smooth walled conical horn to verify the operation of SCATTER for a conical horn

Likewise for the pyramidal version of the modematching SCATTER code a similar single moded example is run at 90 GHz. The rectangular horn geometry is large aperture width 27 mm, narrow aperture width 20 mm, slant length 100 mm and the rectangular waveguide dimensions at the back of the horn are 1.27 mm and 2.54 mm to allow (WR10) one mode propagate there.

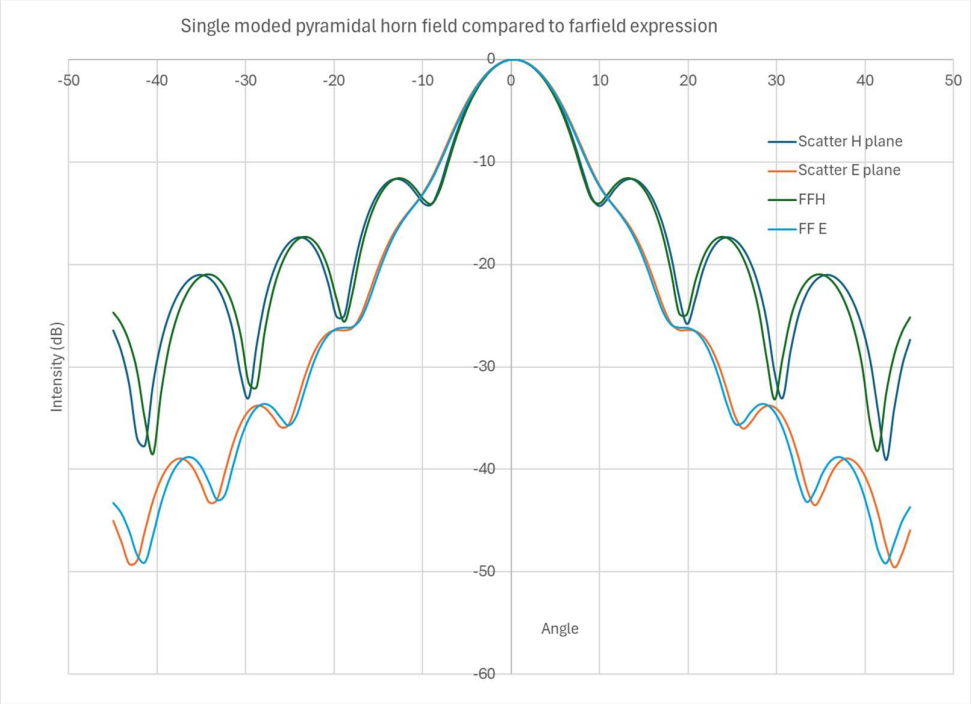

Figure 5.13 The farfield prediction of the SCATTTER modematching code compared to the traditional farfield expression for a single moded pyramidal horn to verify the operation of SCATTER for a single mode operation.

To investigate the initial effects of using a multimoded horn antenna a simple conical horn (slant length 100 mm, aperture radius – 10 mm) and a pyramidal horn with a square aperture of 100 mm slant length 100 mm and input waveguide of 6 mm are simulated using SCATTER. Ultimately BISOU is designed to have a large etendue AΩ of 4 cm^2 sr per detector. Etendue is an optical characteristic that quantifies the geometric extent of light in both area and angle, which determines the maximum amount of radiation that can propagate through an optical system. Both the horn and optics should allow this etendue. At 90 GHz this corresponds to about 30 modes propagating in the multimoded horns. The exit aperture to the horns are designed to support this

number of modes in an initial analysis. The horn geometries are a simple conical or pyramidal shape out to the aperture.

As with the top hat field described previously, the electric field is input into GRASP as a 2-dimensional grid of electric or magnetic field values. There are a different number of these fields depending on the waveguide geometry of the horn being described. In the case of the conical horn, a sum of 34 modes are required to represent the beam propagating at 90 GHz (and equivalently 24 with significant power for a pyramidal horn). These consist of a number of TE (Transverse Electric, where the Electric field is oriented perpendicularly to the direction of propagation) and TM (Transverse Magnetic, where the magnetic field is oriented perpendicularly to the direction of propagation) modes.

These modes occur due to the quantisation of the field propagation due to boundary conditions imposed by the geometry of the horn. These boundary conditions also place a limit on the mode number propagating at a specific frequency. If we assume a waveguide with perfectly conducting walls, then there are no electric fields parallel to the wall surface and no magnetic fields normal to the surface. This leads to the boundary conditions:

$$\left[E_z\right] = 0 \text{ and } \left[\frac{\partial B_z}{\partial n}\right]_{os} = 0$$

where E_z is the electric field parallel to the walls of the waveguide and $\frac{\partial B_z}{\partial n}$ is the magnetic field perpendicular to the surface. For example, in a pyramidal horn with rectangular symmetry. Assuming a pyramidal horn with one corner placed at the origin and the other at a point (a,b). The transverse wave equation in two dimensions is:

$$\frac{\partial^2}{\partial x^2} + \frac{\partial^2}{\partial y^2} = -\kappa^2 E \tag{5.19}$$

For the magnetic field the boundary conditions state that the field must be zero on the walls of the waveguide. So, the above equation must be 0 for x=0, x=a, y=0, y=a.

Using a trial solution of the form:

$$E_z = E_0 \sin(Ax)\sin(By) \tag{5.20}$$

The solution to the transverse wave equation becomes:

$$-A^2 E_0 \sin(Ax)\sin(By) - B^2 E_0 \sin(Ax)\sin(By) = -\kappa^2 E_0 \sin(Ax)\sin(By) \quad (5.21)$$

where

$$\kappa^2 = A^2 + B^2$$

Applying the boundary condition: $E_z(a, y) = 0$

$$E_0 \sin(Aa)\sin(By) = 0$$

$A = \frac{m\pi}{\lambda}$ for m=0,1,2…

And similarly:

$B = \frac{n\pi}{b}$ for n=0,1,2…

This gives the complete solution for the TM mode:

$$E_z = E_0 \sin\left(\frac{m\pi x}{a}\right)\sin\left(\frac{n\pi y}{b}\right)e^{ikz - i\omega t}$$

(5.22)

The derivation of the TE mode is similar. (Ellingson, 2020). These modes are propagated through the system in GRASP separately then summed up after to simulate the beam after propagation through the system.

Below is a sample of some of the conical horn modes, along with the total beam once all are summed together at the horn aperture plane:

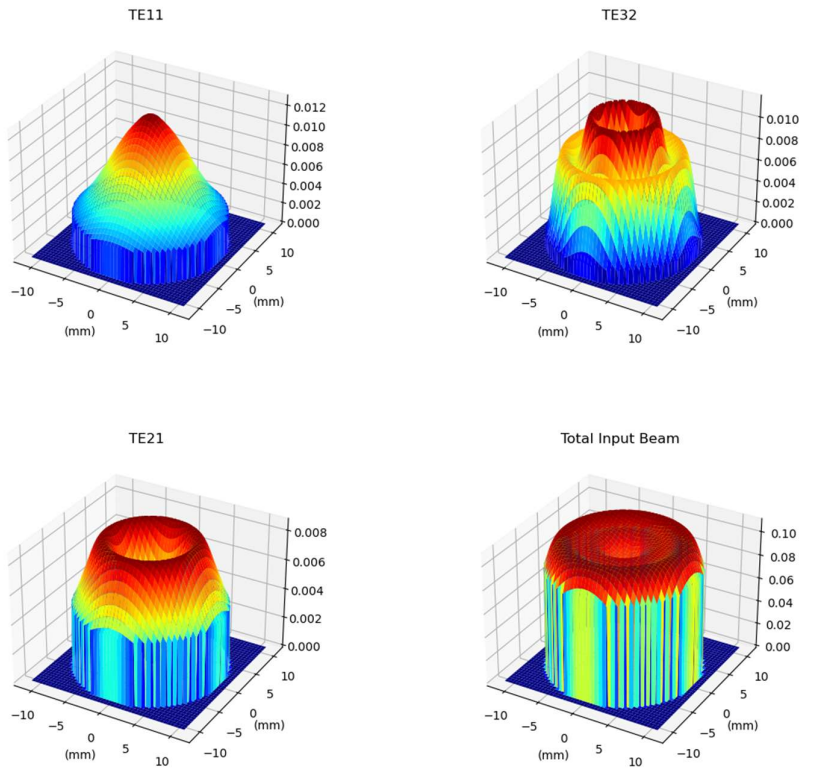

Figure 5.14 A sample of some of the conical horn input modes along with the total beam once all 36 modes have been summed incoherently.

Below is a sample of some of the pyramidal horn modes and the total beam summed together coherently at the horn aperture plane.

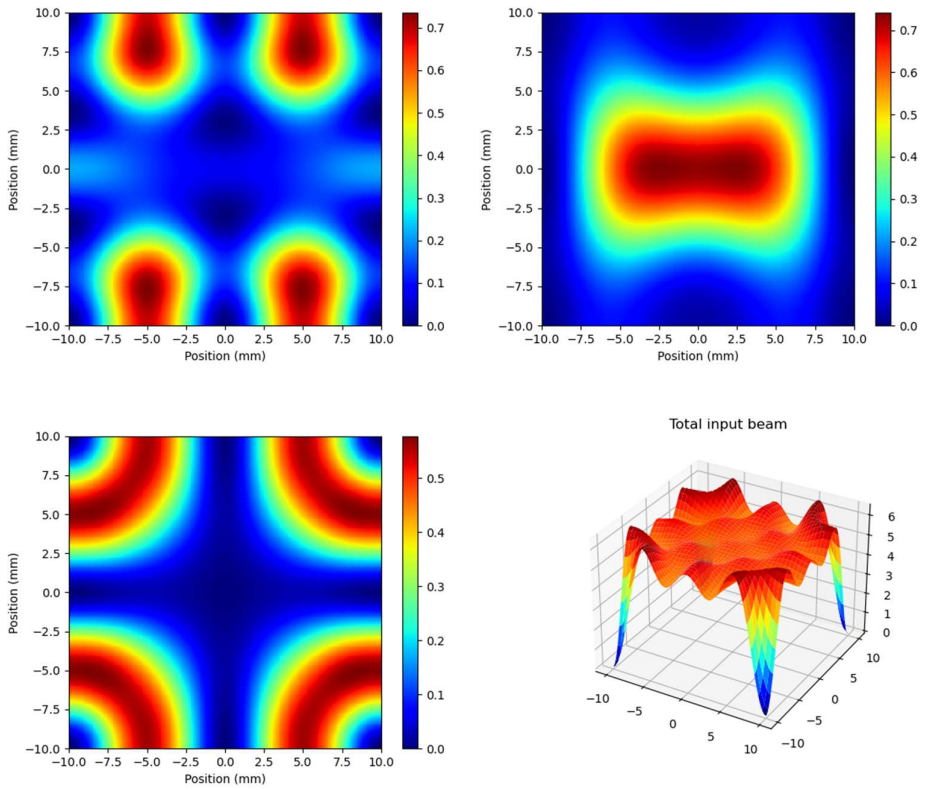

Figure 5.15 A sample of some of the conical horn input modes along with the total beam once all 24 modes have been summed incoherently at the horn aperture plane.

6 Chapter 6: BISOU Design Iteration

This chapter outlines different design iterations that were analysed and an evolution of the BISOU optical design. To assess the optical designs either a simple Gaussian input in GRASP was used to represent the horn antenna beam or a series of modal aperture fields of a multimoded conical or pyramidal horn were included.

6.1 Initial layout with a Gaussian Beam Input and No Dichroic elements included

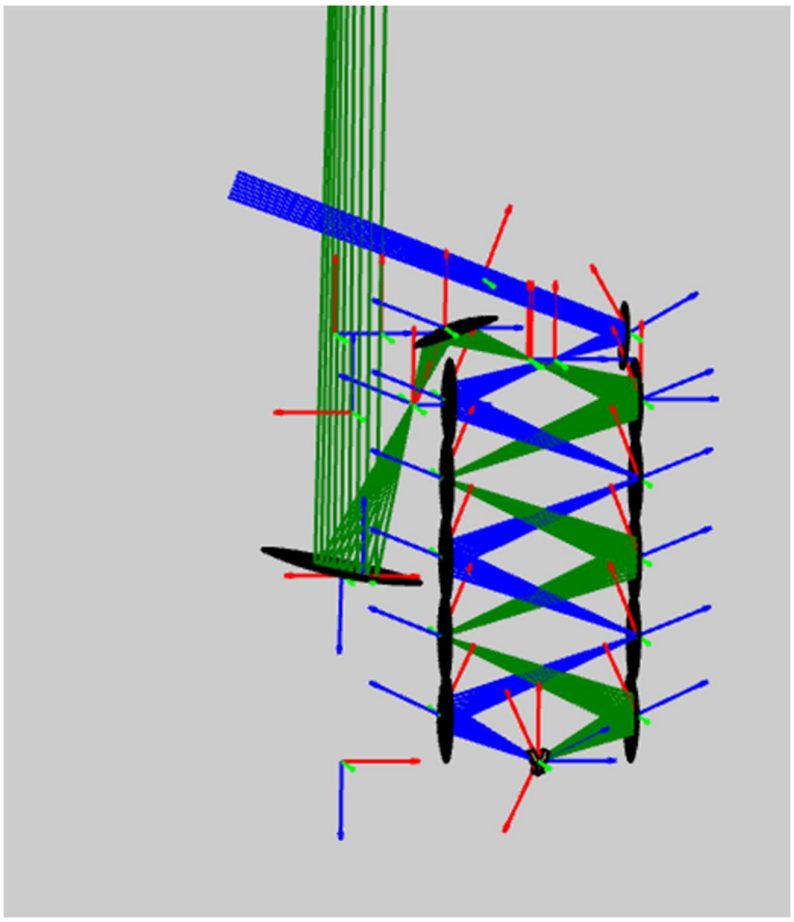

Figure 6.1 Initial design without taking into account the geometric footprint of the horns, this was just to get the main optics right.

Figure 6.1 shows the initial optical design of the BISOU Breadboard FTS system with telescope in GRASP using optical rays to illustrate the beam paths. This design was implemented without the inclusion of a horn physical footprint

and with only two beams propagating through the system, where frequency components are not separated. We illustrate a beam propagation at 90 GHz, the lowest frequency channel. One optical path goes to the telescope and onto the sky and the other goes to the blackbody reference calibrator {illustrated in figure 6.1}. For simplicity these beams were also originating from the same location at the centre point between the FTS mirrors and propagate towards the sky or calibrator. The exact location of the input beam can be varied by varying the focal lengths of the first mirrors in the FTS optical train and is a degree of freedom in initial designs.

The divergence of the beam as it propagates through the system is frequency dependent and a lower frequency beam of 90 GHz will diverge much more significantly than a higher frequency beam.

The divergence of a beam is given by the relationship (Goldsmith, 1998):

$$\theta = \tan^{-1}\left(\frac{\lambda}{\pi\omega_0}\right) \tag{6.1}$$

As divergence of the beam is largest for a low frequency beam, the level of truncation of this beam can be assumed as a worst-case scenario for the band, and the level of truncation for the higher frequency beam would be much less significant (assuming single mode operation. The multimoded nature of BISOU is more complicated). This means that any mirror sizes determined to be necessary for the low frequency beam, can be assumed to be sufficient for the higher frequency beam as well.

A Gaussian beam of various sizes is propagated from origin point and the amount of this beam transmitted through the entire system is used to determine the necessary diameter of each mirror. This method of beam propagation was much easier to implement than trying to send a beam from the opposition direction from the “sky” as would be the case in the actual operation of the system. The principle of reciprocity means that detecting a beam from the sky at the horns after propagating through to the horns and sending a beam from the horns through the system in the other direction, should give equivalent results. This greatly simplifies the simulation of BISOU in GRASP. As the

properties of the beams at the horns can be clearly defined, and then the effect on an equivalent beam on the sky can be measured (Heki, 2024).

The BISOU consortium ultimately plan to have 4 horn antennas & beams, where the full frequency bandwidth is split into two channels using dichroic beam splitters to separate the high and low frequency beam components. This is to facilitate the analysis of the CMB dominated lower frequencies and the higher frequency channel for foreground and atmospheric analysis.

Initial tests of the truncation of the beam using Gaussian beams in GRASP and also truncation analysis code showed good agreement between the theoretical predictions from GBMA truncation code and simulated propagation from GRASP, results for example systems are given in this thesis in section 4.1.

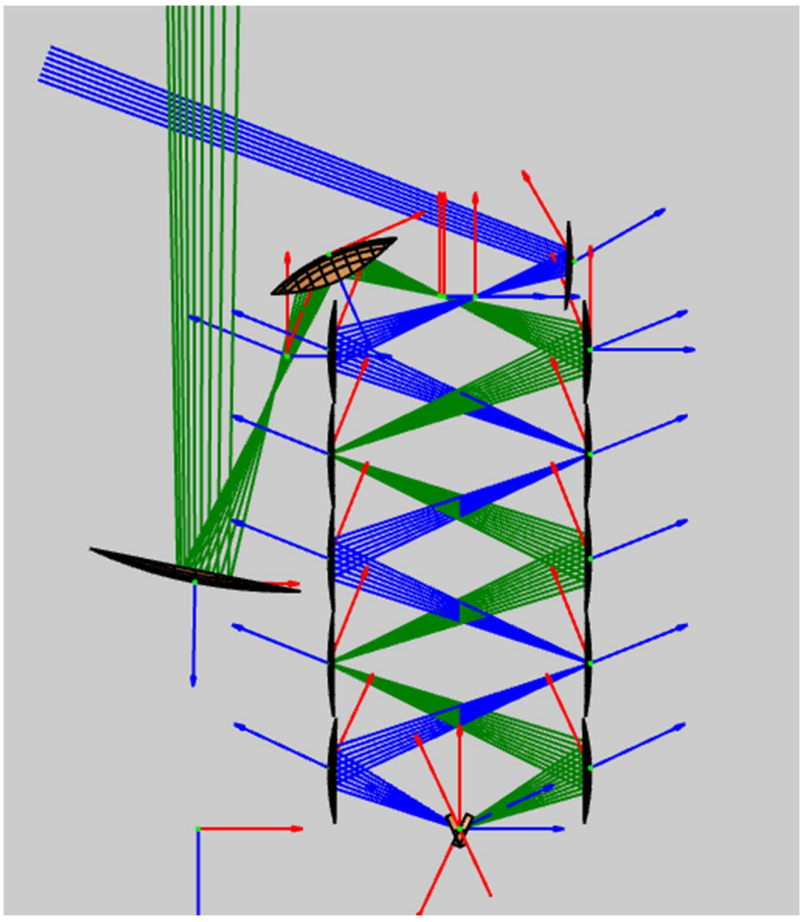

Figure 6.2 Layout with longer focal length and larger radius secondary mirror. The secondary mirror size was increased as the beam was too large. The focal length of the secondary mirror was increased to try and reduce the beam size at the primary mirror.

6.2 Best in-Plane Design – Two Dichroics included.

The next step was to include the two horns and two dichroics in the design. One horn is the lower frequency channel horn (90-350 GHz) and then the higher frequency horn (350 to 2000 GHz). A design was implemented for only the focal plane, ignoring the rest of the instrument for now. The main difficulty in implementing the design is in keeping the correct angle of illumination of the dichroic for both horns.

The horns were included in these GRASP designs using a pyramidal shaped volume with a height (base to point) of 150 mm, with small boxes on the end to represent the size of the detector footprint. This should be representative of the horn and detector footprint ultimately. This was purely used as a geometric indication of the size constraints allowed in the design and served no function optically in GRASP, they are included to show that the designs fit geometrically.

The dichroics are represented by plane mirrors to show the path the reflected and transmitted beams would take.

The angle of incidence of the beam on the dichroic must be kept shallow at no more than 22.5 degrees due to the optical properties of the dichroic and its correct operation which is another optical design constraint. The overall width and height of the BISOU Breadboard system also has size constraints due to the need for a cooling system and to fit within a fixed cryogenic enclosure.

This led to some challenges with the design as intuitively the easiest way to decrease the angles of the horns is to increase their distance horizontally and alternatively the easiest way to decrease the width of the overall system is to increase the angle of incidence on the dichroic. The only design that could be achieved using two dichroics while keeping the entire system in one plane was the design in figure 6.3 below.

The angles of the beams relative to the dichroics are all within the required 22.5 degrees, and the overall system is a reasonable width ≈ 550 mm and height ≈ 730 mm

The overall system was also kept in a single plane, this would hopefully aid the simplicity of construction and cooling and avoid any potential optical effects from requiring the beam to be reflected into/out of the plane.

However, it was decided that this design was not optimum. The two pairs of horns at either side are at very large angles relative to each other (due to having to meet the angle of incidence requirement on the dichroic), this would likely cause issues thermally as ideally the horns would all be kept at the same stable temperature close to one another.

It was also decided that the outer horns on each side would likely be partially blocked/shadowed by the FTS mirrors due to how little space there is between the dichroic, horns and FTS mirrors on each side. As can be seen with the horn on the right side of the diagram, a beam coming from/going to the horn would likely be partially blocked by the FTS mirror. A beam travelling through the path on the right would have almost 1% blocked by the bottom FTS mirror making it unworkable.

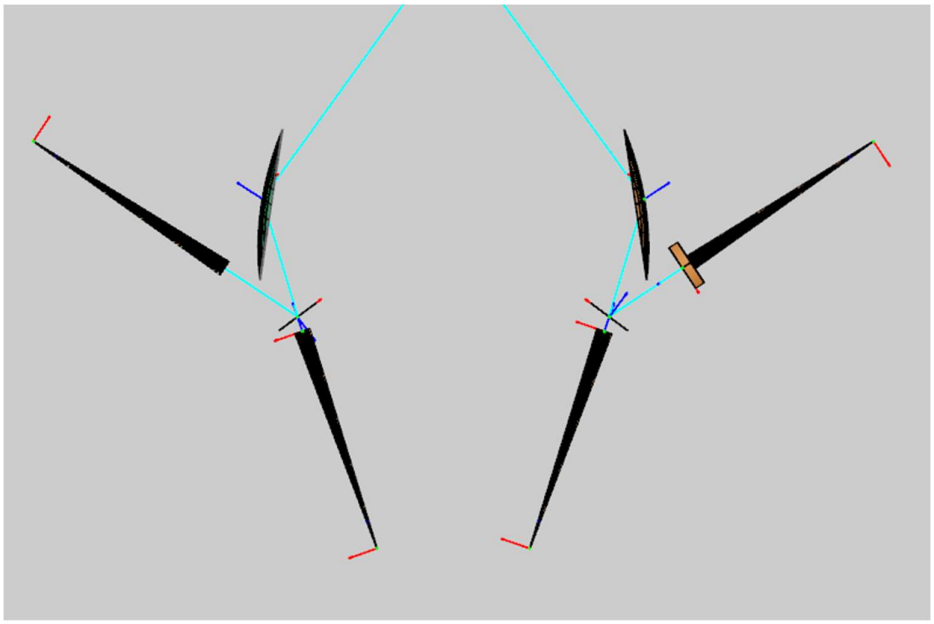

Figure 6.3 In-plane design with two dichroics. Only the horns, dichroics and first FTS mirror are shown as the first step is to make sure the focal plane layout of the design is suitable before moving on to the rest of the design.

6.3 Out of Plane Horn Antennas Design (Version 1)

Moving the horns and dichroics out of the plane required the addition of two extra plane mirrors to deflect the beams out of the plane . This raised the potential issue of extra truncation/aberration of the beam. The angle of the beam on each dichroic was kept to within the allowed 22.5 degrees and it was hoped that this would allow more space for flexibility in the sizing of the plane mirrors.

However, the increased propagation distance between the horns and the first FTS mirror and the limited allowable size of the plane mirror lead to significant truncation of the beam, with over 15% of the beam being lost before the first FTS mirror. After some consideration it was decided that this design was not feasible as the horns were too far out of the plane to fit within the allowed cryogenic enclosure.

The detector ends of the horns out of the plane (out of the page in the first image below and pointing down in the second image) were too far out of the plane to fit within the enclosure at 350 mm from the centre of the FTS to the detector end of the horns as shown .

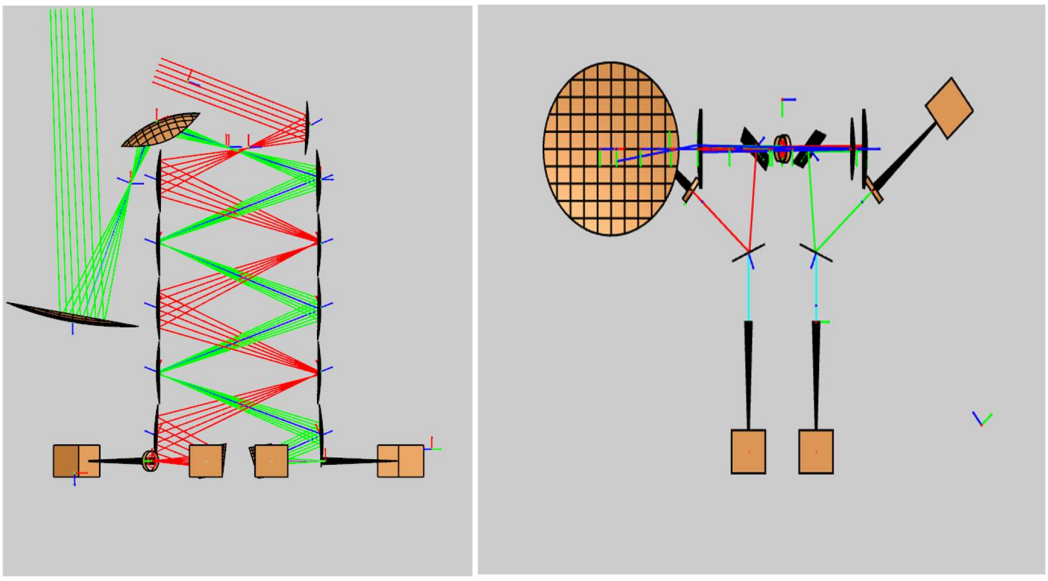

Figure 6.4 First attempt at an out of plane design with two dichroics. Front view (left) and top down view (right) 2 extra plane mirrors were also required to bend the beam out of the plane of the FTS. This adds to the complexity of the design as these mirrors need to be taken into account for truncation effects. This was initially a more promising design than that in figure 6.3 so full ray tracing is included.

6.4 Out of Plane Horn Antennas (Version 2)

(a)

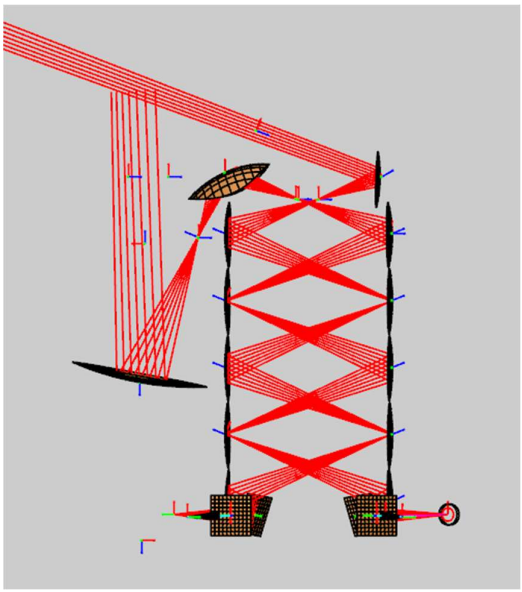

(b)

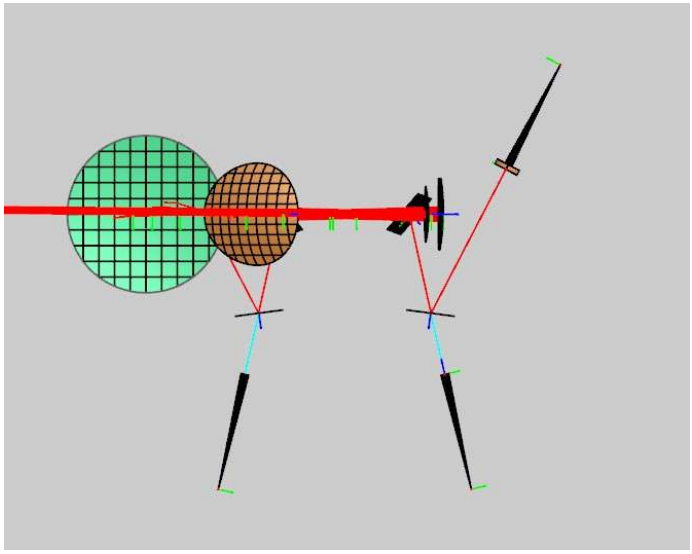

Figure 6.5 Front view (a) and top-down view (b) of the second out of plane attempt. It was attempted to reduce the overall width of the system by moving the outer horns closer to the FTS mirrors.

For the second attempt at an out of plane horn antenna layout, it was attempted to reduce the overall width of the system and also minimise the angles of the horns. This was achieved by moving the outer horns closer to the sides of the FTS. However, this resulted in the plane mirrors being closer to the reflected beams from the bottom FTS mirrors and would lead to significant shadowing of the beams.

Taking the example of horns on the right. A beam travelling from the bottom FTS mirror towards the second FTS mirror is blocked by 10% by the plane mirror. These plane mirrors cannot be made any smaller to avoid beam losses from the beams reflecting from them. This leads to a compromise between leaving the plane mirrors large enough to avoid truncating the beam but small enough to avoid blocking the beam after reflection from the FTS mirror.

This design also had the same issue as previous designs and the out of plane horns would be too far out of the plane to fit within the allowed cryogenic enclosure with the detector ends of the horn being 350 mm out of the plane of the FTS. As shown previously in section 2.2 there is finite space both below the FTS and out of the plane of the FTS to fit within the constraints of the cooling system.

6.5 Optical design with single dichroic (Version 3)

A single dichroic design was also considered, where instead of an individual dichroic for each horn, a dichroic is shared as a single component between two horns. This would potentially reduce truncation and potential aberration of the beam by reducing the number of surfaces required, eliminating the need for extra plane mirrors to direct the beam out of the plane of the FTS.

This would also reduce the overall width of the system as it would allow the removal of one of the dichroics and both plane mirrors, helping to keep the system within the given space constraints.

Figure 6.6 is an example layout of the 4 horn locations, dichroic and 2 FTS mirrors.

In initial versions of this design, the dichroic was placed at the midpoint horizontally of the FTS column, with an angle of incidence on the dichroic of 11.7 degrees for the calibrator (blue) beam. The angle of the telescope (green) beam was set to 22.5 degrees, the max allowed for the dichroic. This was done to maximise the total allowed space for each pair of horns, as the max angle of incidence for the dichroic was limited to 22.5 degrees. Setting one beam to this value would maximise the available space to fit the other pair of horns.

As the angle of incidence for the other pair of horns would need to be less than this 22.5 degree value, they were placed above the telescope horns. A nominal value of 20 mm was chosen as the diameter of the example horns meaning for the pair of horns on either side of the dichroic to be touching, an angle of incidence of 11.7 degrees was chosen for the calibrator beam.

The beam reflected from the dichroic would need to travel from the FTS mirror, to the dichroic, to the horn and with an angle of incidence of 22.5 degrees the vertical location of the dichroic becomes fixed to allow the beam to reflect between both locations. The same is true for the calibrator (blue path). The calibrator beam reflects through as smaller angle from the dichroic, meaning the horns and dichroic must be relocated slightly to allow this beam to hit the FTS mirrors. As the angle of the beams is fixed, any change in focal position must be achieved by moving the dichroic and horns.

To allow the calibrator beam to intercept the mirrors in the correct place, whilst not also causing the telescope beam to be incorrect, it was determined that it would be necessary to offset the dichroic (and thus all four horns) from the initial centred position. The dichroic was moved 10 mm down from the initial location and 20 mm to the right. The dichroic (and horns) were also tilted at an angle of 12 degrees to allow the telescope (green) beam to reflect off the FTS mirror correctly.

The bottom FTS mirror on the left was also moved down so the calibrator (blue) beam was able to reflect off the centre of the mirror. However, this still did not succeed in creating enough space between the horn apertures themselves, below the FTS column and the horns were too close together to fit the aperture width required.

Modifications of this design were attempted, and it was found that the only way to solve both these issues would be to increase the angle of incidence of the beam on the dichroic to roughly 25 degrees. This would not be possible due to the way the dichroic is designed for correct operation and so this design had to be abandoned.

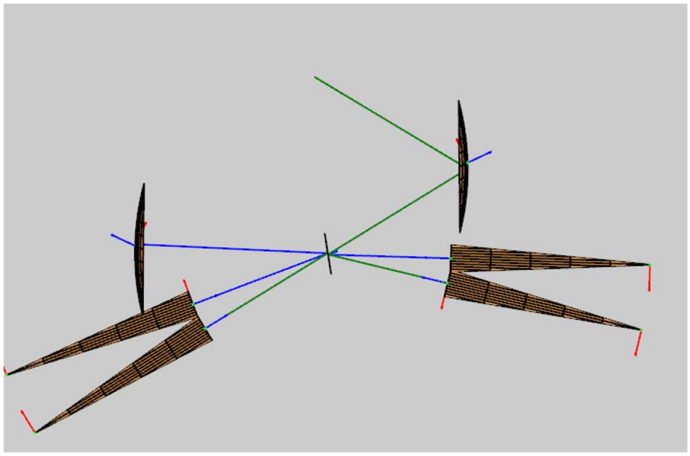

Figure 6.6 Single dichroic design attempt. The location of the horns was too close to the FTS mirrors.

6.6 Single Dichroic element (Version 4)

To avoid the space constraints described above from the horn apertures being too close to the bottom of the FTS mirrors a set of four plane mirrors was considered. This would allow the beams from the FTS to be reflected and allow the positioning of the horns a greater distance vertically below the FTS column.

As described previously the additional plane mirrors could cause issues with regard to truncation or blocking of the beam. Moving the focal plane further down allowed more space for the plane mirrors and more flexibility with the position of the horns.

To avoid the additional plane mirrors truncating the beam path, the horns were positioned significantly closer to them. This would also require modification of the other mirrors in the system to ensure consistent beam size/properties. It was decided to use different plane mirror sizes for each of the 4 horns as the high frequency beam is smaller and diverges less quickly and so for an equivalent

initial beam waist it is possible to use a smaller mirror for a high frequency beam while still maintaining the same level of truncation.

The size of these plane mirrors meant that they needed to be spaced further apart than if an intermediate size was chosen. This spacing of the plane mirrors (and thus the spacing of the horns) meant that the intercepts of the calibrator beam and the telescope beam on the dichroic could not both be exactly in the centre as originally planned. It was decided that this was not an issue as the total required size of the dichroic would still only be 60 × 60 mm and this was small enough that the optical properties would be consistent across the surface, and so the two beam intercepts were not required to be in the same location.

The plane mirrors, while better located than in the previously mentioned out of plane designs, still blocked the beam by a small but not insignificant amount. A 10 mm 90 GHz Gaussian beam travelling from the second horn towards the left FTS mirror would be blocked by 0.03%. A 10 mm 90 GHz Gaussian beam travelling from the 4th horn towards the right FTS mirror would be blocked by the upper plane mirror by 0.004%. While very low, these beam losses are important as they place an upper limit on the size of the folding plane mirrors. The plane mirrors cannot be increased in size without increasing the subsequent shadowing or blocking of the beam along the path as illustrated in figure 6.7.

For a 9 mm 90 GHz Gaussian beam at the input, there is an almost 17% beam loss through the system. 5.5% of this loss occurs at the folding plane mirror. However, this plane mirror cannot be increased in size to avoid blocking the beam coming from the FTS mirror.

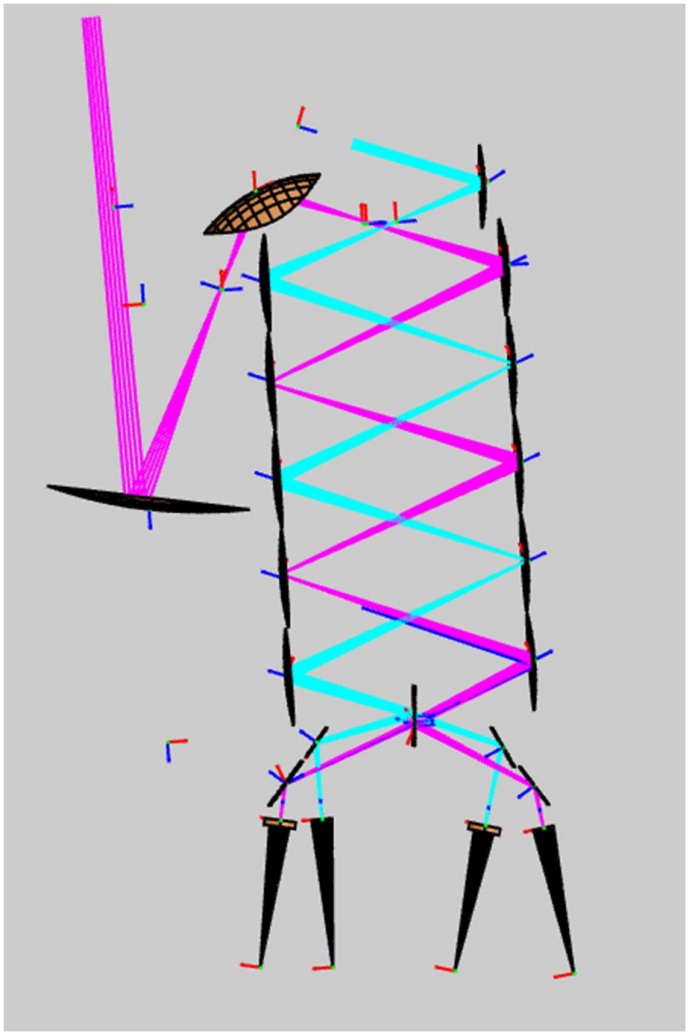

Figure 6.7 Single dichroic design with the addition of folding mirrors to move the horns down further from the FTS.

The designs attempted previously indicate that any feasible final design would require the use of a single dichroic and would likely require the horns to be out of the plane of the FTS

6.7 Breadboard Design

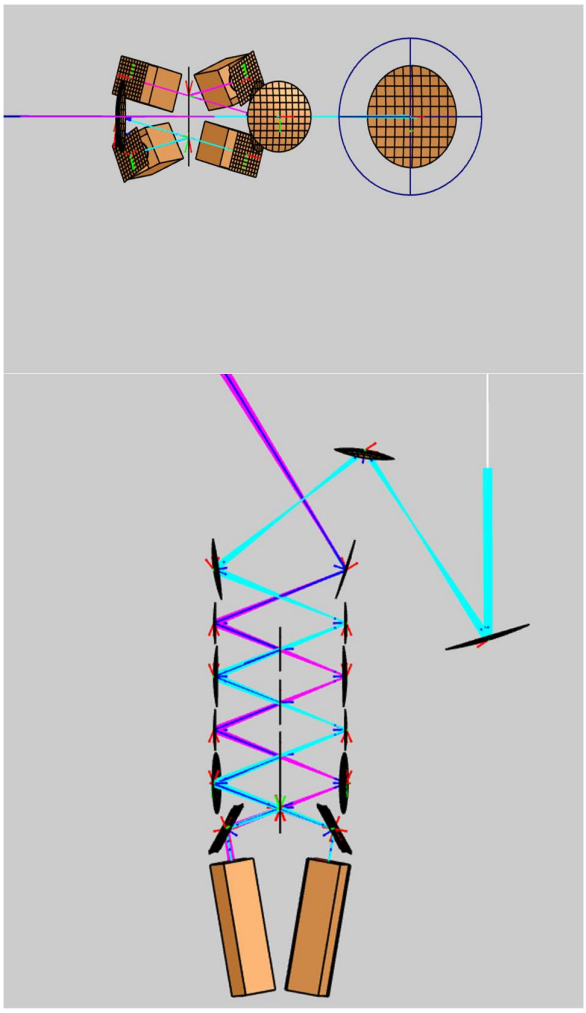

Figure 6.8 selected BISOU breadboard design. Created by Morgane Loquet Le Gall.

The previous designs indicated that the use of a single dichroic, and the positioning of the horns out of the plane were the only feasible design option. The final design chosen is shown above. The 4 horns (represented here by the rectangular boxes at the bottom) are placed out of the plane above and below the plane of the FTS. There are four folding plane mirrors to fold the beams from the FTS out of the plane and down below the bottom of the FTS.

The telescope is kept in the plane of the FTS column. The FTS column has mirrors of alternating sizes 30 mm and 45 mm. This was found to have no effect on the truncation of the beam as the beam will be converging and diverging on

alternate mirrors. Truncation values for both potential FTS layouts were identical.

This also reduces the propagation distance from the centre of one mirror to the centre of the next to 215.5 mm from 223 mm. As the plane mirrors are not in the same plane as the FTS mirrors this avoids the problem of them blocking the FTS mirrors. This also allows there to be much less limitations on the size of the plane mirrors so they can be any size sufficient to avoid truncation.

Having the horns out of the plane in both directions is also good for the thermal performance of the system. The ends of the horns being much closer together than in previous designs means they can be cooled much more efficiently and the temperature between them will be much more stable.

As this was the working design iterated from previous designs more detailed simulations were performed than for the previous designs. A 10 mm waist (or equivalent) Gaussian beam was propagated from each horn through all 4 optical paths to test its truncation. The addition of the extra plane mirrors and the added complexity of the horns being placed out of the plane did not affect the performance of the system negatively as truncation of the beam was reasonable for all 4 optical paths. The addition of 4 extra plane mirrors did not negatively affect truncation levels as they could be made sufficiently large for the given beam size.

Table 6.1 below shows truncation levels for all 4 beam paths includingvalues from GRASP, and values calculated from the GBMA truncation analysis code.

A Gaussian beam of 10 mm was chosen as the base beam size at 90 GHz. The size of an equivalent Gaussian beam from a horn is frequency dependent, so the waist of the high frequency beam was scaled accordingly. A higher frequency of 350 GHz was chosen. This means that its radius would need to be scaled by $\frac{350}{90} = 3.888$ times. So, for a base frequency 90 GHz beam of waist 10 mm, the frequency-scaled beam would have a waist of 2.5714 mm.

	GRASP	GBMA truncation
90 GHz Telescope Beam	0.9694	0.9563
350 GHz Telescope Beam	0.9806	0.9878
90 GHz Calibrator Beam	0.9709	0.9629
350 GHz Calibrator Beam	0.9775	0.9910

Table 6.1 Truncation values from GRASP and Python. The initial beam is normalised to 1. The values shown are the proportion of the beam remaining after propagation through the system

The level of truncation for each of the 4 beams is within a reasonable limit accounting for how the rims of the mirrors are defined in GRASP. The above values show That the optics is of adequate size to allow the beams propagate.

The beams were also plotted after propagation through the system over both paths (sky and calibrator).

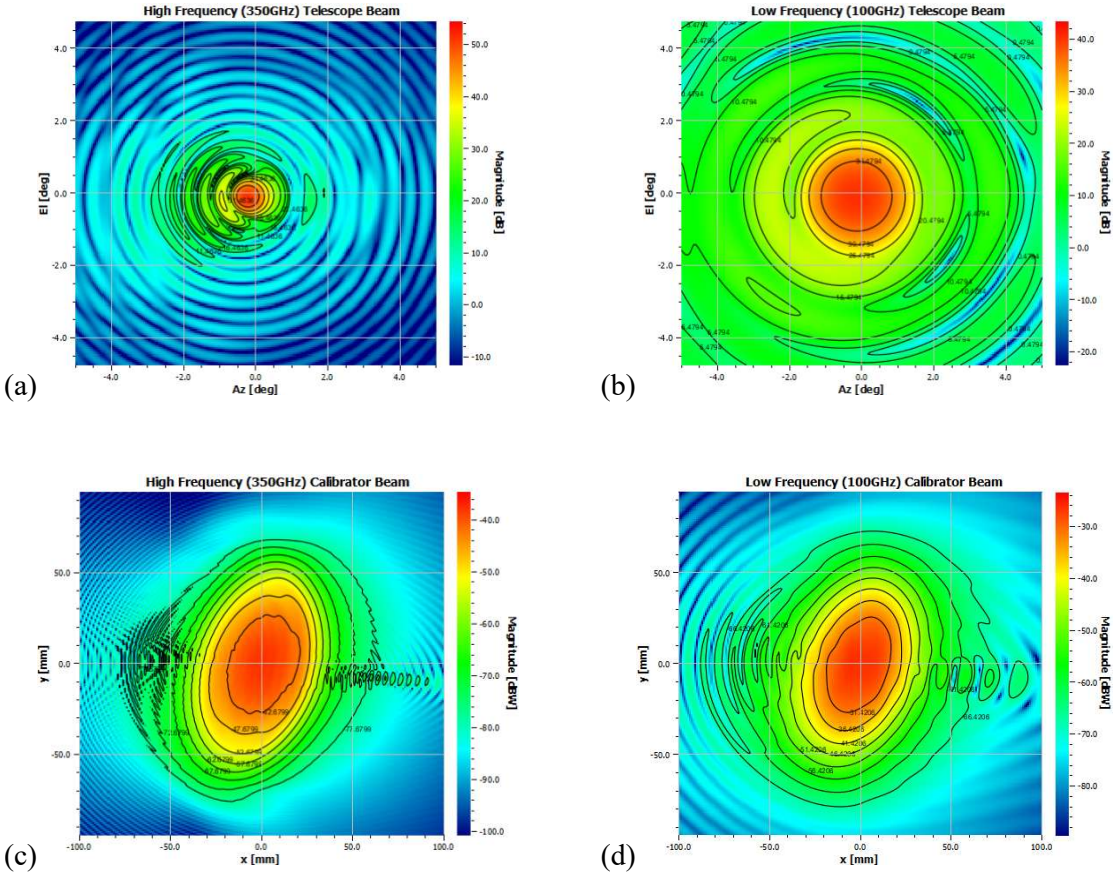

Figure 6.9 The four beams plotted after propagation through the system. (a) the higher frequency 350 GHz beam propagating through the telescope. (b) the lower frequency (100 GHz) beam propagating through the telescope. (c) the high frequency calibrator beam and (d) the low frequency calibrator beam.

There was minimal distortion of the beams, with the beam profile maintaining a symmetric Gaussian shape. The higher frequency main beam is also symmetric showing some wider scale low sidelobe level aberration. The low level of truncation combined with minimal distortion of the beams indicated that this design was acceptable.

6.8 BISOU Flight Instrument V1

Once the breadboard design had been finalised a design for the main instrument could be more thoroughly considered. The main BISOU instrument has a similar optical layout to the breadboard design with the main change being the reorientation of the telescope to be 90 degrees out of the plane of the FTS.

This was due to space constraints in the enclosure and cooling system. Initial concepts for the main instrument design had an extra plane mirror before the secondary to perform the bending of the optical path, leaving the FTS all in a single plane, and the secondary and primary telescope mirrors in a plane at 90 degrees. This extra plane mirror was removed as the addition of an extra plane mirror could lead to more truncation/aberration of the beam. It was decided to modify the secondary mirror and use that single elliptical mirror to deflect the beam towards the primary mirror out of the plane of the FTS.

The V1 BISOU instrument design is shown below in Figure 6.11

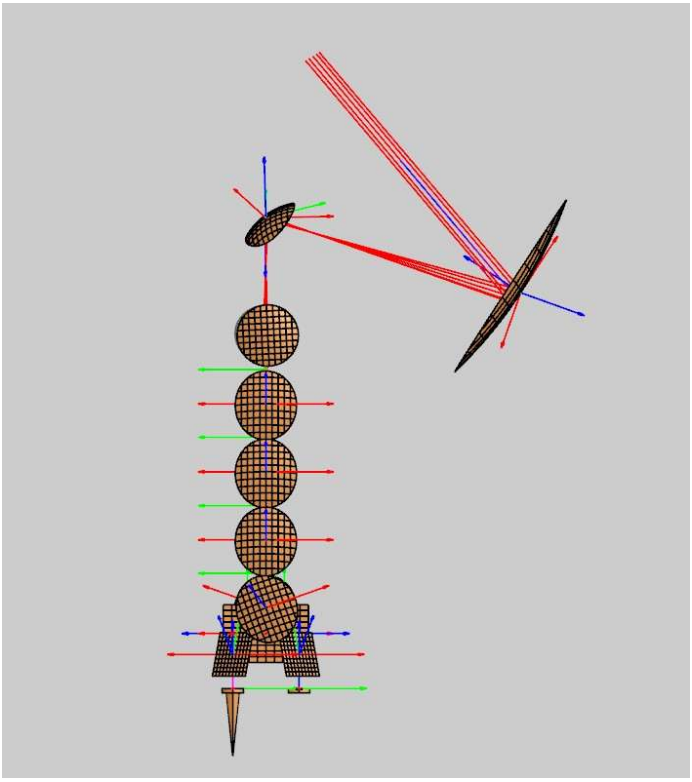

Figure 6.10 BISOU V1 instrument design. The FTS column and focal plane remain similar to the systems described previously. The telescope is now 90 degrees out of the plane of the FTS. This requires a modification of the secondary mirror. The telescope is out of the plane to accommodate space constraints in the gondola. This could add distortion to the beam compared to keeping everything in plane.

This finalised instrument design was analysed in the same way as the breadboard design described previously. Firstly, with a Gaussian beam to check for truncation and distortion of the beam.

Initial simulations with a Gaussian beam indicated some off-axis distortion of the beam:

(a) (b)

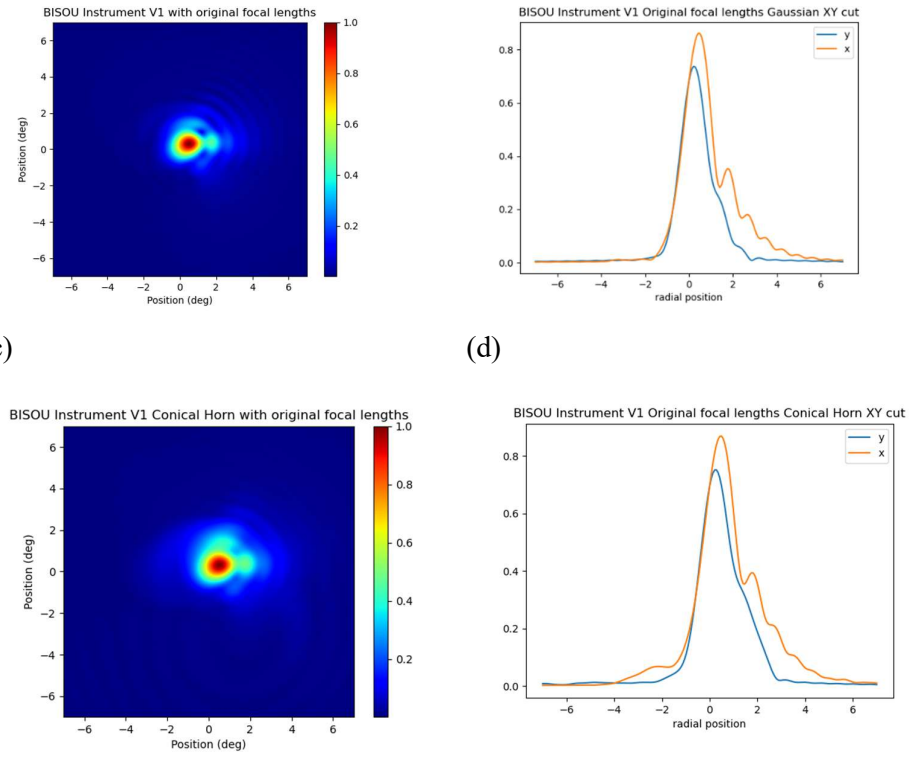

Figure 6.11 plots (a) and (b) show plots of a Gaussian beam propagated through GRASP. Plots (c) and (d) show normalised plots generated by propagating the conical horn beam modes at 90 GHz through the same system. Some distortion of the beam is apparent in both cases.

It was believed this occurred due to the bending of the beam out of the plane by the secondary mirror and the required short focal length of the secondary mirror to mechanically fit the telescope in the envelope of the available volume. To retain the same throughput of the system, it is required that the beam size on the primary mirror be kept constant relative to the 150 mm radius of the primary to maximise coupling to the sky.

The original output focal distance of the secondary mirror was 75 mm. This initial value was chosen to obtain a specific beam size on the primary mirror. To show the secondary mirror is responsible for the aberration of the beam on the sky seen in figure 6.12. its focal length was increased to 150 mm. This should help reduce the aberration. This design change was simulated using the same initial Gaussian beam properties as before and the beam plotted in figure

6.13 appears to improve the off-axis aberration before the primary mirror, and indicated that any distortion present in the final beam was likely occurring at this secondary mirror where the beam was being deflected out of the plane. Deeper analysis of this mirror design is planned for future iterations as it plays a critical role in the beam characteristic on the sky. Distorted beams are not a major problem for BISOU but the higher cross-polar levels in the distorted beam may be of concern.

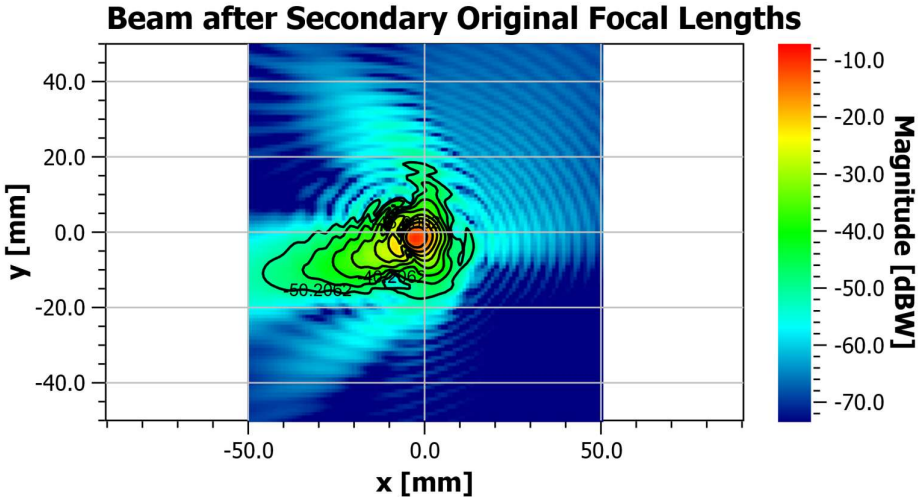

Figure 6.12 Plot shows the beam after the secondary mirror before hitting the primary mirror. The distortion present indicates that it is the design of the secondary mirror which is leading to the distortion in the final beam

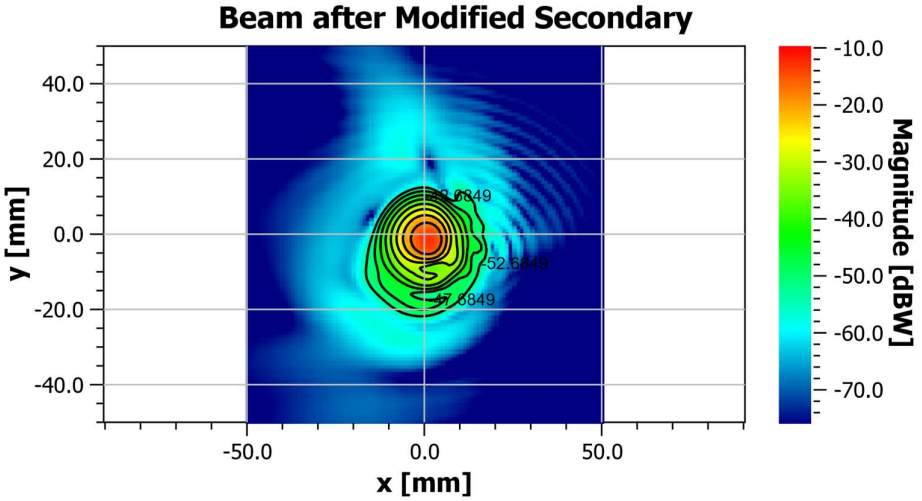

Figure 6.13 Plot shows the beam after the secondary mirror with the modified focal lengths described previously. This is a significant improvement in beam quality indicating that it was the design of the secondary mirror which was likely introducing distortion into the final beam

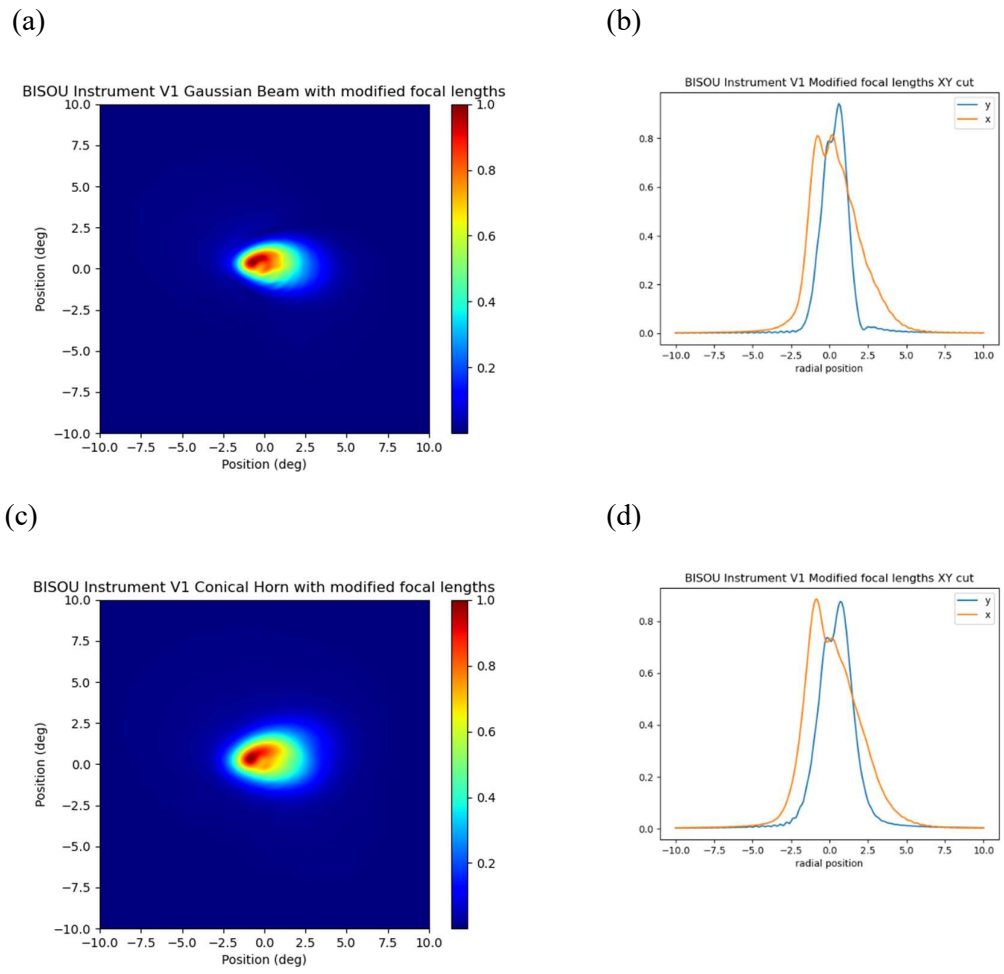

Figure 6.14 Plots (a) and (b) above show the Gaussian beam plots from GRASP with the modified focal lengths in BISOU V1. These plots initially appeared to be an improvement in beam quality compared to plots (a) and (b) in figure 6.12. However, plots (c) and (d) show the conical horn beam mode simulation for the same system with these modified focal lengths. This system no longer appears to be an improvement from the original focal lengths.

Thus, it was decided to revert to the original BISOU V1 instrument design, which would undergo full simulation along with the finalised BISOU breadboard design. This test did illustrate the benefits of performing the more detailed modal analysis as opposed to just the Gaussian beam simulation from GRASP as it can indicate different results.

These two final designs were analysed using the multimoded horn modes described in section 5.3. The simulations were performed for the system shown above in figure 6.8 with the first test being conical horn modes. The simulations were also performed using pyramidal horn modes, with the mirror layout shown

above, and with the mirror rims changed to square rims to match the pyramidal shape of the input horns.

The square rims were tested as the final design for the BISOU horns will likely be pyramidal horns with rectangular symmetry. These horn modes were analysed with both circular and square rimmed mirrors to see any potential difference in truncation/aberration of the beam. If the beam profile is affected drastically then the BISOU FTS mirrors may be changed to have square rims to better match the square symmetry present when using a pyramidal horn.

Only a low frequency of 90 GHz was analysed with this method as described in section 5.3. The number of modes able to propagate from a horn is proportional to the frequency of the radiation. The conical horn being simulated using all propagating 34 modes at 90 GHz (equivalently 24 modes for the sample pyramidal horn with significant power), but this number would be much higher if the higher frequency band at 350 GHz was simulated. This would lead to drastically increased computation time.

6.9 BISOU Instrument V1 and Newest Breadboard Design Truncation Results

First truncation analysis was performed for both designs using the Laguerre-Gaussian truncation analysis process as described previously. This was initially done with the assumption of a circularly symmetric beam, and circular rimmed mirrors. This process was carried out for both the most recent BISOU Breadboard design and the BISOU V1 flight instrument design. This was completed to ensure all optical components were of sufficient size to avoid truncating the beam, while also keeping the system within the size constraints imposed by the cooling system and enclosure.

Truncation analysis results for the Breadboard design are shown in Table 6.2 below:

	M5	M4	M3	M2	M1	Secondary	Primary
GRASP (circular mirrors)	0.9939	0.9919	0.9888	0.9872	0.9824	0.9775	0.9694
Laguerre modes	0.9932	0.9932	0.9815	0.9815	0.9631	0.9594	0.9563

Table 6.2 Circularly symmetric truncation analysis values for the BISOU breadboard design. Spillover values from GRASP are compared with truncation values from the Laguerre-Gaussian truncation analysis python code.

These truncation values are compared with spillover values from GRASP with the initial assumption of circular mirrors with a circularly symmetric beam. The same truncation analysis was also performed for the BISOU Instrument V1 Design:

	M5	M4	M3	M2	M1	Secondary	Primary
GRASP	0.9926	0.9915	0.9893	0.9886	0.9690	0.9622	0.9162
Laguerre modes	0.9932	0.9925	0.9812	0.9800	0.9660	0.9613	0.9537

Table 6.3 Circularly symmetric truncation analysis values for the BISOU Instrument V1. Spillover values from GRASP are compared with truncation values from the Laguerre-Gaussian truncation analysis python code.

6.9.1 Hermite-Gaussian Truncation Analysis

The final design for BISOU will utilise pyramidal horns which have cartesian symmetry. To more accurately represent the cartesian symmetry present in beam modes supported by these horns, Hermite-Gaussian Beam modes can be used to represent the beam. As the beam modes supported by a pyramidal horn have rectangular symmetry it may be better to simulate the system with square mirrors to better match the symmetry present in the pyramidal horn beam modes. Both mirror geometries were tested to determine how significant the difference would be.

This simulation was performed with the Hermite-Gaussian truncation code described in section 5.2.

Table 6.4 below shows results for the BISOU Breadboard Design truncation analysis with Hermite-Gaussian Beams for square mirrors:

Mirror	M5	M4	M3	M2	M1	Secondary	Primary
Hermite modes	0.9941	0.9941	0.9882	0.9882	0.9823	0.9821	0.9819
GRASP	0.9956	0.9943	0.9926	0.9918	0.9900	0.9863	0.9820

Table 6.4 Truncation values for python Hermite-Gaussian truncation code and values from GRASP for a Gaussian beam simulation with square mirrors.

Table 6.5 shows results for the BISOU Instrument V1 with Hermite-Gaussian Beams and square mirrors.

Mirror	M5	M4	M3	M2	M1	Secondary	Primary
Hermite modes	0.9941	0.9941	0.9882	0.9881	0.9823	0.9821	0.9782
GRASP	0.9960	0.9955	0.9939	0.9936	0.9901	0.9863	0.9345

Table 6.5 Truncation values for python Hermite-Gaussian truncation code and values from GRASP for a Gaussian beam simulation with square mirrors.

6.9.2 Multimode Horn Analysis

The first test of the systems using the beam modes generated as described in section 5.3 was conical horn modes with elliptical mirrors. Conical horn beams and elliptical mirrors both have circular symmetry and are useful as a starting point for simulating optical or quasioptical systems. The horn modes were propagated incoherently through both systems and then summed up at the output. This process was performed for both of the recent BISOU designs discussed previously the breadboard design and the BISOU Instrument V1 design.

BISOU Breadboard Conical Horn with circular rim mirrors

Figure 6.15 below shows the normalised beam on the sky above after propagation through the BISOU Breadboard system. It looks symmetric and is similar in profile to the Gaussian beam analysis illustrated in figure 6.10b.

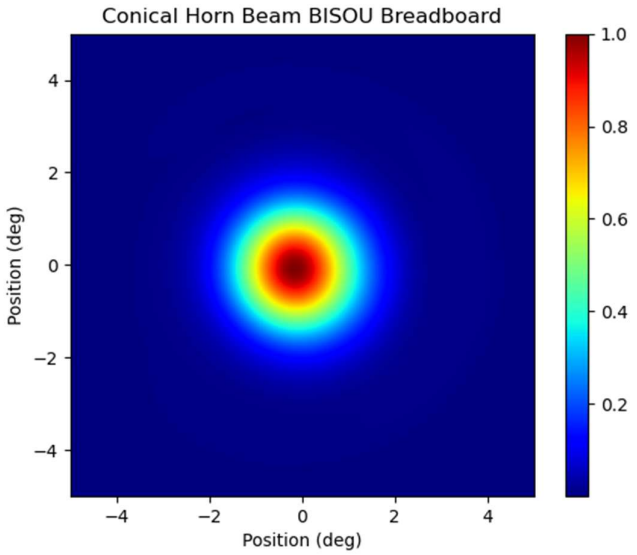

Figure 6.15 Normalised beam after propagation through the BISOU breadboard system.

The beam in figure 6.20 is circularly symmetric and shows a gaussian-like intensity profile. This would be expected for the given input beam propagating through a system with limited truncation/distortion. A plot of perpendicular cuts through the above beam demonstrates the level of symmetry:

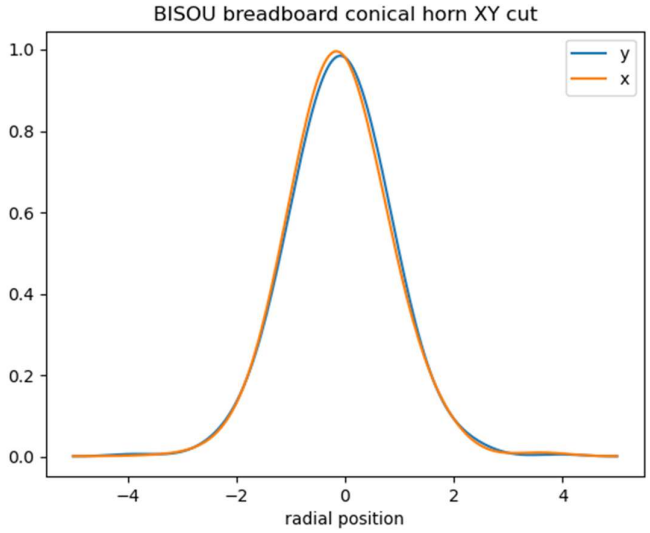

Figure 6.16 Above is plotted two slices through the beam shown in figure 6.20. If the assumption made above that this beam is symmetrical then it would be expected that two perpendicular slices would overlap, showing circular symmetry. While this is not exact, the plot shows very good agreement between the two beam cuts and thus a good level of symmetry of the beam.

BISOU Instrument V1 Conical Horn circular mirrors

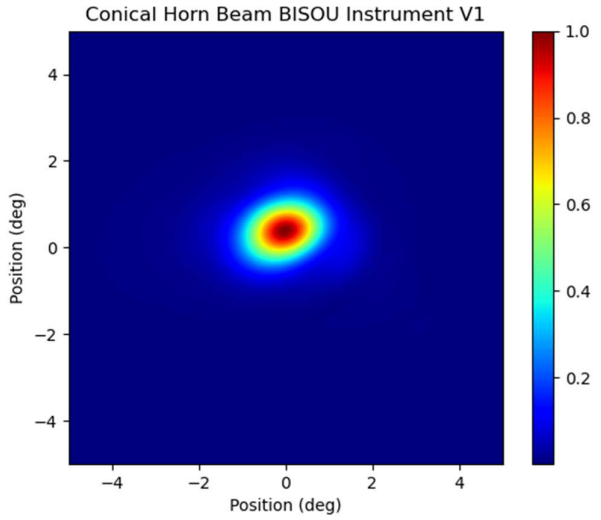

Figure 6.17 Normalised conical horn beam after propagation through V1 of the BISOU instrument design. It is clear that the beam is much less symmetrical than the beam propagated through the breadboard design. This is likely caused by the fact that the beam is thrown out of the plane for the Instrument design to accommodate the layout of the cooling system/gondola.

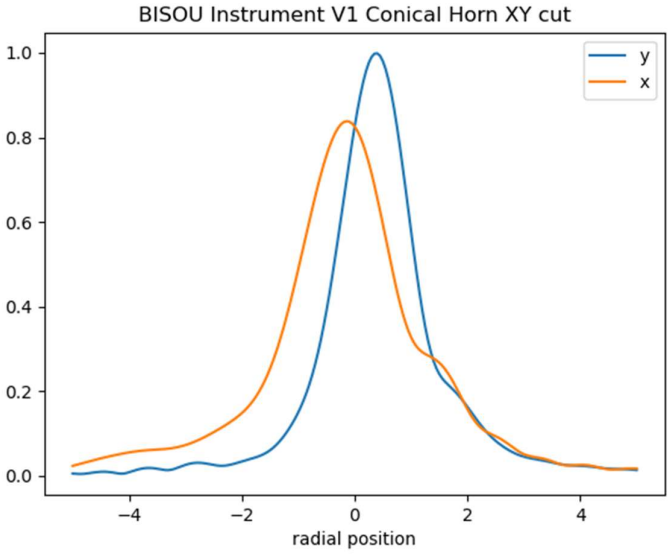

Figure 6.18 XY cut of normalised conical horn beam after propagating through the BISOU V1 instrument design. The level of symmetry is much worse than for the breadboard design and more aberration and distortion of the beam is apparent. This is likely due to the reorientation of the telescope to be out of the FTS plane in the instrument design as opposed to the breadboard design where everything remains in plane.

Pyramidal Horns circular rimmed Mirrors

The next test of the two systems was to run pyramidal horn modes through the systems. These modes are propagated through the system in GRASP from a series of grid files described previously in section 5.3. The pyramidal horn beam modes were initially tested with circular mirrors as round mirrors were the default reflector geometry chosen throughout this project. As the symmetry present in a pyramidal horn is Cartesian this choice of mirror may lead to worse distortion of the beams, however both geometries will be tested to determine how significant this difference is.

BISOU Breadboard

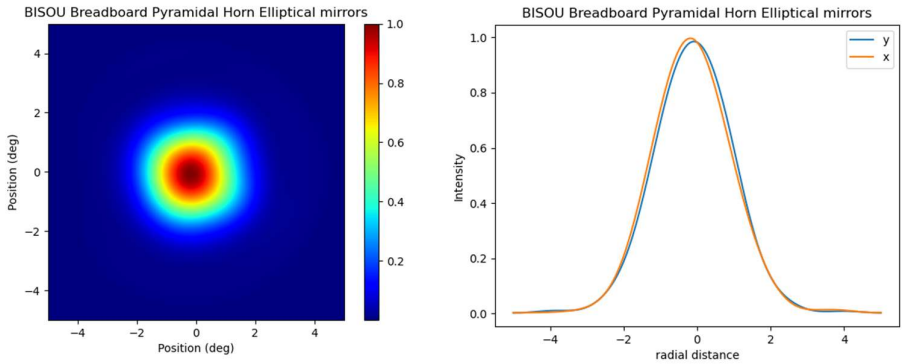

Figure 6.19 Beam plot and beam XY cut for a pyramidal horn beam propagated through the BISOU breadboard system, with elliptical mirrors. The beam profile is very similar to the plot in figure 6.20. This indicates that using elliptical mirrors may not be too much of an issue with the pyramidal horn beam as it appears to have little beam aberration/truncation effects

BISOU Instrument V1

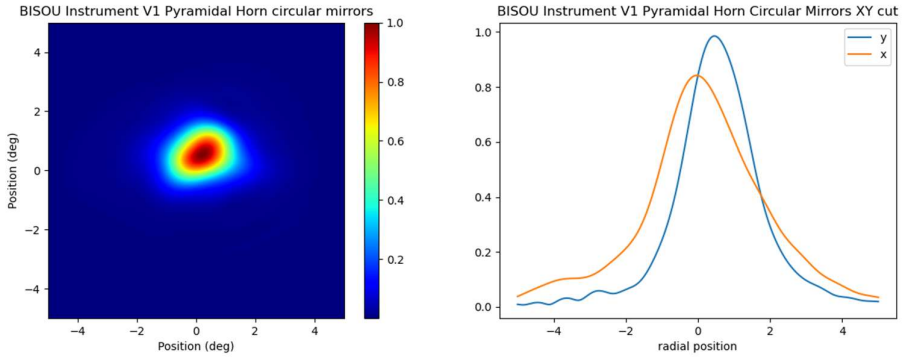

Figure 6.20 Beam plot and beam XY cut for a pyramidal horn beam propagated through the BISOU instrument, with elliptical mirrors. The beam profile is very similar to the plot in figure 6.20. This indicates that using elliptical mirrors may not be too much of an issue with the pyramidal horn beam as it appears to have little beam aberration/truncation effects

Pyramidal Horns Square Mirrors

The pyramidal horn beams were also tested with square mirrors as these square mirrors would better match the symmetry present in the pyramidal horn beams.

BISOU Breadboard

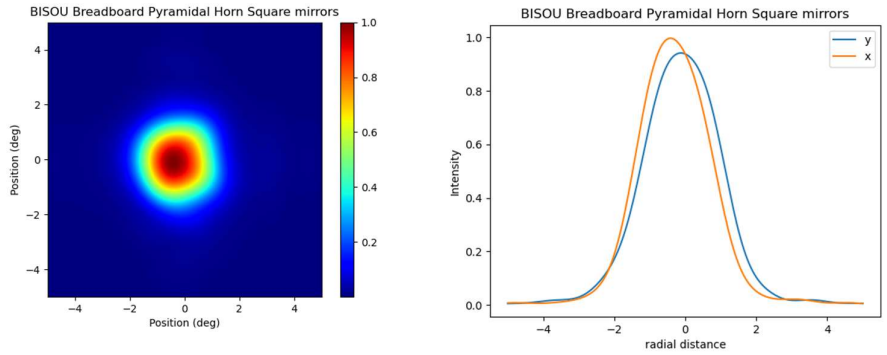

Figure 6.21 Beam plot and XY cut of a pyramidal horn beam propagated through the BISOU breadboard system with square mirrors.

It can be seen from figure 6.26 that the beam still retains a very good level of symmetry as was the case in figure 6.21 and 6.20. This shows that the modification of the mirrors to be square and the use of the pyramidal horn beam instead of the conical horn did not negatively affect the beam quality. This indicates that as suspected, the square mirrors were in fact a better match for the Cartesian symmetry of the pyramidal horn beam. A full truncation study will need to be performed using the beam modes described here but initial results indicate the benefits of matching the mirror geometry to the horn geometry.

BISOU Instrument V1

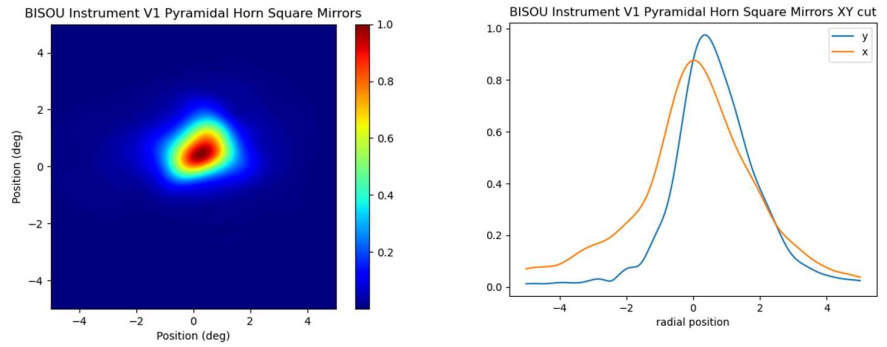

Figure 6.22 Beam plot and XY cut of a pyramidal horn beam propagated through the BISOU V1 Instrument system with square mirrors

Full simulation with polarising grids

A full simulation of the BISOU optics requires the inclusion of polarising grids. The output beam will have a lower power/intensity than the beam without the inclusion of polarising grids, as a portion of the beam will be reflected at the polarising grid and a portion will be transmitted.

Figure 6.28 shows the BISOU breadboard design in GRASP now with the addition of polarising grids. These polarising grids are oriented as shown in the diagram in figure 2.1. In the future a full polarisation characterisation of BISOU is required to analyse all polarisation components it all paths. This preliminary analysis here just allows all polarisations initially leave the horn antenna but then due to the inclusion of the polarizing grids half the modes will be lost (one orthogonal mode set) leaving half the modes propagate along the path analysed. Therefore, the beams below indicate a linear polarisation limited horn mode set on the sky. The beams will therefore lack the symmetry observed above and have different profiles in the two directions plotted on the sky.

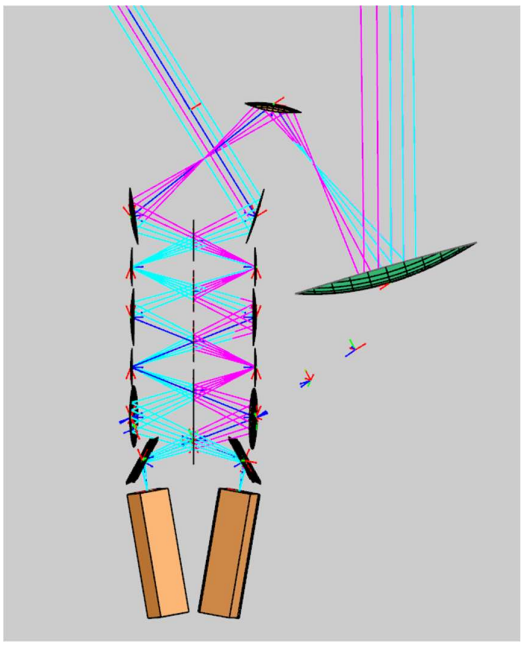

Figure 6.23 BISOU Breadboard design with polarising grids. These grids are oriented as described in figure 2.1.

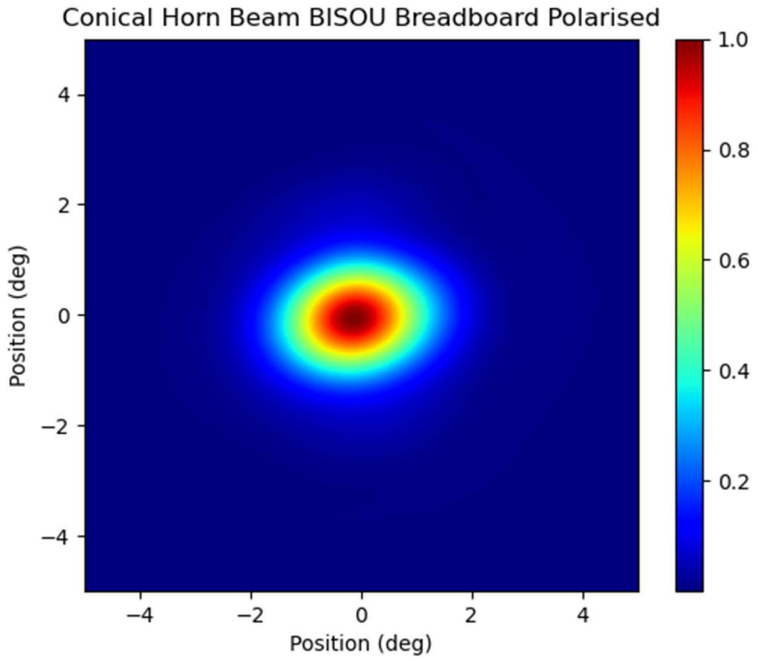

Figure 6.24 Plot of summed conical horn modes after propagation through the system in figure 6.28. This is the same design as the breadboard version described previously with the addition of polarising grids. The beam is observed to be less symmetric than before the inclusion of polarising grids.

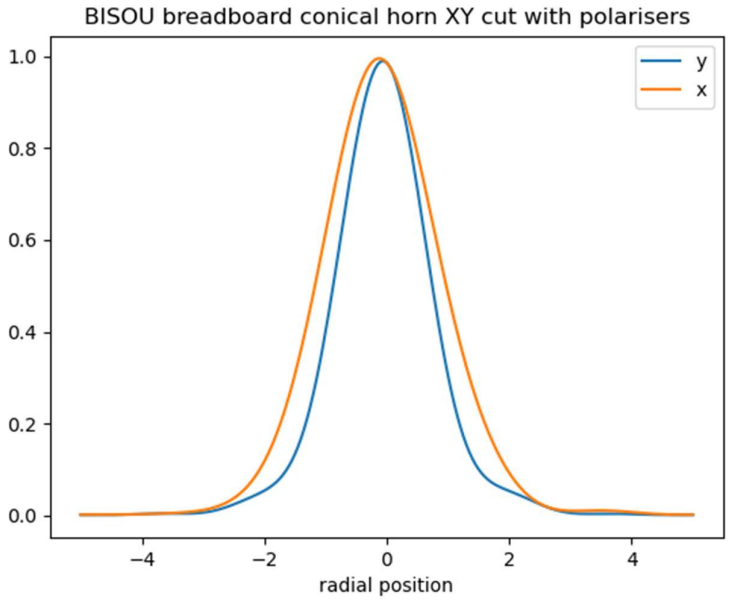

Figure 6.25 XY cut of the above beam in figure 6.29. This beam is observed to be less symmetric than before the inclusion of polarising grids

Conclusions

This thesis presents the design and analysis of a nulling polarising interferometer for measurement of CMB spectral distortions called BISOU. This work reflects the initial stages of optical design where the basic design is being realised, and various configurations of options are investigated. Many design iterations presented are optically viable but for other engineering reasons are not possible. The author spent considerable time investigating different solutions and ultimately iterating towards a working design where a realistic solution is presented.

As well as the basic optical layout, a truncation analysis was carried out to ensure the size of all optical components was large enough to accommodate various Gaussian beam sizes representing different horn antenna designs. Beam parameters along the optical train were modelled using Gaussian Beam Mode Analysis (GBMA) truncation and compared to spillover defined in the commercial software GRASP using a physical optics technique.

Theoretical predictions for the beam truncation using Laguerre-Gaussian and Hermite-Gaussian truncation analysis were compared with simulations from GRASP where a mirror's rim is defined in various ways. GRASP can simulate an off-axis truncation whereas GBMA simulations presented here assume an on-axis illumination. Also presented was a simulation of various beam modes using mode matching analysis to simulate waveguide modes propagated through conical horn and pyramidal horn antennas.

Chapter 1 introduces the concept of CMB spectral distortions and gave a scientific background and justification for the development of an instrument for the measurement of these distortions and the scientific goals.

Chapter 2 introduces the concept of a nulling polarising interferometer and justifies its use for the case of detecting spectral distortions. Also outlined are previous similar mission concepts including PIXIE (the Primordial Inflation Explorer) and FIRAS (the Far Infrared Absolute Spectrophotometer instrument on NASAs COBE mission)

Chapter 3 contains a discussion of the Physical optics simulation technique and how these simulations are implemented in GRASP. Also discussed are the limitations of both PO and GBMA.

Chapter 4 discusses the background theory behind Gaussian beams, Laguerre Gaussian modes and Hermite-Gaussian modes with an introduction to the ABCD matrix method. Examples given indicate excellent agreement between the beam parameters simulated using GBMA and a beam propagated through GRASP.

Chapter 5 describes the truncation analysis methods used in this project, mainly using Laguerre-Gaussian beam modes and Hermite-Gaussian beam modes. Analysis is performed on example optical systems and results are found to be in very close agreement to values obtained from GRASP. Also introduced is modal analysis of beams from conical and pyramidal horns.

Chapter 6 discusses a number of design iterations for the BISOU breadboard and BISOU instrument designs. Constraints on these designs are discussed, and two suitable designs are chosen at the end for further simulation using the previously described methods.

The basic optical design of BISOU is now in place and an initial analysis of a multimoded horn antenna seems feasible based on the current design. A full modal field was propagated through the optics from the horn aperture to the sky and beams look realistic. Of course, much more detailed analysis is required to fully verify the optical performance of BISOU across multiple frequencies and with optimised horn designs

Future Work

Future work on this project would be a wide range of tasks to check and verify many different characteristics of the BISOU optics. This thesis outlines the basic optical design and illustrates various iterations towards a working breadboard and flight instrument design. A basic initial multimoded horn antenna analysis was presented for a basic design of a conical and a pyramidal horn design. A full truncation analysis of the individual horn modes at each optical component will be required to be completed and at multiple frequencies. Only the lowest frequency of 90 GHz was outlined here which has the lowest number of waveguide modes propagating and more frequencies will also be required for more detailed characterisation. Also including the full polarisation analysis of all possible paths for all reflected and transmitted polarisation components will be required when all grids are integrated into the electromagnetic GRASP model for all waveguide modes. At that stage then a decision of the mirror shapes (either square or circular) can be made based on detailed analysis. It would seem that square mirror surfaces would maximise throughput and may be required for higher order modes. Also, the moving mirror of the FTS also needs to be analysed carefully, and the nominal range of movement needs to be analysed in detail in GRASP and effects on beam shape and profile checked as the mirror moves over its prescribed range of distances.

Further investigation of any beam aberrations present will be required. It is important to determine if this beam aberration can be eliminated through further modification of the optical design. If this aberration cannot be eliminated, constraints should be established on how much this will negatively interfere with the interferometry.

Of course, the optical design of the mirrors and polarizing grids need to be closely matched with the horn design and modal profile and incorporating the detector array in the optical analysis is also a final stage of optical analysis. Different horn designs might require different sized optical components in the BISOU train.

The calibrator so far in the analysis is only modelled as a perfect blackbody located at a specific location in the optical design. Using GRASP, the beam will need to be coupled to the blackbody source efficiently and so more detailed optical analysis is also required here.

Bibliography

Alpher, R. A. & Herman, R. C., 1949. Remarks on the Evolution of the Expanding Universe. *Physical Review,* 75(7).

Anon., n.d. *Thorlabs:Gaussian Distribution*. [Online]
Available at:
https://www.thorlabs.com/NewGroupPage9_PF.cfm?Guide=10&Category_ID=141&ObjectGroup_ID=16

Baumann, D. et al., 2008. Probing inflation with CMB Polarisation.

Boggess, N. et al., 1992. The COBE Mission: Its Design and Performance Two Years after Launch. *The Astrophysical Journal,* Volume 397.

Bothun, G., 1998. *Modern Cosmological Observations and Problems*. s.l.:CRC Press.

Burke, D., 2021. Design and Analysis pf the Optical Beam Combiner and Corrugated Feed Horns for the QUBIC Instrument.

Cervantes-Cota, J. L., Galindo-Uribarri, S. & Smoot, G. F., 2023. The Unsettled Number: Hubble's Tension. *Universe*.

Chen, B. et al., 2025. A Review of Sub-Wavelength Wire Grid Polarizers and Their Development Trends. *MDPI Photonics,* 12(11).

Chluba, J., 2016. Which spectral distortions does ΛCDM actually predict?. *Monthly Notices of the Royal Astronomical Society,* 460(1), pp. 227-239.

Chluba, J. et al., 2019. New Horizons in cosmology with spectral distotions of the Cosmic Microwave Background. *ESA Voyage 2050 Science White Paper*.

Chluba, J. et al., 2020. Spectral Distortions of the CMB as a Probe of Inflation,.

Colgan, R., 2001. Electromagnetic and quasi-optical modelling of horn antennas for far-IR space applications..

Coulon, X., Maffei, B. & Aghanim, N., 2024. Towards measurements of the CMB spectral distortions. *EPJ Web of Conferences,* Volume 293.

Doherty, S., 2012. Optical and Quasi-Optical Design and Analysis of Astronomical Instrumentation including a Prototype SAFARI Pixel.

Ellingson, S. W., 2020. Rectangular Waveguide-TE Modes. In: *Electromagnetics, Volume 2*. s.l.:Virginia Tech University.

Finn, T., 2007. Quasioptical Verification of HIFI for the Herschel Space Observatory and Standing Waves in Quasioptical Systems.

Fixsen, D. et al., 1996. The Cosmic Microwave Background Spectrum from the Full COBE FIRAS Data Set. *The Astrophysical Journal*.

Gleeson, E., 2004. Single and multi-moded corrugated horn design for cosmic microwave background experiments.

Goldsmith, P. F., 1998. Fundamental Gaussian Beam Mode in Rectangular Coordinates: One Dimension. In: *Quasioptical Systems: Gaussian Beam Quasioptical Propagation and Applications*. s.l.:Wiley-IEEE Press, pp. 16-18.

Goldsmith, P. F., 1998. Higher Order Modes in Rectangular Coordinates. In: *Quasioptical Systems: Gaussian Beam Quasioptical Propagation and Applications*. s.l.:Wiley-IEEE Press, pp. 30-32.

Heki, L. K., 2024. Design and Optimisation of Phased-Array Metasurfaces for Applications in Light Emission and Quantum Optics.

Herold, L. & Ferreira, E. G., 2022. Resolving the Hubble tension with Early Dark Energy.

Ji, X. & Dou, L., 2012. Two types of definitions for Rayleigh range. *Optics and Laser Technology,* 44(1), pp. 21-25.

Kehoe, S., 2008. *An Investigation of Efficient Submillimetre Analytical Techniques and methods of modelling multiple reflections*. s.l.:s.n.

Kobayashi, H., 2020. Physical Optics.

Kogut, A. et al., 2020. Astro2020 APC White Paper CMB Spectral Distortions: Status and Prospects.

Kogut, A. et al., 2025. The Primordial Inflation Explorer (PIXIE): Mission design and science goals. *Journal of Cosmology and Astroparticle Physics*.

Kogut, A. et al., 2011. The Primordial Inflation Explorer (PIXIE): A Nulling Polarimeter for Cosmic Microwave Background Observations. *Journal of Cosmology and Astroparticle Physics*.

Kouveliotou, C. et al., 2014. Enduring Quests-Daring Visions (NASA Astrophysics in the Next Three Decades).

Leclercq, S., 2007. Discussion about Noise Equivalent Power and its use for photon noise calculation. *Institut de Radioastronomie Millimetrique*.

Li, J., Lu, D.-f. & Qi, Z.-m., 2015. A Modified Equation for the Spectral Resolution of Fourier Transform Spectrometers. *Journal of Lightwave Technology,* 33(1).

Lucca, M., 2020. The role of CMB spectral distortions in the Hubble tension: a proof of principle.

Lucca, M., 2023. *The future of cosmology? A case for CMB spectral distortions*. Brussels: Université libre de Bruxelles.

Maffei, B. et al., 2021. BISOU: a balloon project to measure the CMB spectral distortions. *Proceedings of the 16th Marcel Grossmann Meeting on Recent Developments in Theoretical and Experimental General Relativity, Astrophysics and Relativistic Field Theories*.

Maffei, B. et al., 2021. BISOU: A balloon project to measure the CMB spectral distortions. *The Sixteenth Marcel Grossman Meeting*.

Maffei, B. et al., 2024. BISOU: a balloon pathfinder for CMB spectral distortions studies. *SPIE*.

Martin, D. H. & Bowen, J. W., 1993. Long-Wave Optics. *IEEE TRANSACTIONS ON MICROWAVE THEORY AND TECHNIQUES,* 41(10).

Masterman, P. & Clarricoats, P., 1971. Computer field matching solution of waveguide transverse discontinuities. *IEEE,* Volume 118, pp. 51-63.

Mather, J. C., Fixsen, D. J. & Shafer, R. A., 1993. Design for the COBE far-infrared absolute spectrophotometer (FIRAS). *SPIE,* Volume 2019.

Mather, J., Cheng, E., Cottingham, D. & Eplee, R., 1994. Measurement of the Cosmic Microwave Background Spectrum by the COBE FIRAS Instrument. *The Astrophysical Journal,* Volume 420.

Milligan, T., 1985. In: *Modern Antenna Design*. s.l.:Wiley, pp. 59-65.

Murphy, J., McCabe, M. & Withington, S., 1988. Gaussian beam mode analysis of the coupling of power between horn antennas. *International Journal of Infrared and Millimeter Waves,* Volume 18.

NASA Goddard Space Flight Centre Astrophysics Science Division, 2021. *Galactic Emission*. [Online]
Available at:
https://asd.gsfc.nasa.gov/archive/arcade/science_galaxy.html
[Accessed 1 October 2025].

Olver, A., Clarricoats, P., Kishk, A. & Shafai, L., 1994. *Microwave Horns and Feeds*. New York: IEEE Press.

Paknys, R., 2016. Physical Theory of Diffraction. In: *Applied Frequency-Domain Electromagnetics*. s.l.:Wiley IEEE, pp. 317-334.

Rahimi, M. & Reichardt, C. L., 2024. Polarization of the Cosmic Microwave Background. *Encyclopedia of Astrophysics*.

Räsänen, S., 2009. On the relation between the isotropy of the CMB and the geometry of the universe.

Sarkar, A., Sethi, S. K. & Das, S., 2017. The effects of the small-scale behaviour of dark matter spectrum on CMB spectral distortion. *Journal of Cosmology and Astroparticle Physics*.

Siegman, A. E., 1990. *Lasers*. s.l.:University Science Books.

Smoot, G. F., 1997. THE CMB SPECTRUM.

Tashiro, H., 2014. CMB spectral distortions and energy release in the early universe. *Progress of Theoretical and Experimental Physics,* 2014(6).

Weisstein, E. W., 1999. *Laguerre Differential Equation*. [Online] Available at: https://archive.lib.msu.edu/crcmath/math/math/l/l039.htm [Accessed 12 November 2025].

Wexler, A., 1967. Solution of Waveguide Discontinuities by Modal Analysis. *IEEE Transactions on Microwave Theory and Techniques,* pp. 508-517.